OECD/MCCI-2010-TR02

OECD MCCI Project
Category 2 Coolability Engineering Enhancement Tests:
Final Report

Rev. 1 - Final

November 2010

by:

M. T. Farmer, S. Lomperski, R. W. Aeschlimann, and D. J. Kilsdonk

Nuclear Engineering Division
Argonne National Laboratory
9700 S. Cass Avenue
Argonne, IL 60439 USA

Table of Contents

Table of Contents (Contd.)

List of Figures

Figure **Page**

List of Figures (Contd.)

Figure **Page**

List of Figures (Contd.)

Figure **Page**

List of Tables

1.0 INTRODUCTION

1.1 Background

Ex-vessel debris coolability is an important light water reactor (LWR) safety issue. For existing plants, resolution of this issue will confirm the technical basis for severe accident management guidelines (SAMGs). For new reactors, understanding this issue will help confirm the effectiveness of the design and implementation of new accident mitigation features and severe accident management design alternatives (SAMDAs). The first OECD-MCCI program [1-4] conducted reactor material experiments focused on achieving the following technical objectives: i) provide confirmatory evidence and data for various cooling mechanisms through separate effect tests for severe accident model development, and ii) provide long-term 2-D core-concrete interaction data for code assessment and improvement.

Debris cooling mechanisms investigated as part of the first program included: i) water ingression through cracks/fissures in the core debris, ii) melt eruption caused by gas sparging, and iii) large-scale crust mechanical failure leading to renewed bulk cooling. The results of this testing and associated analysis [1,5-6] provided an envelope (principally determined by melt depth) for debris coolability. However, this envelope does not encompass the full range of potential melt depths for all plant accident sequences. Cooling augmentation by additional means may be needed at the late stage to assure coolability for new reactor designs as well as for various accident sequences for existing reactors. In addition, the results of the CCI tests showed that lateral/axial power split is a function of concrete type. However, the first program produced limited data sets for code assessment. In light of significant differences in ablation behavior for different concrete types, it became clear that additional data would be useful in reducing uncertainties and gaining confidence in code predictions.

Based on these findings, a broad workscope was defined for the follow-on MCCI-2 program. The workscope was divided into the following four categories:

1) Combined effect tests to investigate the interplay of different cooling mechanisms, and to provide data for model development and code assessment purposes.
2) Tests to investigate new design features to enhance coolability, applicable particularly to new reactor designs.
3) Tests to generate two-dimensional core-concrete interaction data.
4) Integral tests to validate severe accident codes.

In addition to the experimental work, an analysis task was defined to develop and validate coolability models to form the basis for extrapolating the experiment findings to plant conditions.

As part of the steps involved in satisfying these objectives, the project Management Board (MB) approved the conduct of three dedicated experiments to provide data in the area of Category 2: design features to enhance coolability. The MB convened a subcommittee to recommend testing options to investigate generic approaches for augmenting ex-vessel corium coolability in new reactors. Based on the committee deliberations, two general approaches for stabilizing ex-vessel core melts were defined; i.e.,

1) a cold-crucible method in which decay heat from the corium is removed by cooling of the crucible exterior boundary with water, and
2) a melt fragmentation method in which water is introduced at the bottom of the melt pool at a slight overpressure, and the ensuing steam formation acts to cool and solidify the melt in a highly porous configuration that is readily permeable by water.

On the basis of deliberations that spanned several Project Review Group (PRG) meetings, the MB subsequently approved the conduct of one large scale water-cooled basemat integral effect test to provide data on the cold-crucible method for melt stabilization, and two separate effect tests that utilized the SSWICS test facility [3] to provide data on the melt fragmentation method for melt stabilization. This final report summarizes the test facilities, operating procedures, and key test results obtained from these three experiments. Additional details can be found in the test plans [7-9] and follow-on data reports [10-12] for the experiments.

1.2 Objectives and Approach

Specifications for the Water-Cooled Basemat (WCB-1) integral effect test are provided in Table 1-1. The objective was to provide prototypic data on the transient evolution and stabilization of a core melt in a generic water-cooled core catcher design for advanced plant applications. The experiment approach was to incorporate a water-cooled basemat into the core-concrete interaction test apparatus used for the CCI tests [2]. The basemat was composed of five parallel water channels that were instrumented to provide both local and global data on the heat transfer performance. The basemat was covered with a layer of sacrificial concrete that would be ablated by the overlying melt at the start of the experiment. Eventually, the melt would approach, and then be thermally stabilized at, the interface of the water-cooled basemat. Due to the longer timeframe associated with this type of test, it was necessary to Direct Electrically Heat (DEH) the melt to provide sufficient time for the melt to come to thermal equilibrium.

Specifications for the two SSWICS tests that were carried out to provide data on the melt fragmentation cooling mechanism are provided in Table 1-2. The objective of the first test (denoted SSWICS-12, which was the 12^{th} test in the SSWICS series) was to evaluate the effect of pressure head on the debris cooling rate using a porous concrete nozzle design. The approach for achieving this objective was to install four nozzles into the inert MgO basemat of the SSWICS apparatus; each nozzle was fed by a different header tank, and the four tanks were positioned at different elevations in the test cell in order to vary the water head to each nozzle. The test section was divided into four quadrants using a tungsten cruciform, with one nozzle in each quadrant. This design basically allowed four tests to be conducted simultaneously. The objective of the second test (i.e., SSWICS-13) was to examine the influence of concurrent noncondensable (i.e., N_2) gas injection on the local debris cooling rate, since the presence of non-condensable gas during melt-water interaction is postulated to suppress the possibility of an energetic interaction [13]. For this test, four stainless steel tube nozzles were incorporated into the basemat; two were fed with water only, while the other two were fed with a gas-water mixture. For this test, a tungsten cruciform was used to separate the test section into two sectors; the first side contained the water-fed nozzles, while the second contained the water-gas mixture nozzles. This approach thus allowed two tests to be conducted simultaneously.

Table 1-1. Specifications for WCB-1.

Parameter	Specification
Corium	100 % oxidized PWR with 8 wt % siliceous concrete
Test section cross-sectional area	50 cm x 50 cm
Test section sidewall construction	Inert MgO protected by UO_2 pellet layer.
Basemat construction	0-15 cm depth: siliceous concrete
	15-19.4 cm: water-cooled basemat, 5 parallel channels.
System operating pressure	Atmospheric
Melt formation technique (timescale)	Chemical reaction (~30 seconds)
Initial melt mass (depth)	400 kg (25 cm)
Initial melt temperature	1950 ºC
Melt heating technique	Direct Electrical (Joule) Heating
Initial power input level	Constant power at 80 kW[a]
Inlet water temperature	15 ºC
Inlet water flow rate	2 liters/second
Sustained water depth over melt	50 ± 5 cm

[a]Based on 150 kW/m^2 design heat flux to bottom and top surfaces of melt (0.5 m^2 area), plus an additional 5 kW to compensate for a long-term heat losses of 10 kW/m^2 to MgO sidewalls (0.5 m^2 area).

Table 1-2. Specifications for SSWICS-12 and -13.

Parameter	SSWICS-12	SSWICS-13
Corium	100 % oxidized PWR with 15 wt % siliceous concrete	100 % oxidized PWR with 15 wt % siliceous concrete
Test section cross-sectional area	30 cm ID	30 cm ID
Test Section sidewall construction	Inert MgO	Inert MgO
Basemat construction	Inert MgO	25 mm thick LCS concrete over 38 mm thick inert MgO
System operating pressure	Atmospheric	Atmospheric
Melt formation technique (timescale)	Chemical reaction (~30 seconds)	Chemical reaction (~30 seconds)
Initial melt mass (depth)	136 kg (30 cm)	136 kg (30 cm)
Initial melt temperature	2000 ºC	2000 ºC
Melt heating technique	None	None
Basemat nozzles	4 each (same radius = 108 mm)	4 each: 2 ea water; 2ea water/gas (same radius = 106 mm)
Nozzle diameter	32 mm	13.2 mm
Nozzle characteristics	Porous concrete	Single tube for water Double tube for water/gas
Concrete thickness above nozzles	0 mm	10 mm
Partition	4 regions	2 regions
Water supply pressure	0.2, 0.15, 0.1, 0.05 bar	0.2 bar
Maximum water flow rate	~ 2.4 lpm	~ 1.2 lpm
Maximum gas flow rate	N.A.	0.24 lpm (20% of water flow rate)

1.3 Related Research and Development

The primary objective of research and development efforts in the area of ex-vessel corium coolability has been to demonstrate through a combination of experiments and analysis that core melt interacting with concrete can be quenched and rendered coolable over a wide range of conditions. Unfortunately, this has been an extremely difficult objective to achieve. Results to date [1,5-6] indicate that modestly deep (i.e., < 40 cm) core melt pools interacting with LCS concrete should be coolable. However, for deeper melts, or for melts interacting with siliceous concrete, the same conclusion cannot be drawn.

For new Generation 3+ plants, the focus has been on achieving long term coolability and melt stabilization as a key design objective. Vendors have taken note of the results coming out of the debris coolability R&D programs and decided that engineering features to enhance coolability would need to be built into new plant designs. As described by Sehgal [14], two approaches have been taken: i) in-vessel melt stabilization and retention, and ii) ex-vessel coolability and melt retention. In-vessel melt retention relies on flooding of the reactor pit and submerging the vessel lower head with water. The design challenge in this case is to ensure that the thermal load to the water pool through the head does not exceed the CHF limit with sufficient margin. This approach has been adopted for the AP600 [15] and AP1000 [16] plant designs.

For ex-vessel conditions, the two approaches for stabilizing the melt were summarized in Section 1.1; i.e., i) the cold crucible technique, and ii) melt fragmentation. The cold crucible technique has been adopted for the EPR^{TM} [17] that features a spreading room adjacent to the reactor pit in which the melt is cooled by water from the bottom and top after spreading is completed. An extensive series of full scale experiments were performed in order characterize the heat removal capabilities of this cooling structure [18]. The VVER-1000 also utilizes a crucible technique, but in this design the crucible is located directly below the reactor vessel [19].

The melt fragmentation technique, denoted COMET, was pioneered by Forschungszentrum Karlsruhe (FZK). Both simulant and a limited number of reactor material tests have shown that this is a very effective means for quenching and stabilizing core melt [20-22]. However, to the best of the authors knowledge, this concept has not been deployed in any current reactor design. Another concept that has been developed by Sehgal and coworkers [23-24] are downcomers that provide a pathway to channel water from the top of the melt pool to the bottom, where the water is introduced into the debris thereby achieving the same beneficial results as those observed for COMET. This technique may be useful as a simple backfit to existing plants to improve the chances of cooling and stabilizing the core melt in the event of a severe accident.

2.0 WATER COOLED BASEMAT TEST RESULTS

The high-level experiment objective of WCB-1 was to provide reactor material test data on the transient evolution and stabilization of a core melt within a generic water-cooled core catcher design for advanced plant applications. The experiment approach was to incorporate a test section featuring a water-cooled basemat into the Core Concrete Interaction (CCI) test facility to study thermal performance under long-term conditions in which melt resistance heating was provided to simulate decay heat. Details regarding the test design and experiment results are provided below.

2.1 Facility Description

2.1.1 Test Apparatus

The WCB-1 test facility consisted of a test apparatus, a power supply for Direct Electrical Heating (DEH) of the corium, a basemat water supply system, a corium top flooding water supply system, two steam condensation (quench) tanks, a ventilation system to complete filtration and exhaust the off-gases, and a data acquisition system. A schematic illustration of the facility is provided in Figure 2-1. The apparatus consisted of three rectilinear sidewall sections and a lid. The overall structure was 3.4 m tall. The sidewall sections had a square internal cross sectional area of nominally 50 cm x 50 cm.

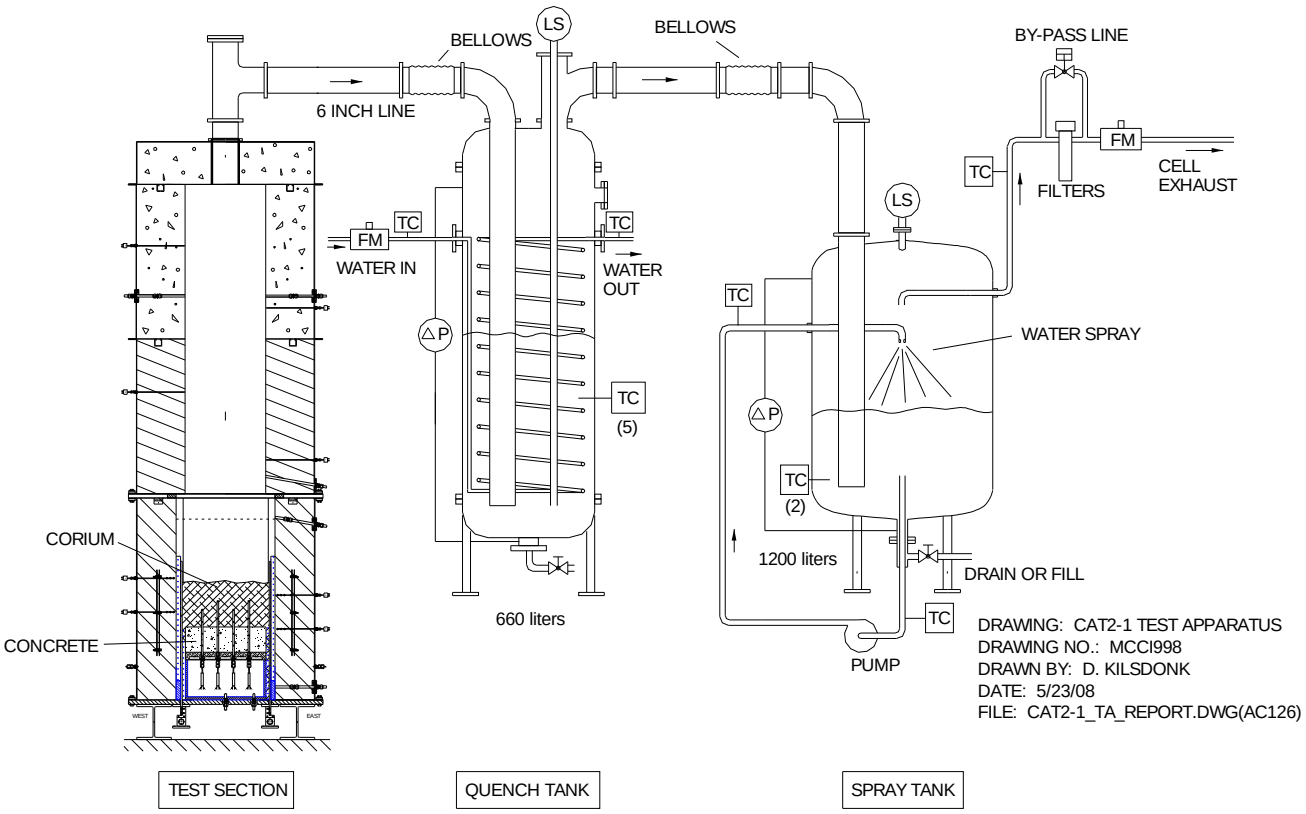

Figure 2-1. Schematic of WCB-1 Test Facility.

The test section for containment of the core melt was located at the bottom of the apparatus. Cross-sectional views showing the water-cooled basemat installation are provided in Figures 2-2 and 2-3. The design utilized four refractory MgO sidewalls that were each lined with a layer of crushed UO_2 pellets. The pellets served as an inert (i.e., non-ablative) and highly insulating wall surface. As shown in the figures, the refractory walls were equipped with tungsten backup plates to preclude sidewall melt-through if the pellet layer were to fail and sidewall erosion occurred. The plates were instrumented with contact circuits to alert operating personnel in the control room if melt contacted the plates. This detection/mitigation system formed part of the safety planning for the experiments, and on this basis it would have been difficult to modify these components to provide feed throughs for the basemat water lines and instruments. Thus, the connections were brought in through the test section bottom plate. This approach had both design and operational implications, as outlined below.

The refractory sidewalls were contained within a flanged steel form that was used to secure the lower section to the bottom test section support plate and the middle sidewall section. The flanges allowed the lower sidewalls to be disassembled to reveal the solidified corium and water-cooled basemat following the test. Aside from the instrumented basemat, multi-junction Type C thermocouple assemblies were cast within the sidewalls so that the time-dependent heat loss from the melt could be calculated from the local temperature gradient and the thermal conductivity of the MgO.

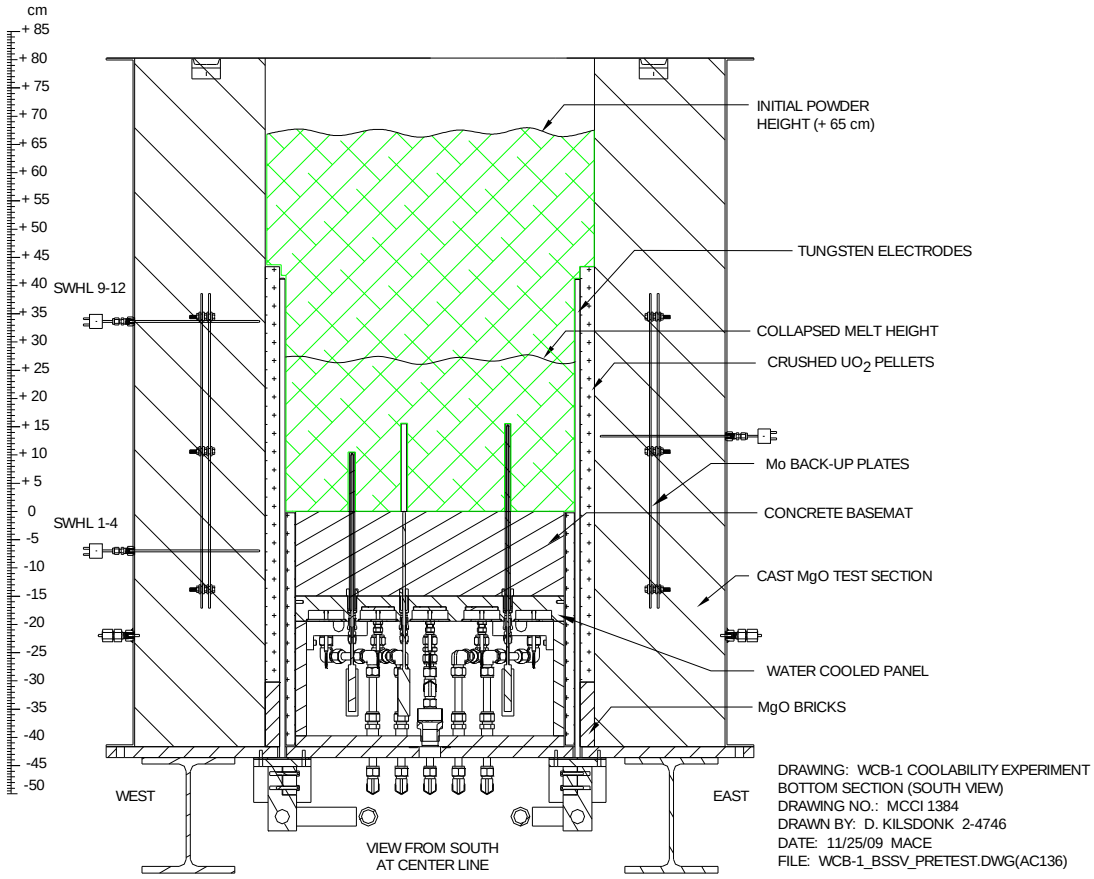

Figure 2-2. Electrode Sidewall View of Test Section.

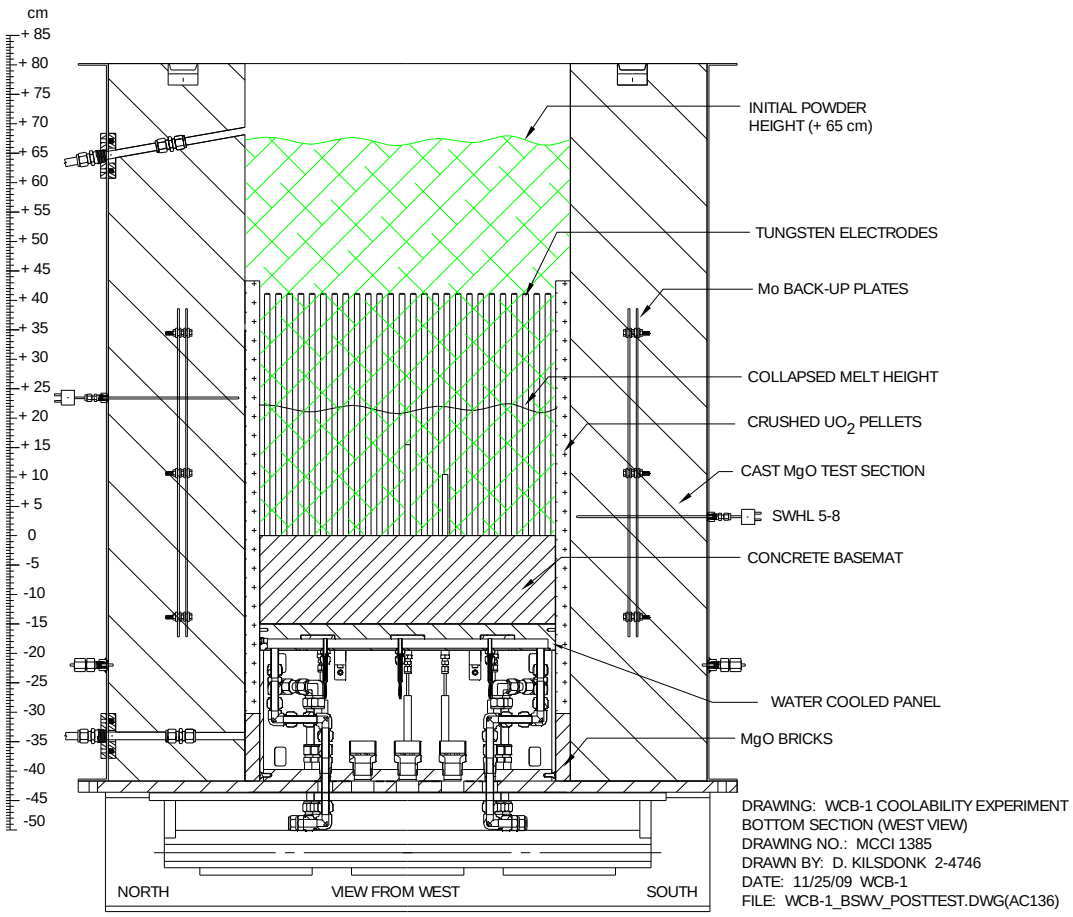

Figure 2-3. Non-Electrode Sidewall View of Test Section.

Design details of the water-cooled basemat are shown in Figures 2-4 and 2-5, while a photograph showing the actual test article after fabrication is provided in Figure 2-6. The overall layout consisted of a 15 cm deep layer of sacrificial concrete that sat on top of the water-cooled basemat plate. The plate consisted of five parallel cooling channels that were machined out of a monolithic piece of 4.4 cm thick Type 304 stainless steel. A photograph of the plate after machining is shown in Figure 2-7. Although carbon steel would be a more attractive construction material due to the higher thermal conductivity, melting point, and lower material cost, a non-magnetic material had to be used to preclude induction heating of the plate by the power supply used to resistively heat the melt. The basemat was the critical feature in this experiment, and it was essential to preclude spurious system failures that could develop as a result of fabrication techniques that could have been adopted to reduce costs. Although the monolithic design required a great deal of machining and welding, it was nonetheless adopted to minimize the chance of spurious water leaks that could form if the plate were manufactured using a cheaper method in which parts were sealed with gaskets, since these interfaces could provide leakage pathways if thermal stresses warped the plate during the test. A photograph showing the plate as it was being welded is provided in Figure 2-8.

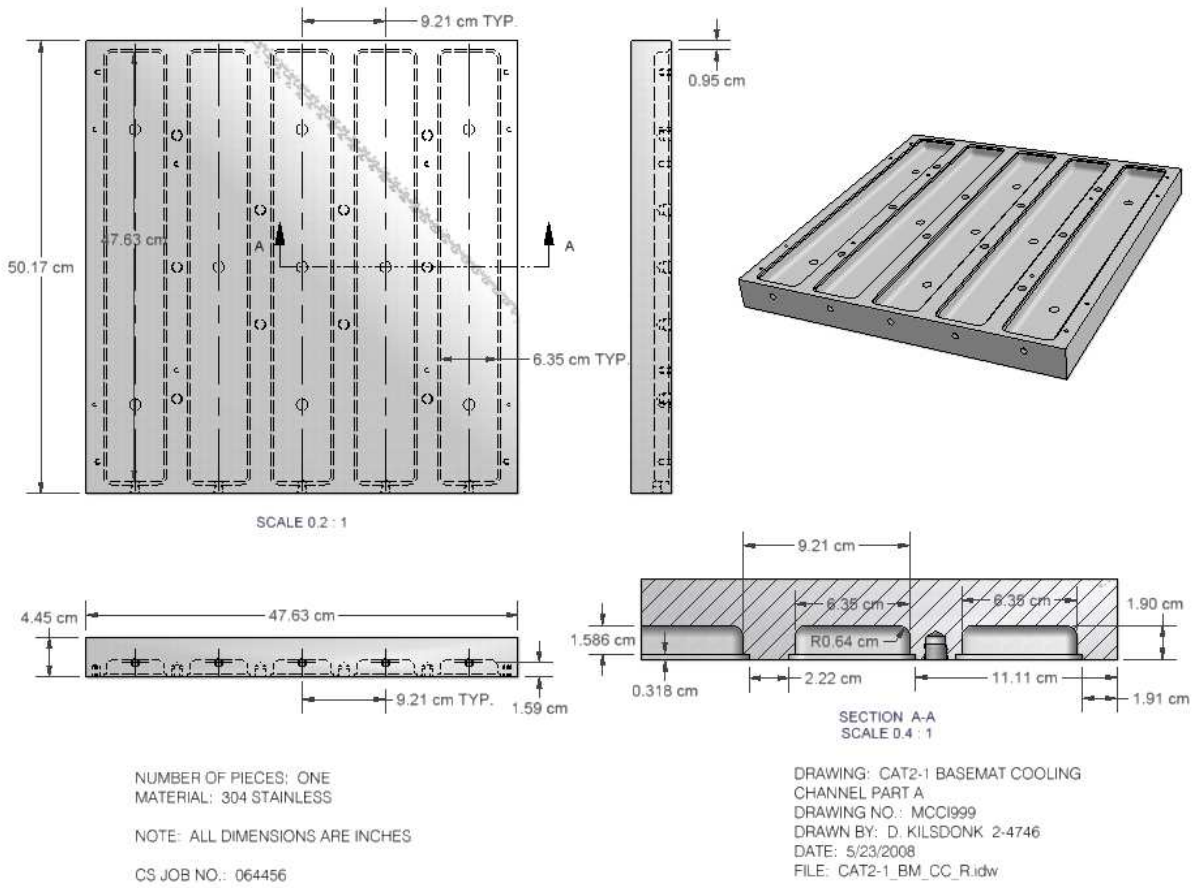

Figure 2-4. Fabrication Details of Water-Cooled Basemat.

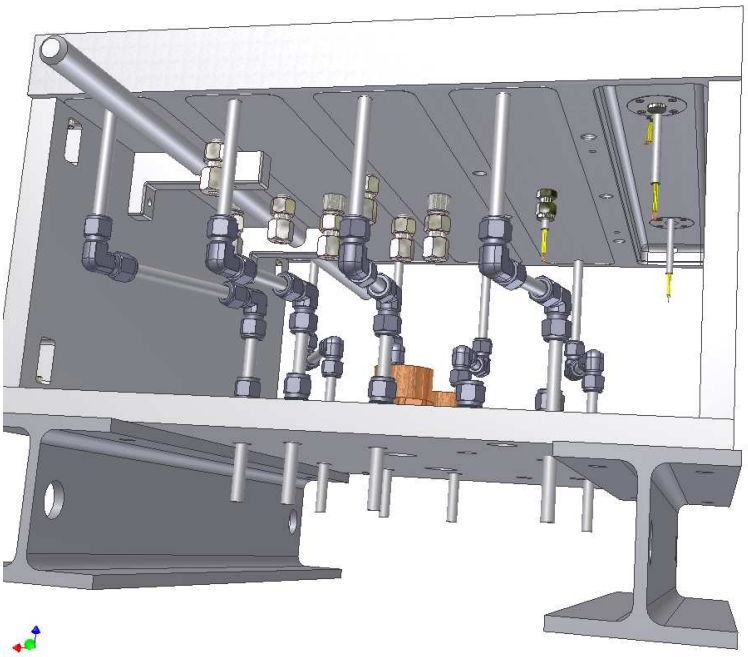

Figure 2-5. Details of Basemat Waterline and Instrumentation Feed Throughs.

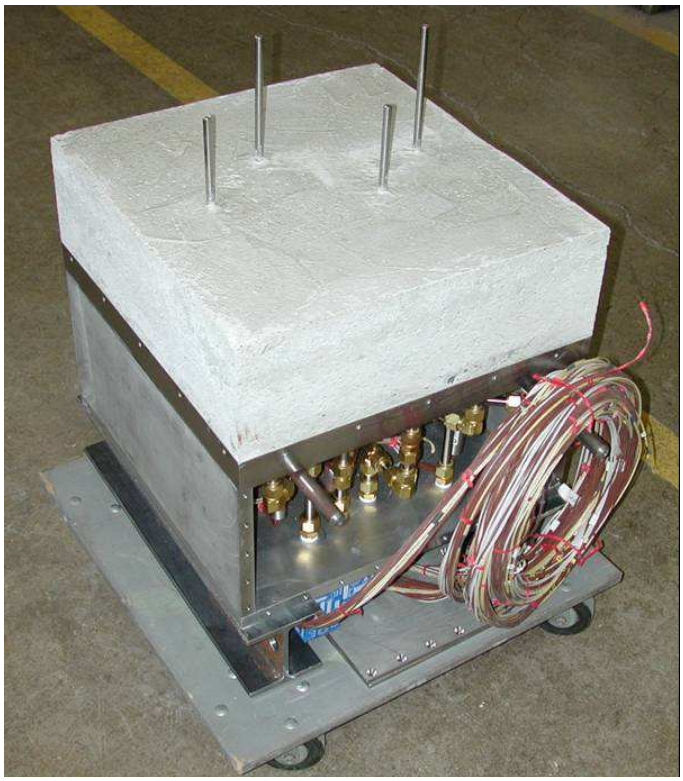

Figure 2-6. Basemat Test Article Following Fabrication.

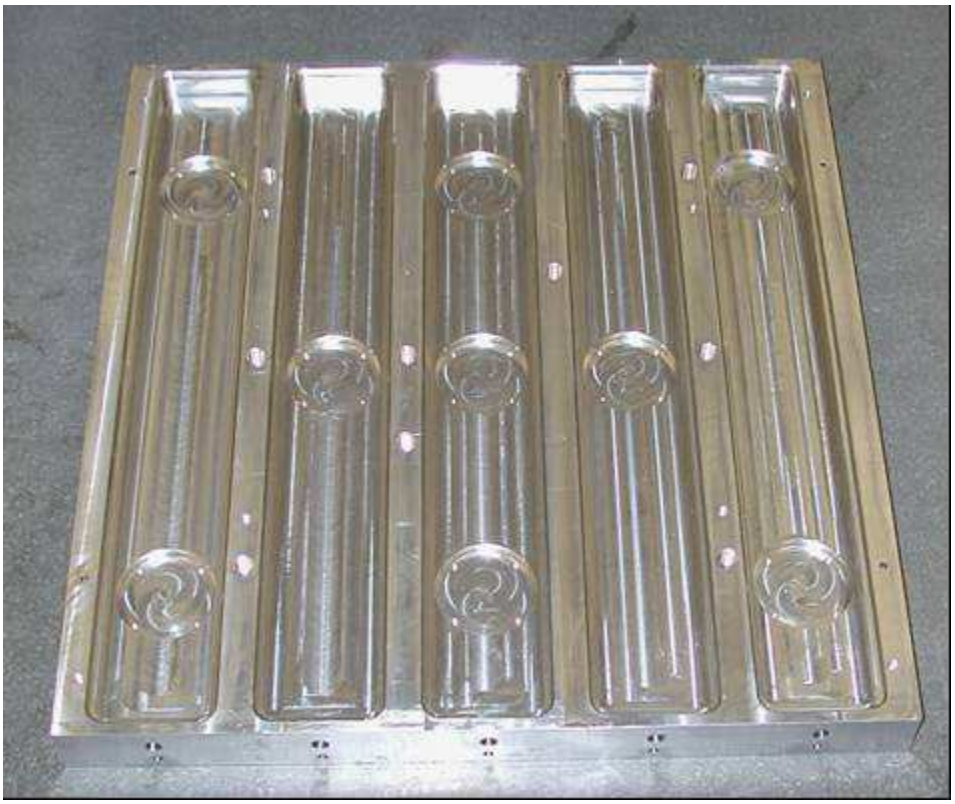

Figure 2-7. Photograph of Basemat Plate after Machining (view of bottom surface).

Figure 2-8. Photograph Showing Basemat Plate During Welding Stage.

In one of the original design concepts for this test, the basemat was segmented with non-conductive electrical material (i.e., micarda) so that a shorting path could not develop if melt were to come into direct contact with the plate in two different locations. However, there was a concern that the insulation material could cause local hot spot(s) to form that could impede plate thermal performance, and on this basis the segmentation was omitted in the final design. Thermal analysis [9] indicated that the plate should, under normal operating conditions, be protected by an insulating corium crust, and therefore the technical risk associated with omitting the segmentation was deemed to be small.

As described later in this section, the test assembly was instrumented to measure overlying melt pool temperature, ablation profile of the sacrificial concrete, and the plate/coolant thermal response. The plate instrumentation layout was also designed to minimize penetration of the water channel that could lead to the development of leaks. For the multi-junction thermocouple assemblies devoted to measuring melt temperature and basemat erosion, this was accomplished by mounting the assembly feed throughs in the unmachined regions between the individual coolant channels (see Figure 2-22 in Section 2.1.11). This somewhat limited potential locations for the assemblies, but nonetheless ensured that the feed throughs could not provide a leak path for water. Another design requirement was to electrically isolate the thermocouple assemblies from the basemat to prevent ground loops that would provide alternative current paths for the electrical current used to heat the melt. This was accomplished by using ceramic-sleeve gland seals (Conax) to mount the thermocouples to the basemat plate. In addition, the tungsten thermowells that protected the melt temperature thermocouple assemblies were electrically isolated with ceramic (fired lavite) sleeves that were used to seat the base of the wells

in the plate. Photographs showing the instrument penetrations through the plate as viewed from above and below are provided in Figure 2-9.

side from the thermocouple assemblies, the water channels were also instrumented with *in-situ* high temperature heat flux meters to provide local heat flux measurements. For these units to be effective, they had to be installed directly in the cooling channel so there was no choice but to provide feed throughs that passed directly through the channel cover plates. To ensure a leak-tight fit, specialty units were utilized that were fitted with a 6.4 mm diameter pipe nipple that passed signal wiring through the channel bottom plate; see Figures 2-10 and 2-11. In this manner, the feed throughs could be sealed using high-grade compression fittings that provided reasonable assurance that the fittings would not develop leaks during the test. As noted earlier, once the heat flux meters were installed, the channels were sealed with 3.2 mm thick 304 stainless steel cover plates that were welded in place to ensure a leak-tight fit (see Figure 2-8).

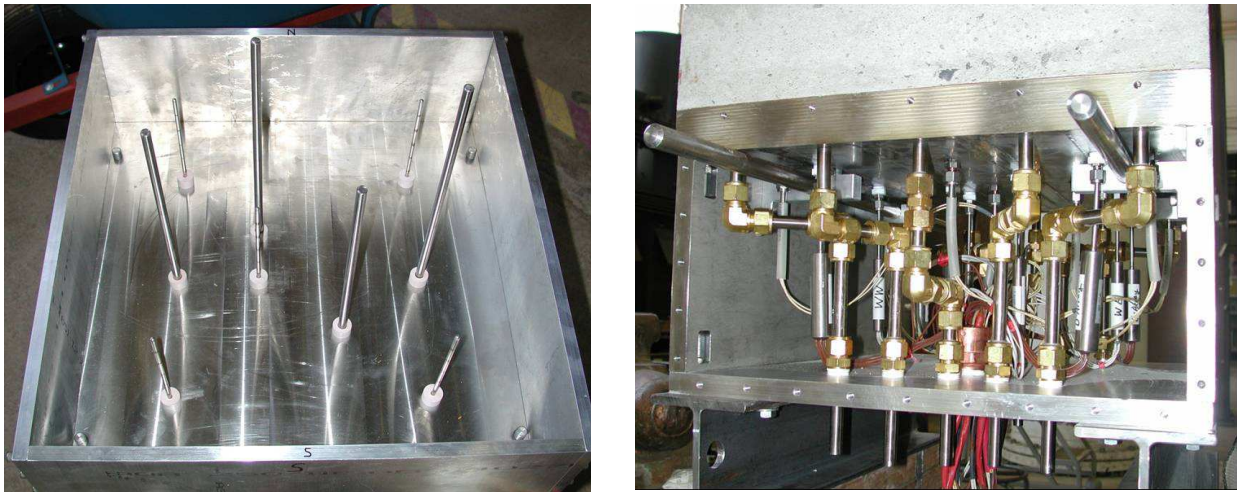

(a) **(b)**

Figure 2-9. Photograph Showing Instrument Penetrations in the Cooling Plate (a) From Above, and (b) From Below.

Melt pool generation was achieved through an exothermic "thermite" chemical reaction that produced the target initial melt mass over a timescale of ~ 30 seconds. Two iron/alumina sparklers, wrapped with nichrome starter wire, were positioned a few centimeters below the top of the corium charge near the centerline of the test section. One of these sparklers was used to initiate the thermite reaction by heating the neighboring powder to the ignition point. (The thermite composition is described later in this section). The second sparkler was provided as a backup in case the first failed to ignite the material.

A few minutes after the melt was formed, ablation of the sacrificial concrete basemat began. As shown in Figure 2-1, a large (15 cm diameter) gas line was used to vent the helium cover gas and the various gas species arising from the core-concrete interaction (i.e., CO, CO_2, H_2O, and H_2) into two adjacent tanks that were partially filled with water. In the initial phase of the experiment as the concrete was eroded, the tanks served to cool the off-gases and filter aerosols generated from the core-concrete interaction. In the late phase after the cavity was flooded, the tanks served to condense the steam and, based on the measured condensation rate,

provided data on the corium cooling rate. In both phases, the helium covergas and non-condensables (CO, CO_2, and H_2) passed through the tanks and were vented through an off gas system that included a demister and filters. The gases were eventually exhausted through the containment ventilation system and a series of high efficiency (HEPA) filters before finally being released from the building stack.

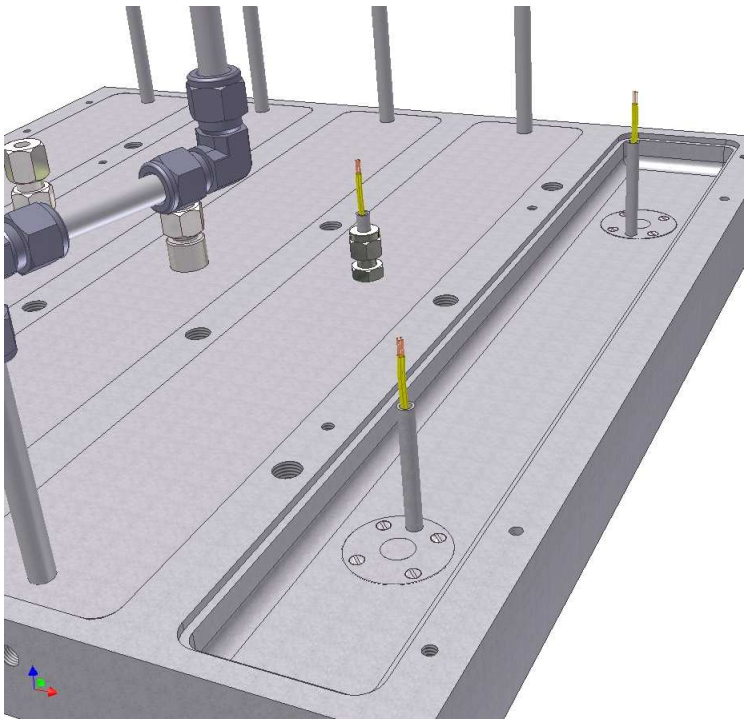

Figure 2-10. Design Details of Basemat Heat Flux Meter Installation.

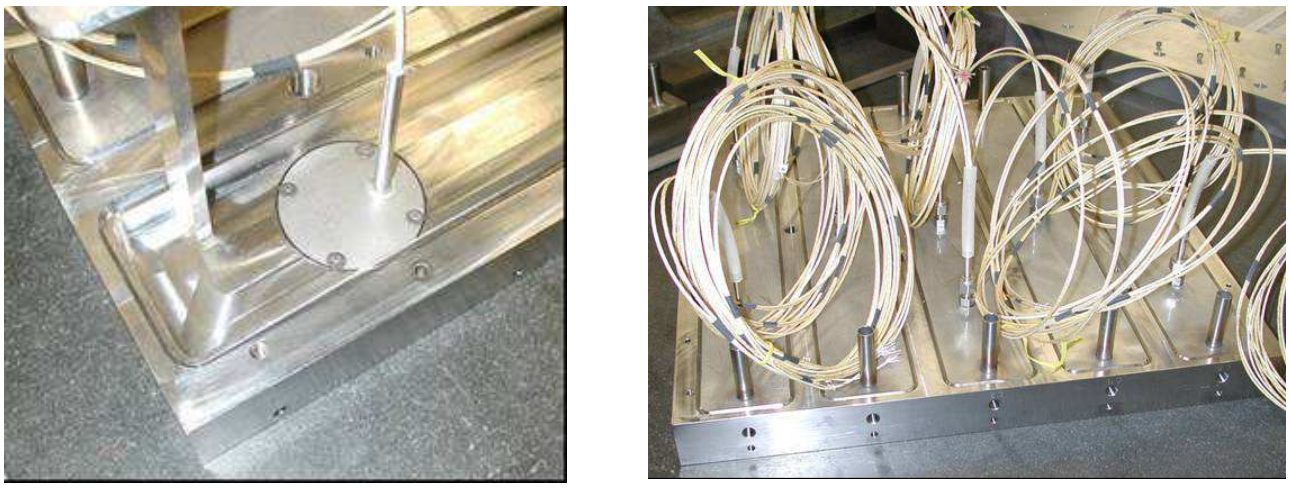

(a) **(b)**

Figure 2-11. Photographs of (a) Actual Heat Flux Meter After Installation in Channel and (b) Array of Heat Flux Meters Installed with Channel Cover Plates in Position for Welding.

After a specified period of dry core-concrete interaction, water was introduced into the test section through weirs located in the upper sidewall section just beneath the lid of the apparatus. The layout for the weirs is shown in Figure 2-12. A total of nine penetrations were

cast into the upper lid of the test section. Of these penetrations, six were utilized for WCB-1: one lid video camera view port, a port for an insertable water level probe, a 15 cm steam line to the quench system, two light ports, and a port for an optical pyrometer to view the melt upper surface.

The test section components were bolted together on the stationary half of the existing ZPR-9 reactor bed. Zirconia felt and silicon gasket material were used to seal the flanges. An illustration is provided in Figure 2-13. Installation and torquing of test section flange bolts was performed according to an approved procedure to ensure uniform preload on the flange surfaces. Additional reinforcement of each test section component was provided by clamping bars installed in both the North-South and East-West directions.

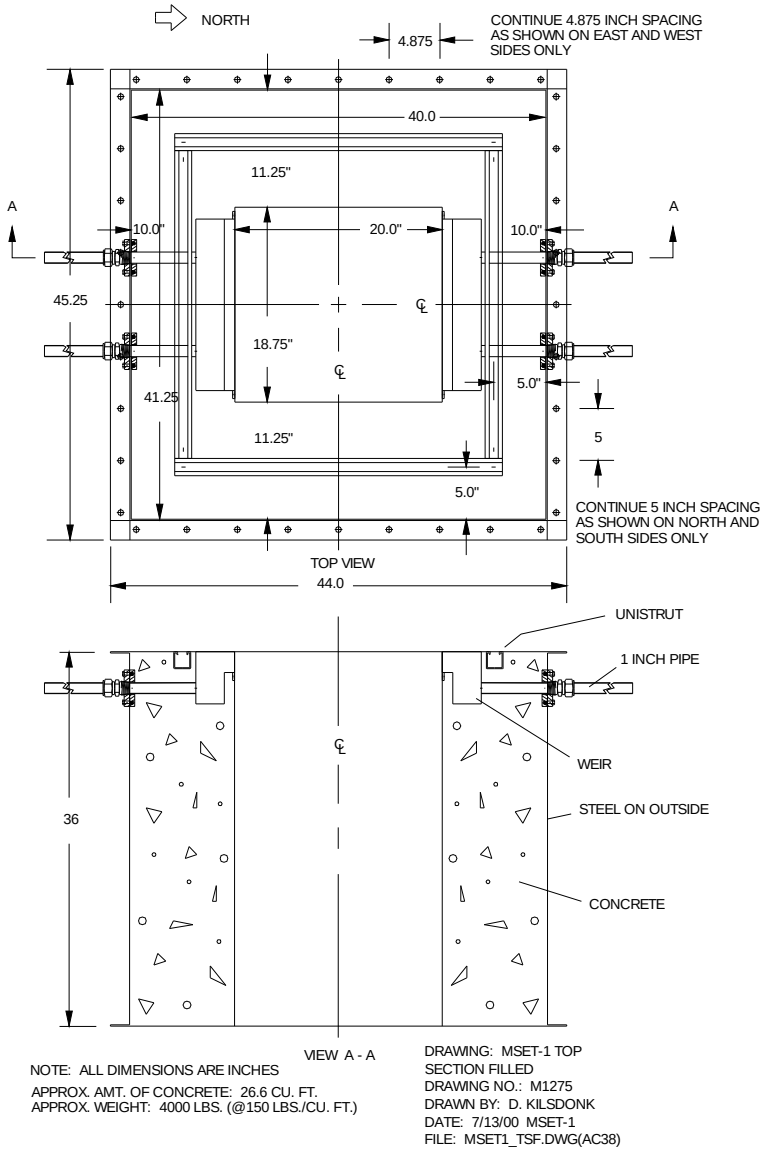

Figure 2-12. Details of the Top Test Section Showing Water Weirs.

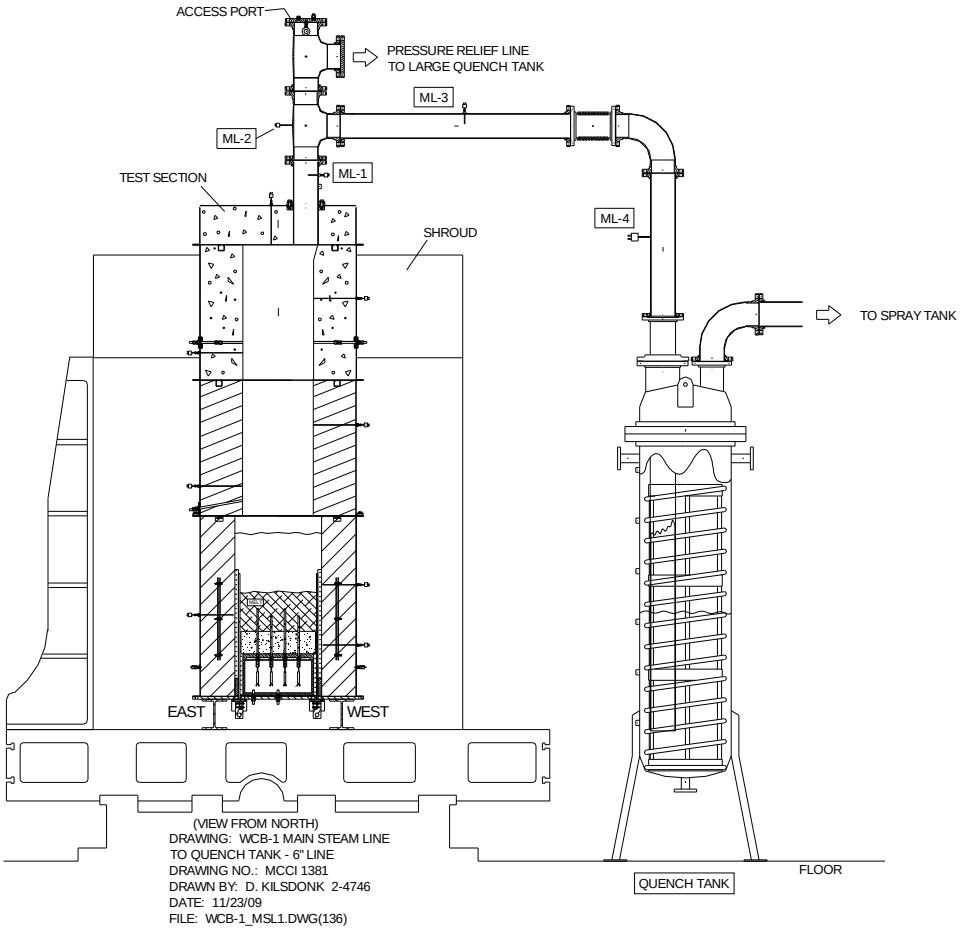

Figure 2-13. Illustration of WCB-1 Test Section Mounted on ZPR-9 Reactor Bed.

2.1.2 Basemat Water Supply System

A schematic illustration of the basemat water supply system is shown in Figure 2-14. The instrumentation locations are also shown in this figure. As previously noted, the water supply and return lines to the basemat were brought in through the test section base support plate. Each channel was equipped with an independent water measurement and control system that included both manual and remote isolation valves and an ultrasonic flowmeter. Temperature rise across each channel was measured using Type K thermocouples. The channel piping was constructed from 1.3 cm ID tubing. The individual channel flowrate and water temperature rise data allowed the average heat flux to each channel to be calculated. Each channel was also equipped with a secondary supply line with manual and remote isolation valves that could provide additional water flow to selected channels during the test if excessive heatup was observed. Both the primary and makeup supply lines were fed from 3.9 cm diameter header manifolds, and vented through a common manifold of the same diameter. The bulk temperature rise across the supply and return manifolds and total mass flowrate allowed the average heat flux to the plate to be calculated for comparison to the local channel measurements determined by the heat flux meters and the individual channel mass flux/temperature rise measurements.

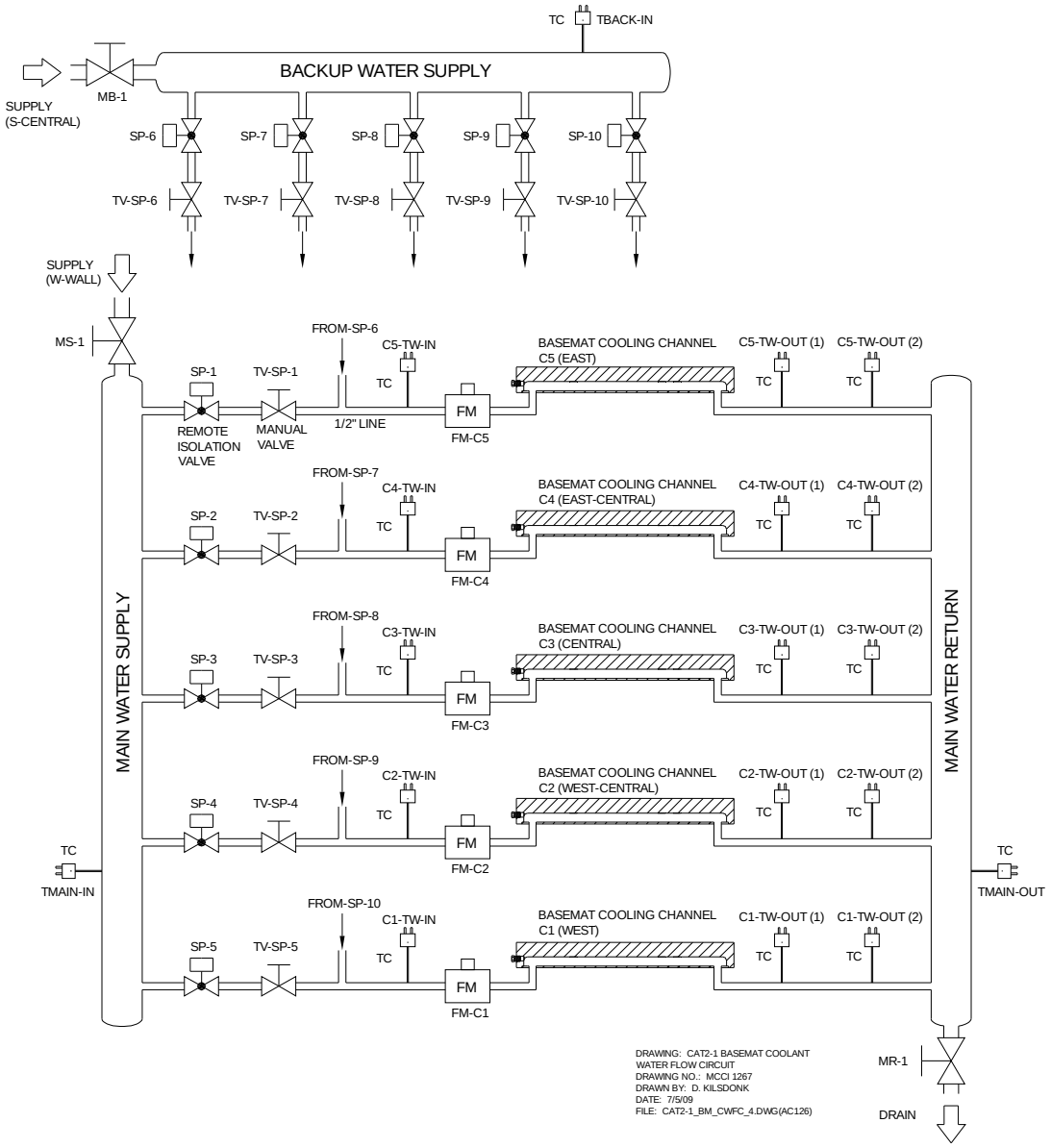

Figure 2-14. Basemat Water Channel Cooling Circuits.

Since the basemat water inlet and exits were from the bottom of the plate, this test could not investigate situations in which the bulk water outlet temperature approached saturation, otherwise the channels could potentially vapor-lock and cause premature test termination. Finally, given this design, it was important to vent the air out of the lines before the test section was fully assembled. As shown in Figures 2-4 and 2-7, each channel was equipped with a small (6.4 mm diameter) pipe plug that was mounted at the top of the channel on the inlet side. Prior to installing the test section sidewalls, the water lines were pressurized and the plugs loosened until all the air was vented and the plugs resealed. After this point, test procedures did not allow the water line return side isolation valves to be opened unless the inlet valves were opened and the lines pressurized. This prevented air from reentering the system.

2.1.3 Test Section Water Supply System

The water supply system consisted of a 1900 l capacity tank connected to the flooding weirs in the north and south sidewalls of the top test section through a valve-controlled supply line that provided water to the test section at a specified flow rate. A schematic illustration of the supply system is provided in Figure 2-15; details of the flooding weirs are shown in Figure 2-12. The supply system flowmeter, pressure transducer, level sensor, and thermocouple instrumentation locations are also shown in Figure 2-15. Water flow through the system was driven by a ~ 1 Bar differential pressure in the supply tank at a nominal flow rate of 120 lpm (2 l/s). The inlet water flow rate of 120 lpm corresponds to a melt/water heat flux in excess of 20 MW/m^2 based on a specific enthalpy of 2.6 MJ/kg for saturated steam at atmospheric pressure, assuming heat transfer occurs through boiling of the overlying coolant. The inlet water flow rate to the test section was monitored with a paddlewheel flowmeter. Both the initial water inventory (125 l) and makeup were provided through pneumatic ball valve RV-1, which was opened as needed at the control console to maintain the water volume inside the test section constant at 125 ± 13 l (50 ± 5 cm). A redundant supply line, activated by pneumatic ball valve RV-2, was provided in case RV-1 failed to open during the test. A third pneumatic valve, RV-3, was provided in case RV-1 or RV-2 failed in the open position. The test was initiated with valve RV-3 in the open position.

Note from Figure 2-15 that the supply line to the test section contained a manual bypass valve downstream of water injection valves RV-1 and RV-2. This valve was vented to a catch pan equipped with an alarmed water detector. During pretest procedures, this valve was left in the open position to divert any water leakage away from the test section. The alarm was intended to notify personnel that a leak was present so that corrective action could be taken. This valve was closed as one of the final steps of pretest operations prior to evacuation of the cell.

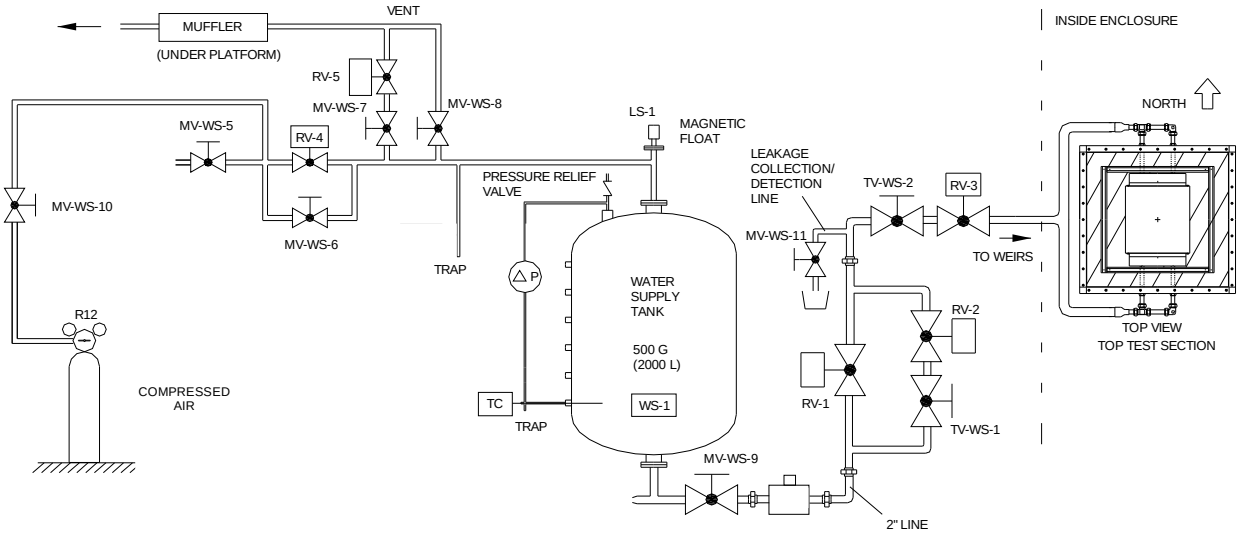

Figure 2-15. Test Section Water Supply System.

2.1.4 Quench System

The quench system, shown in Figures 2-16 and 2-17, consisted of a primary quench tank, a secondary spray tank, and a condensate overflow tank. The quench system flowmeter, pressure transducer, level sensor, and thermocouple instrumentation locations are also shown in these two figures. Steam and concrete decomposition gases passed from the test section through a 15 cm stainless steel pipe into the 680 l capacity, 60 cm ID primary quench tank. This tank contained an initial water inventory of 250 l. With this amount of water, a pool void fraction of ~ 60% could initially be accommodated before the voided water height reached the top of the tank. The quench tank was equipped with a 1.9 cm diameter cooling coil to remove heat from steam condensation, thereby maintaining a subcooled state.

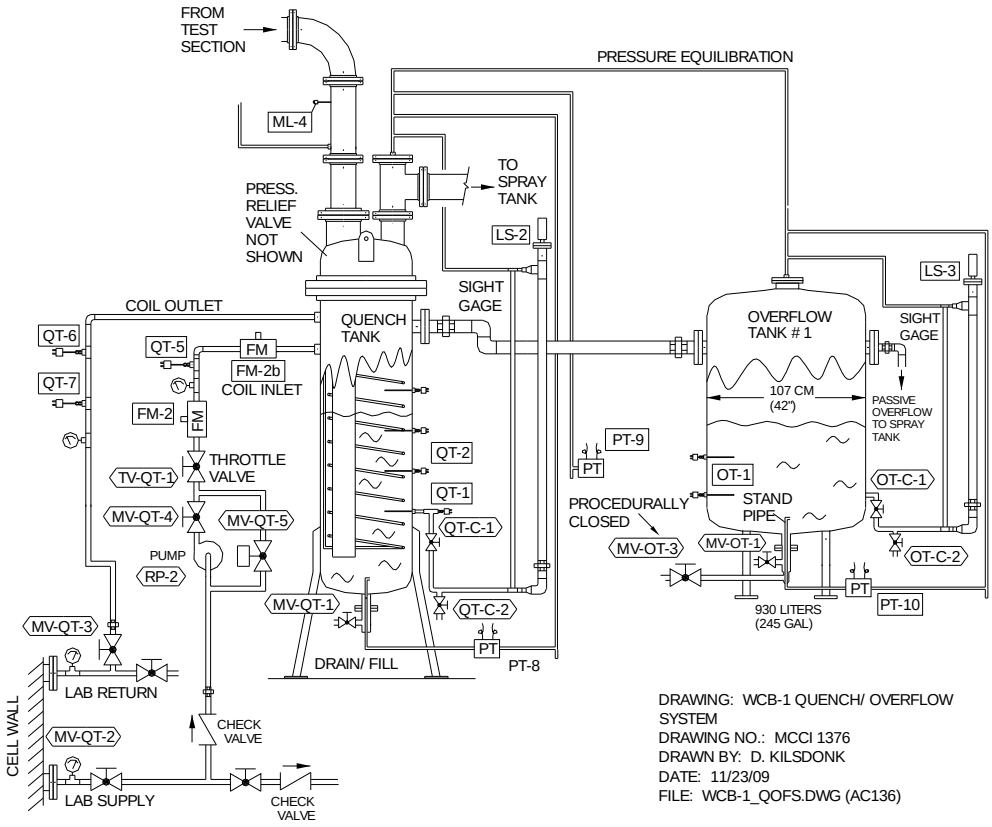

Figure 2-16. WCB-1 Quench and Overflow Tanks.

The secondary 1230 l capacity spray tank was connected to the quench tank by a 15 cm stainless steel pipe. In the event that the steam generation rate overwhelmed the primary quench tank, the secondary spray tank served to condense the remaining steam. This tank contained an initial water inventory of 375 l. With this amount of water, a pool void fraction in excess of 60% could be accommodated before the voided water height reached the top of the tank. The spray tank and interconnecting piping between the spray and quench tanks was also insulated to minimize heat losses.

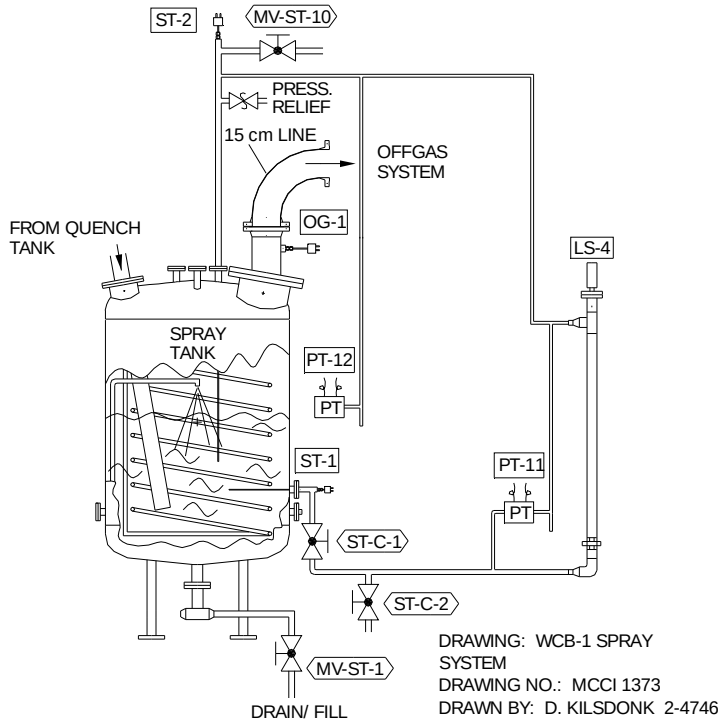

Figure 2-17. WCB-1 Spray Tank System.

2.1.5 Test Section Pressure Relief System

A pressure relief system was provided to prevent over-pressurization and possible failure of the test section. A schematic illustration of the system is shown in Figure 2-18. The system consisted of a 15 cm vent line from the test section to an auxiliary tank containing a nominal initial water inventory of 400 l. The auxiliary tank had an inside diameter of 1.22 m and a capacity of 4100 l. The tank was open to the atmosphere. The pressure relief line to the tank was equipped with a passive, counter-weighted check valve set to open at a differential pressure of nominally 68 kPa. A rupture diaphragm (68 ± 13.4 kPa differential failure pressure) upstream from the check valve prevented any flow through the line unless the pressure in the test section exceeded the design value of 68 kPa differential. As shown in Figure 2-18, the relief line was also equipped with a 7.5 cm vacuum breaker valve. This valve was provided to prevent water hammer from occurring due to stream condensation should the pressure relief valve open and then reseat after water had been introduced into the test section.

The initial 400 1water inventory in the auxiliary tank was provided to cool gases from the test section and to remove aerosols before any noncondensables present in the gas stream passed into the cell atmosphere. The tank was instrumented with a Type K thermocouple to measure water temperature and a differential pressure transducer to measure water depth. The instrumentation locations are shown in Figure 2-18. Water depth and temperature instruments were provided so that the steam condensation rate could be determined should the pressure relief valve open. In this manner, there would be no loss of data should the system activate.

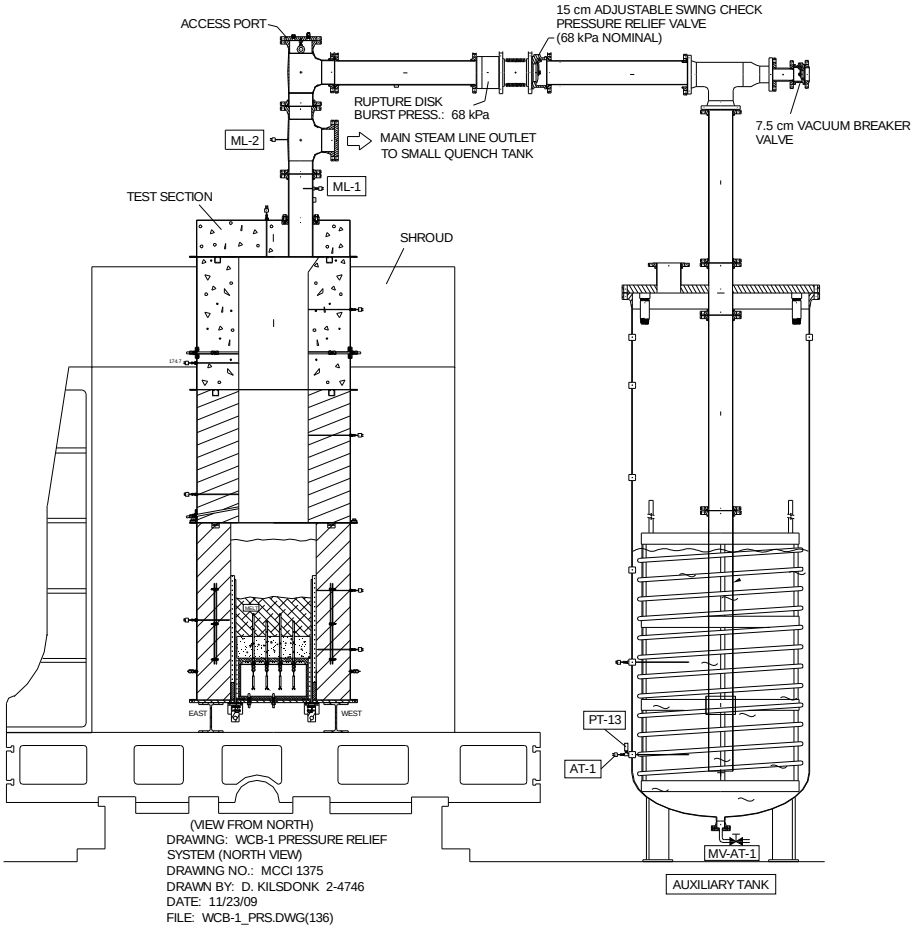

Figure 2-18. WCB-1 Test Section Pressure Relief System.

2.1.6 Off Gas System

An illustration of the off gas system is provided in Figure 2-19. This system filtered and vented the noncondensable concrete decomposition gases to the cell exhaust. The decomposition gases (H_2, CO, CO_2 and the cover gas) exited the spray tank and passed through a flow separator. The cleanup efficiency of the separator was 99% of all entrained solid and liquid when the particle size exceeded 10 microns. After passing through the flow separator, the flow could potentially split into two parallel off gas system lines. One line was constructed from 7.5 cm piping, while the second was made from 10.0 cm piping. The system was designed with the capacity to accommodate large-scale (up to 120 cm x 120 cm) tests. Since WCB-1 used a reduced scale 50 cm x 50 cm test section, the 7.5 cm side of the parallel off gas system was taken out of service using a blank-off plate at the branch point in the system (see Figure 2-19). As a result, all gas flow was diverted through the 10 cm side of the off gas system. The final filters in the system (4 individual filters per filter housing, yielding a total of 8 filters for each side of the off gas system) removed any remaining particulate before venting the off gases through the flowmeter to the cell atmosphere. The filters were equipped with a passive counter-weighted check valve set to open at a nominal differential pressure of 7 kPa. The bypass was provided in the event that the filters plugged during the experiment.

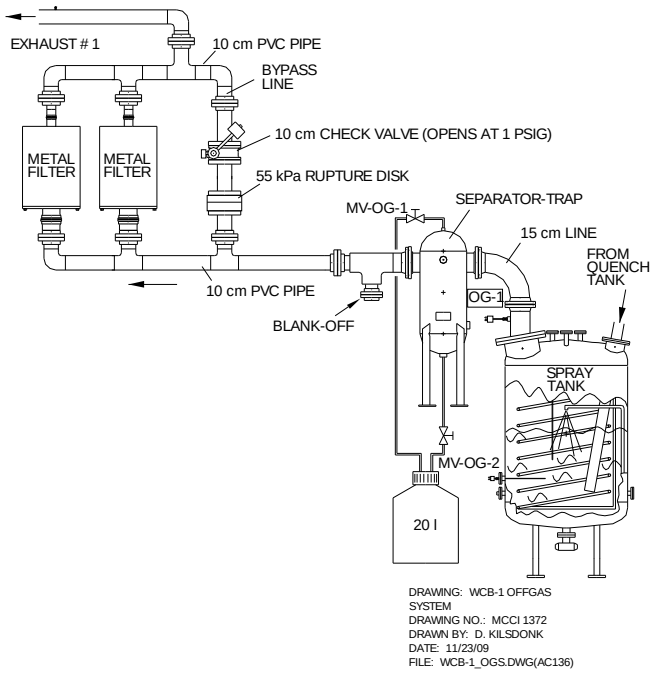

Figure 2-19. WCB-1 Off Gas System.

2.1.7 Cover Gas System

During the test a uniform flow rate of helium was fed into the test section to suppress burning of combustible concrete decomposition gases (H_2 and CO) and protect test section internals. An illustration of the cover gas system is shown in Figure 2-20. Cover gas flow was modulated by a total of three Hastings Flow Controllers (FC's). One 0-200 slpm FC provided cover gas to the lid camera and light port penetrations, while a second 0-350 slpm FC provided dedicated cover gas flow to the lid camera and optical pyrometer to prevent aerosol deposition on the camera and pyrometer quartz windows through which the melt upper surface was viewed. A third 0-100 slpm FC was used to inert the apparatus on the evening before the test.

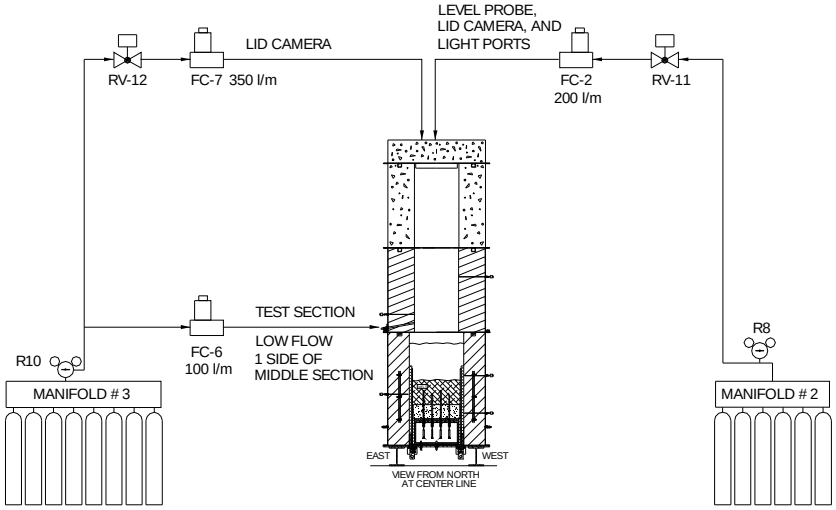

Figure 2-20. WCB-1 Cover Gas System.

2.1.8 Power Supply

The power for Direct Electrical Heating (DEH) of the corium was provided by a 0.56 MW single phase AC power supply made by NWL Transformers. Output of the power supply was voltage or current controlled. The supply had four voltage/current ranges: 56.4 V/10 kA, 113 V/5 kA, 169 V/3.3 kA, and 226 V/2.5 kA. The power supply was connected to the two arrays of tungsten electrodes in the test section through water cooled copper pipes that passed through a wall of the former reactor fuel loading compartment. The calculated total voltage drop through the water cooled copper pipes and tungsten electrodes at operational temperature and maximum current was less than 0.5 V. The leakage current through the overlying water pool during test operation has been estimated to be less than 1% of the total current.

2.1.9 Corium Composition

As shown in Table 1-1, the corium composition for WCB-1 was specified to contain 8 wt % calcined siliceous concrete as an initial constituent. As part of the developmental work for the CCI-1 experiment [25], a specific thermite was developed to produce this particular melt composition. The thermite reaction was of the form:

$$1.22U_3O_8 + 3.3Zr + 0.58Si + 1.14SiO_2 + 0.026Mg + 0.36\,CaO + 0.12Al + 1.842CrO_3 \rightarrow$$

$$3.66UO_2 + 3.3ZrO_2 + 1.72SiO_2 + 0.026MgO + 0.91CaO + 0.36Al_2O_3 + 1.842Cr;$$

$$Q = -252.2 \text{ kJ/mole } (1.71 \text{ MJ/kg});$$

$$T_{adiabatic} = 2572\ ^\circ C$$

$$T_{actual} \sim 2100\ ^\circ C$$

The bulk composition of the melt produced from this reaction is summarized in Table 2-1, while the detailed pre- and post-reaction compositions are provided in Table 2-2. Note that the pre- and post-reaction compositions do not include the mass of the UO_2 pellets that were used to line the test section MgO sidewalls; see Figures 2-2 and 2-3. This material did not participate in the initial exothermic chemical reaction, and remained essentially intact as a protective layer during the test.

The 400 kg thermite charge was packed into the test section in a large, 1.7 mil aluminized Saran bag that was pre-installed over the basemat. The thermite was packed in the bag to prevent water absorption by CrO_3 and concrete oxides (principally CaO and SiO_2), since these constituents are hygroscopic. Any moisture absorbed by the thermite is converted to H_2 gas that not only degrades the burn process, but results in combustible gas generation that is unrelated to the scientific aspects of the experiment.

Table 2-1. Post-Reaction Bulk Composition for WCB-1 Thermite.

Constituent	Wt%
UO_2	60.97
ZrO_2	25.04
Calcined Concrete	8.08[b]
Cr	5.91

[b]Calcined siliceous concrete: 79.0/0.9/15.4/4.7 wt% SiO_2/MgO/CaO/Al_2O_3

Table 2-2. Detailed Pre- and Post-Reaction Compositions for WCB-1 Thermite.

Constituent	Reactant		Product	
	Wt%	Mass (kg)	Wt%	Mass (kg)
U_3O_8	63.38	253.52	-	-
UO_2	-	-	60.97	243.88
Zr	18.53	74.12	-	-
ZrO_2	-		25.04	100.16
Si	1.00	4.00	-	-
SiO_2	4.23	16.92	6.38	25.52
Mg	0.04	0.16	-	-
MgO	-	-	0.07	0.28
Al	0.20	0.80	-	-
Al_2O_3	-	-	0.38	1.52
CaO	1.25	5.00	1.25	5.00
CrO_3	11.37	45.48	-	-
Cr	-	-	5.91	23.64
Total	100.00	400.00	100.00	400.00

Table 2-3. Engineering Composition of WCB-1 Siliceous Concrete Basemat.

Constituent	wt %	Size Distribution
Aggregate	47.4	5-8 mm: 16.6 wt % 8-11 mm: 20.4 wt% 11-16 mm: 10.4 wt%
Sand	30.6	0-2 mm: 12.2 wt % 2-4 mm: 18.4 wt %
Type 1 Cement	15.3	N/A
Tap Water	6.7	N/A

2.1.10 Concrete Composition

The composition of the WCB-1 concrete was siliceous. The mix was identical to that used in the CCI-3 experiment [26]. The engineering composition for this particular concrete type is shown in Table 2-3. The sand and aggregate were supplied by CEA as an in-kind contribution to the program. The chemical composition for this concrete is provided in Table 2-4. These data are based on analysis of a specimen taken from the CCI-3 concrete archive sample [2]. The concrete density was determined to be 2270 kg/m^3 from the archive sample using the standard weight-volume method.

2.1.11 Instrumentation and Data Acquisition

The WCB-1 facility was instrumented to monitor and guide experiment operation and to log data for subsequent evaluation. Principal parameters that were monitored during the course of the test included the power supply voltage, current, and gross input power to the melt; melt temperature and temperatures within the concrete basemat and water-cooled basemat plate; supply water flow rate to the basemat and to the test section; water volume and temperature within the test apparatus, and water volume and temperature within the quench system tanks.

Other key data recorded by the DAS included temperatures within test section structural sidewalls, melt/crust upper surface temperature, off gas temperature, and pressures at various locations within the system. Measurement uncertainties for the various instruments that were used in the test are summarized in Table 2-5.

Table 2-4. Chemical Composition of Siliceous Concrete (CCI-3 basis [2]).

Constituent	Wt %
SiO_2	60.99
CaO	17.09
Al_2O_3	3.61
Fe_2O_3	1.52
MgO	0.87
MnO	0.04
SrO	0.04
TiO_2	0.16
SO_3	0.44
Na_2O	0.67
K_2O	0.83
CO_2	9.98
H_2O	3.76[a]

[a]Free water content is 2.33 wt % while bound water content is 1.43 wt %.

Table 2-5. Summary of Data Measurement Uncertainties for WCB-1.

Measurement	Instrument	Accuracy
Temperature (other than melt)	Type K thermocouple	± 2.2 ºC or ± 0.75 %
Temperature (melt)	Type C thermocouple	± 4.5 ºC or ± 1.0 %
Temperature (corium upper surface)	Two-color optical pyrometer	± 4.0 ºC
Pressure	Pressure transducer	Differential: ±0.4 kPa Absolute: ± 2.0 kPa
Water flowrate	Basemat channel and quench tank coil: ultrasonic flowmeters	± 0.3 lpm
	Test section supply and quench tank coil: paddlewheel flowmeters	± 4 %
Basemat heat flux	Heat flux meter	± 5%
DEH input power	Hall effect meter	± 0.2 %
Power supply voltage	Digital voltmeter	±0.008 %
Tank water volume	Magnetic float	± 2 l for quench tank; ± 5 l for all other tanks
Debris-water heat flux	Calculated based on steaming rate as measured by quench tank level float.	± 10 %[a]

[a]Primary contributor is corium surface area (9%)

All data acquisition and process control tasks were managed by a PC executing LabVIEW 8.2 under Windows XP. Sensor output terminals were connected inside the test cell

to model HP E1345A 16-channel multiplexers that were integrated into a mainframe chassis in groups of eight. An illustration of the DAS setup is provided in Figure 2-21. The multiplexers directed signals to an HP E1326B 5 ½ digit multimeter incorporated into each chassis. Three independent 128 channel systems exist as part of the facility; two of these were used for WCB-1.

Signal noise was reduced by the digitizer through integration over a single power line cycle (16.7 ms). The digitized sensor readings were routed from the test cell to the PC in the control room via two HP-IB extenders. The extenders allowed the ASCII data from the HP to be sent through the cell wall over a BNC cable. The extender within the control room then communicated with a GPIB card within the PC. This configuration also permitted remote control of the multimeter through LabVIEW.

Integration of the signals over the period of a power line cycle limited the speed with which the multiplexer could scan the channel list. The minimum time for the digitizer to scan the list was ~1.7 s (16.7 ms • 100 channels/chassis for this test). Though the three systems operate independently, implying the ability to update all 300 channels in roughly two seconds, the actual time required for the update was about 5 seconds.

The basemat for WCB-1 was instrumented to monitor melt temperature during both the concrete ablation and plate-cooling phases of the test using multi-junction Type C thermocouples in tungsten thermowells. In addition, a two-color optical pyrometer was used to measure the debris upper surface temperature during periods when aerosol production did not optically occlude the view of the surface. Multi-junction Type K thermocouples cast directly into the basemat were also used to track the location of the concrete ablation front during the concrete erosion phase of the test. Plan and elevation views of the basemat thermocouple layout are provided in Figures 2-22 and 2-23. The water-cooled basemat and basemat water supply system (Figure 2-14) were instrumented to provide local and global heat transfer performance data.

The water supply tank was equipped with a magnetic float to measure the time-dependent water level. As a redundant level measurement technique, the supply tank was also equipped with a differential PT. Water flow rate to the test section was monitored by a paddlewheel flowmeter. The location of the supply system instrumentation is shown in Figure 2-15.

The quench, overflow, and spray tanks were instrumented to measure the transient energy deposition due to steam generation from corium quenching in the test section. The quench and overflow tank instrument locations are shown in Figure 2-16, while the spray tank instrumentation is shown in Figure 2-17. Each tank was equipped with a magnetic float and (redundant) differential PT to measure the accumulating water volume due to steam condensation. Transient water temperatures in all tanks were monitored using Type K TC's (two in the quench and spray tanks and one in the overflow tank). Water flow rate and temperature differential across the quench tank cooling coil were monitored with a paddlewheel (and redundant ultrasonic) flowmeter and Type K TC's, respectively, thus providing a measurement of the time-dependent energy extraction rate from the water mass in the tank. The main steamline between the test section and quench tank was instrumented with Type K TC's to measure the local gas and pipe structure temperatures. The steamline thermocouple locations are shown in Figure 2-13.

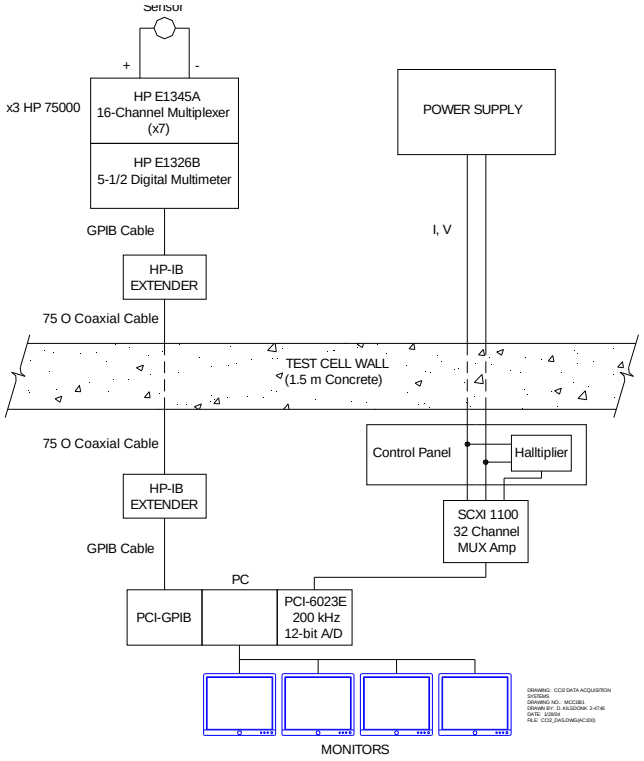

Figure 2-21. Data Acquisition System Setup for WCB-1.

The test section sidewalls and upper lid were also instrumented with a total of 20 Type K and Type C thermocouples to measure the sidewall heat up prior to water addition, and also to measure the sidewall cooling rate above the melt surface after water was added. Illustrations of the TC locations in the test section sidewalls are provided in Figures 2-24 and 2-25.

One method for monitoring water level in the test section was provided by a differential level probe which was inserted through a sealed penetration in the lid. The probe was maintained in a retracted position during the dry ablation phase until water was added to the test section. After water addition, the probe was inserted to a distance of 63 cm from the initial basemat surface (38 cm from the initial collapsed melt surface). The probe tip was instrumented with two 1.6 mm diameter ungrounded junction Type K TC's which monitored plenum gas temperature prior to water addition; thereafter, the TC's monitored the water temperature over the melt surface. The probe tip locations after insertion are shown in Figure 2-26.

Aside from the insertable water level probe, two additional methods were provided to monitor the water volume in the test section. The first was a static water level port located in the North sidewall 70 cm from the initial basemat surface (45 cm from the initial collapsed melt surface). The port location is shown in Figure 2-26. The second method was provided by an on-line calculation of the water volume in the test section based on conservation of mass; i.e., the water volume in the test section at any time was equal to the initial volume in the supply/quench system tanks minus the volume in the same tanks at the current time.

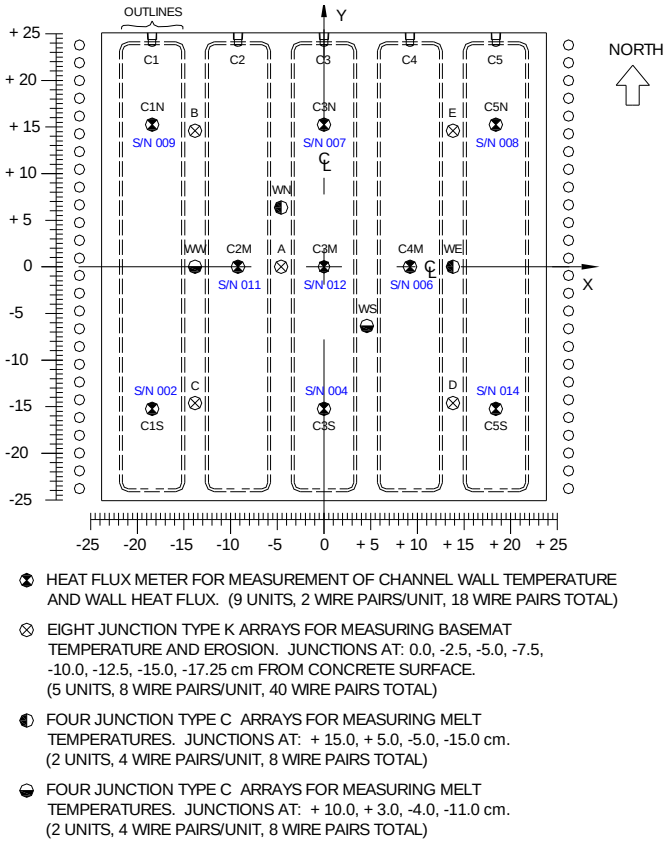

Figure 2-22. Plan View of Basemat Instrumentation Layout (dimensions are in cm).

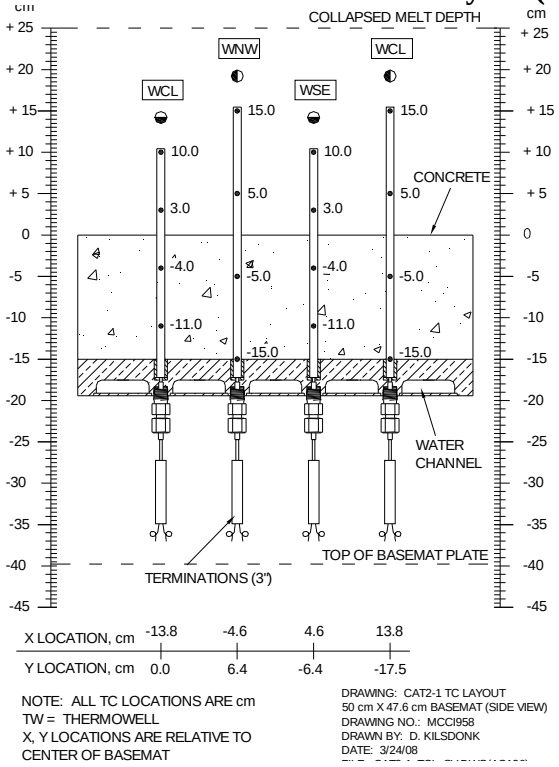

Figure 2-23. Elevation View of Basemat Type C Thermocouple Locations.

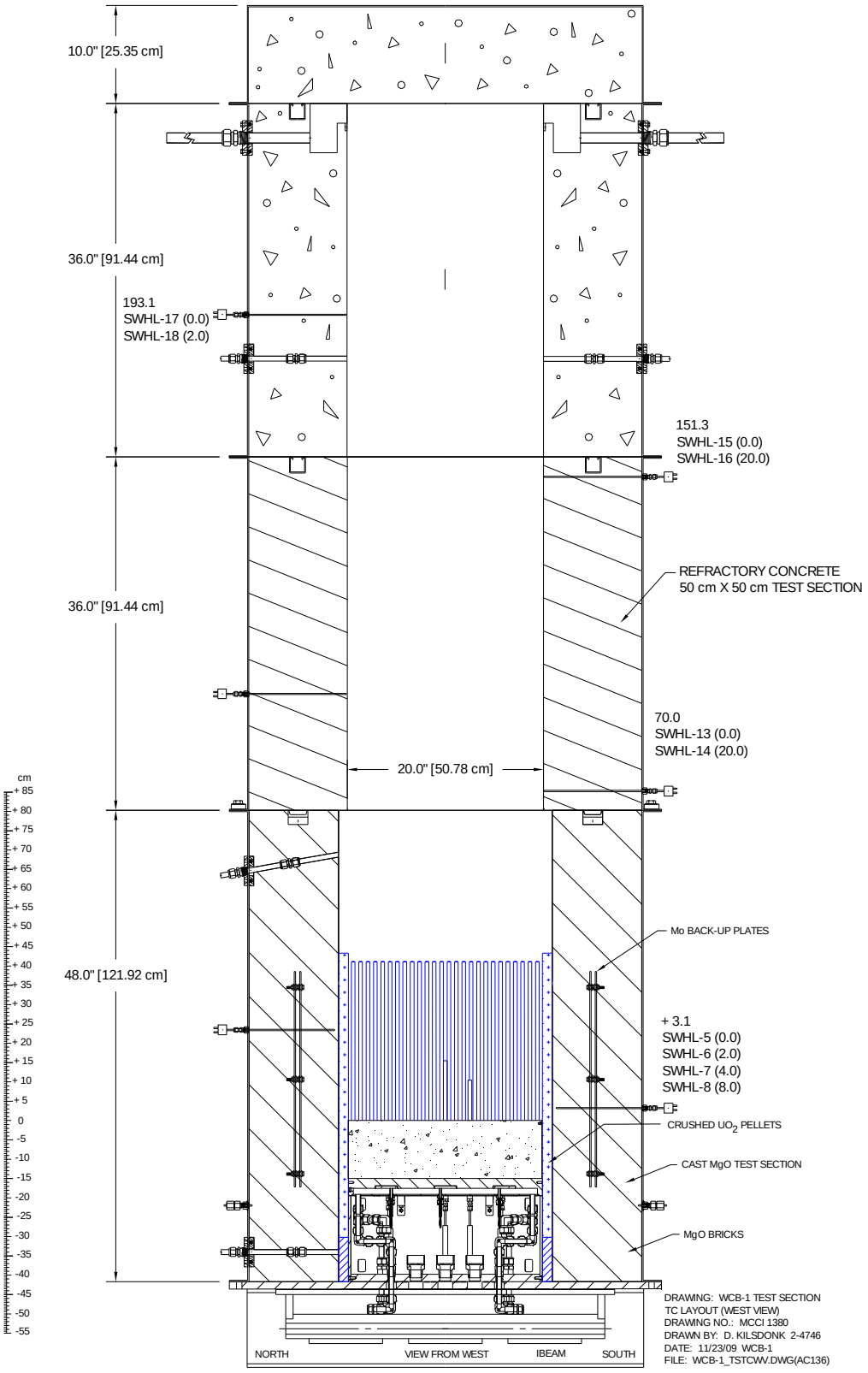

Figure 2-24. WCB-1 Test Section Sidewall Instrumentation (View from West).

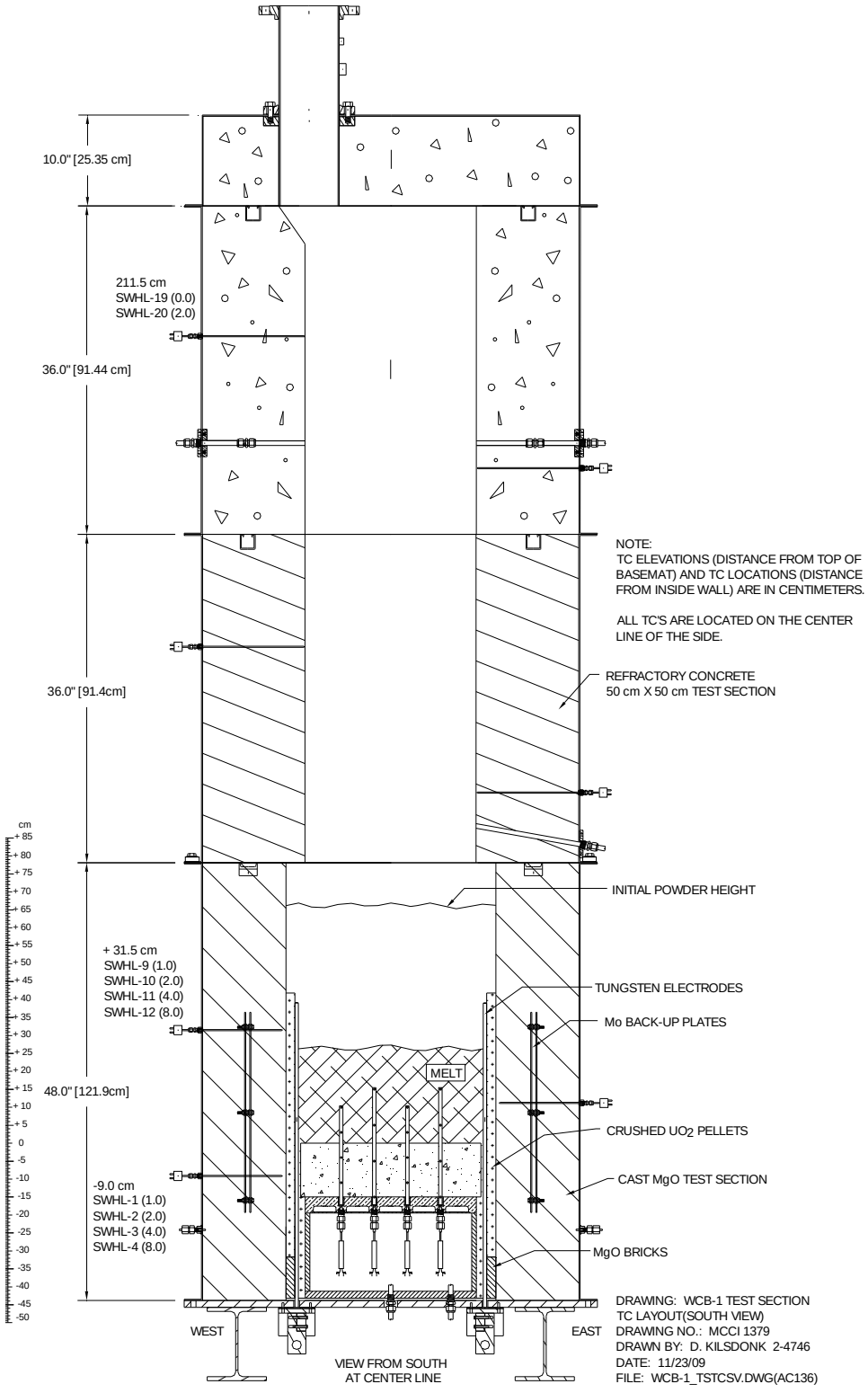

Figure 2-25. WCB-1 Test Section Sidewall Instrumentation (View From South).

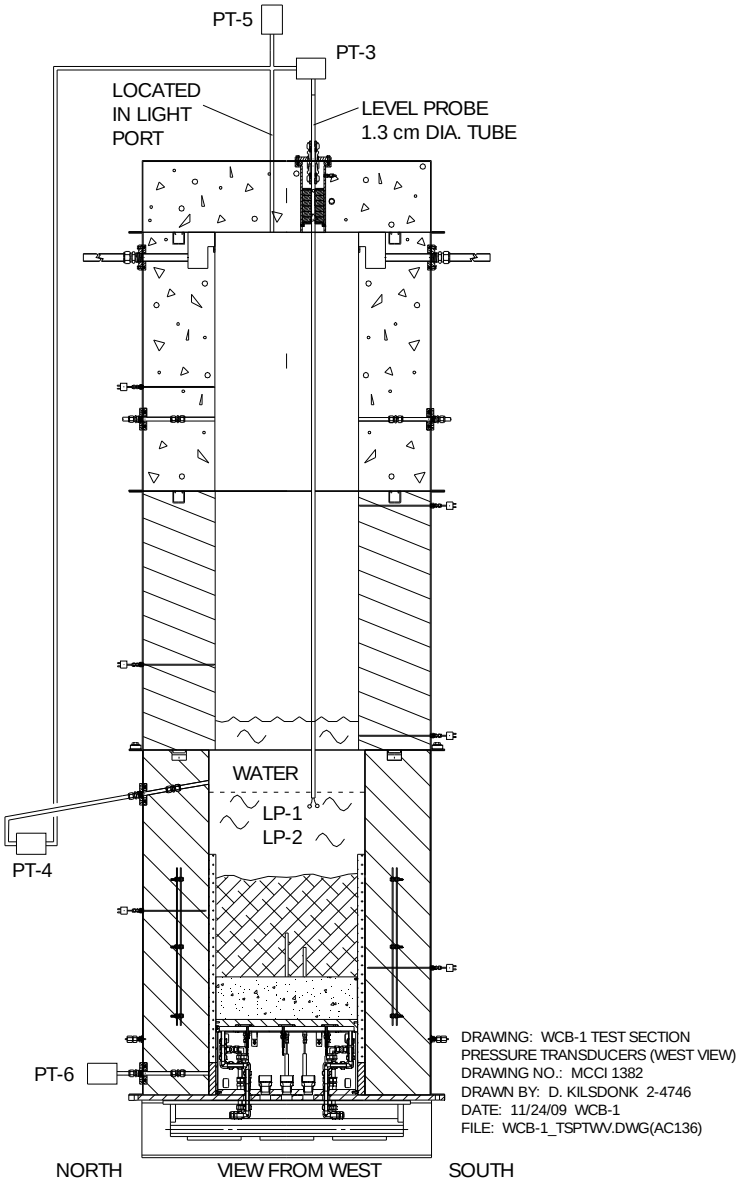

Figure 2-26. WCB-1 Test Section Pressure Transducer Layout.

Key system pressures were monitored with strain-gauge type pressure transducers manufactured by Sensym, Inc. As shown in Figures 2-15 through 2-17 and 2-26, the pressure in all system tanks were monitored, as well as the test section plenum pressure. An additional PT was located in the lower test section to monitor the pressure beneath the melt upper surface. This transducer was mounted on the north sidewall of the test section at an elevation of 46 cm beneath the initial concrete surface (see Figure 2-26). The gap between the MgO sidewalls and the electrodes was packed with crushed UO_2 pellets during corium loading. Thus, this PT could sense the pressure beneath the melt surface as long as the gap did not plug during the test.

In terms of the power supply operating parameters, voltage drop across the tungsten electrode bank was monitored with the DAS voltmeter, while current input was monitored with

two 5000:1 current transformers. Power input to the melt was monitored with two Hall Effect meters.

In addition to the above instrumentation, visual information regarding the core-concrete interaction and melt quenching behavior was provided by a video camera mounted on the upper lid of the apparatus. Five area video monitors were also used in the cell to monitor for leaks, and to record any disruptive events (e.g., steam explosion) should one occur.

2.2 Test Procedures

2.2.1 Pretest Preparations

Assembly of the apparatus began through the installation of tungsten electrodes into machined copper electrode clamps. The electrode clamps were then attached to the bottom of the 2.54 cm thick aluminum support plate, which served as the foundation for the entire apparatus. With the electrode clamps installed, the support plate was moved into position on the test stand. The water-cooled basemat was then installed, plumbed up to the supply and return water manifolds, vented of air, and then leak checked. Once these steps were completed, the four sidewalls were set in place on the support plate. The lower section flange bolts and clamping bars were then installed and tightened. Following this step, the basemat instruments were connected to terminal boxes that were prewired to the data acquisition system.

In parallel with test section assembly, the thermite powders were mixed in preparation for corium loading. As a precursor for initiating mixing, a gas sample test was conducted to verify that the initial level of volatile impurities in a sample prepared from the WCB-1 thermite constituents was sufficiently low to preclude excessive gas release during the burn. The results of this test were positive, and on this basis, mixing was initiated.

Once the lower section is assembled, preparations for loading of the corium charge were initiated. A single large 1.7 mil aluminized Saran bag was preinstalled over the basemat. During loading, the 400 kg thermite charge was placed within this bag in order to reduce the amount of bagging material present in the thermite. As the powders were placed in the test section, the basemat melt temperature thermocouples were monitored to detect any localized heating in the corium powders. If heating was observed, the cell was to be evacuated immediately. As the thermite was placed, the gap between the tungsten electrodes and MgO sidewalls was filled with crushed UO_2 pellets. The crushed pellets served as a protective layer against excessive chemical/thermal attack by the corium during the test. Once loading was completed, two sparkler igniters were placed a few centimeters below the top of the powders near the center of the test section, and then the bag was folded and sealed.

Once loading was completed, a removable train containing a 2.0 kg bagged sample of thermite was installed over the powder bed. The sample train was removed weekly and the sample weighed to monitor the moisture pickup by the thermite during the period between loading and test initiation. The train also contained a 4.5 kg canister of desiccant. The desiccant was provided to maintain the plenum gas as dry as possible during pretest operations. As an additional measure to prevent moisture accumulation in the powder bed, the lower test section

was continuously purged with argon (2 slpm) from the time loading was completed until the test was initiated.

Once loading was completed, the remainder of the test apparatus was assembled. This included installation of the two upper sections and the enclosure lid. Peripheral instruments were then installed and connected to terminal boxes. The main gas line from the test section to the quench tank was installed, as well as the pressure relief line from the test section to the auxiliary tank. (The main steamline was closed off from the test section using an insertable blank-off plate throughout pretest operations to preclude moisture migration from the quench tank back into the test section).

After assembly was completed, extensive system checkout procedures were performed to ensure that the facility was in proper working order. This included a proof test of the test section at 83 kPad, which is 20 % in excess of the pressure relief system activation pressure of 69 kPad. The pressurization gas for this test was argon. An insertable blind flange was installed upstream of the rupture disk in the pressure relief line to isolate this system. During the test, the apparatus was gradually pressurized to the proof pressure. After a 1 minute hold at this pressure, the system was isolated to determine the leak rate. The leak rate of the WCB-1 test section was found to be 2.0 kPa/min (8 slpm) at a nominal pressure of 55 kPad, which was significantly below the acceptable leak rate of the fully assembled test section (i.e., < 2 % of the expected peak gas/vapor generation rate during the test).

Pretest preparations for WCB-1 culminated with a final full system checkout that involved remotely running all equipment with the power supply in operation across a water cooled dummy load. Once the full system check was completed, final system preparations were carried out. These efforts included: (i) hookup of the power supply to the tungsten electrodes through water cooled buss bars, (ii) installation of the final piping connection between the water supply tank and the test section, and (iii) removal of the sample train from within the test section. Following connection of the power supply to the electrode clamps, the key for the power supply lockout located in the cell, as well as the key for the interlock located on the control room console, were assigned to a custodian who kept the keys in their possession until the test was initiated. This step was taken to preclude inadvertent activation of the power supply.

2.2.2 Test Operations

The planned test operating procedure is described first, followed by a summary of the actual operating procedure.

As shown in Table 1-1, initial target power for the core-concrete interaction phase was 80 kW. After melt formation, the input power would be held constant at 80 kW until the concrete was eroded to a depth of 12.5 cm, as evidenced by thermocouple readings near the bottom of the concrete. Once the concrete ablation depth reached 12.5 cm, leaving a concrete layer 2.5 cm thick over the water-cooled basemat, the cavity would be flooded and the input power held constant at the 80 kW level until the system came to thermal equilibrium. The determinants for thermal equilibrium would be that the steaming rate from the test section, as well as the melt and water channel exit temperatures, remained stable for 15 minutes. After the initial operating stage at a constant power level of 80 kW, the power would be gradually reduced in 10 kW intervals

and the system would be allowed to equilibrate at each new power level. After each adjustment, the power supply would be run in a constant voltage mode for a period of ~ 15 minutes to look for the possibility of water ingression, as would be evidenced by reducing input power at constant voltage.[b] Operation in this manner would continue until the input power was reduced to zero, either by gradual quench, or by periodic operator reductions in power level.

WCB-1 was performed on 29 July 2009. On the evening prior to the experiment, the apparatus was inerted with a slow bleed of helium into the test section. On the day of the experiment, the apparatus was brought up to operating conditions, a final walk through inspection was performed by operating personnel, the thermite igniter was hooked up, and finally the power supply was energized before the containment was evacuated and sealed. Data acquisition was initiated at 4:47 pm. Coolant and cover gas flows were brought up to design conditions, and the cell ventilation system was closed and sealed per test procedures.

The event sequence for WCB-1 is provided in Table 2-6. In the discussion that follows, time t = 0 corresponds to melt contact with the concrete basemat. The criterion used to define the onset of concrete ablation at a given location was that the local temperature reached the siliceous concrete liquidus temperature of 1250 °C [27].

As shown in Table 2-6, data acquisition began at -31.3 minutes relative to initial melt contact with the basemat. Power was applied to the nichrome wire/sparkler located at the top of the powder charge at -1.1 minutes. Based on video camera data from the test section and plenum gas temperature readings, thermite ignition was announced and logged in the control room at -0.7 minutes. Based on readings from the Type K thermocouples cast flush with the concrete basemat surface (Figures 2-22 and 2-27), the burn front reached the bottom of the powder bed and contacted the concrete in ~ 40 seconds (i.e., at 0.0 minutes), which was within the planning basis for the experiment. The readings from selected melt temperature thermocouples are shown in Figure 2-28 over the first few minutes of the interaction. As is evident from this collection of data, peak melt temperatures near the center of the melt over the first minute were in the range of 1900 to 1960 °C, with the average being close to 1950 °C.

As shown in Figure 2-29, DEH input power was stabilized at the initial target level of 80 kW by 2.1 minutes. The power was maintained relatively constant at this level until the first reduction at 145.2 minutes. By 5.0 minutes, aerosols in the test section plenum cleared sufficiently to reveal the debris surface. The melt pool was quiescent, and was covered with an overlying stable crust. At 18.6 minutes, aerosol production increased, and by 20.6 minutes, the view of the surface was again occluded. In general, aerosol production for this test was substantial, with limited views of the debris surface obtained in the time intervals from 23.3 to 25.5 minutes and from 59.3 to 64.3 minutes. Each of these views indicated a fairly quiescent melt pool covered by an overlying crust.

[b]Following concrete erosion, melt sparging would cease. As a result, the test conditions would resemble a water ingression test [3] but with sustained heating. Thus, when operating with constant voltage, the power should decrease as the material quenched if water ingression occurred. However, if the power did not fall appreciably, then the power level would be above the dryout limit. In this event, the power would be reduced in 10 kW intervals spaced at ~ 15 minute intervals until the power began to decrease at constant voltage. This would define the dryout limit for the melt, which would be additional data to add to the SSWICS water ingression database.

Table 2-6. WCB-1 Event Sequence (times relative to melt contact with basemat).

Shifted Time (Minutes)	Event
-31.3	DAS started.
-1.1	Power applied to thermite igniter wire.
-0.7	Thermite burn initiated; view of melt surface occluded by aerosol within 5 seconds.
0.0	Thermite burn completed (burn time ~ 40 seconds); melt temperature ~1950 °C
2.1	DEH input power stabilized at target level of 80 kW.
30.7-52.6	Onset of basemat ablation detected at basemat centerline and in all four quadrants.
86.6-99.5	Basemat ablation depth reached 2.5 cm; sharp increase in ablation rate.
103.3-105.5	Basemat ablation depth reached 12.5 cm at centerline and in southwest quadrant (A and C array locations); preparations for cavity flooding initiated.
106.1	Water addition to test section initiated. Intermittent sparks observed from melt surface for ~ 1 minute, then the surface darkened for the rest of the test. Initial debris cooling rate was 3.3 MW/m^2, then steadily declined below 500 kW/m^2 at 120 minutes.
108.3	Makeup water added to test section (makeup water added at 110.2, 115.1, 132.9, 149.9, 173.3, 209.1, and 229.2 minutes)
130.0	Melt temperatures stabilized in the range of 1700 – 1900 °C. Debris/water heat flux falls to 370 kW/m^2 (DEH input power equivalent to 320 kW/m^2). Plate upper surface temperatures at 4 out of 5 locations stabilized in the range of 100-250 °C. Heat fluxes to the plate were low; 10-20 kW/m^2. Power split biased heavily upwards.
134.8	Basemat ablation depth reached 12.5 cm in northeast quadrant (E array location)
137.1	Input power reduced to 70 kW; constant voltage operation initiated (47 volts). Backup water flows in channels C3, C4, and C5 started; channel flowrates increased from ~ 10 to 12 lpm.
145.2	Plate surface temperature in northeast quadrant continued to hover near 800 °C; input power reduced to 40 kW. Constant voltage operation resumed (39 volts).
152.0	Plate surface temperature in northeast quadrant (E array location) fell below 600 °C and continued to decline thereafter.
145.0 – 165.0	Melt temperatures scattered (1600-1950 °C). Debris-water heat flux declined to 150 kW/m^2 and stabilized. Plate temperature in northeast quadrant declined steadily, while temperature near centerline approached 500 °C. All other plate temperatures were < 400 °C. Plate heat fluxes ranged from 10 to 40 kW/m^2, with an average near 20 kW/m^2. Power split remained biased heavily upwards.
169.5	Basemat ablation depth reached 12.5 cm in northwest quadrant (B array location)
168.2-181.5	Plate surface temperature in northwest quadrant (junction B-7 in B array) recorded a steady increase in local temperature from 223 °C to 743 °C over the time interval; heating rate was ~ 40 °C/minute.
178.4	Input power reduced to 20 kW; constant voltage operation resumed (29 volts).
178.4-194.6	Melt temperatures scattered in the range of 1700-1900 °C. Plate surface temperature in northwest quadrant stabilized in the range of 750 – 780 °C before starting gradual decline. Debris-water heat flux declined steadily to ~ 120 kW/m^2 and stabilized. Local plate heat fluxes were in the range of 10 – 25 kW/m^2. Power split remained biased heavily upwards.
194.6	Input power reduced to 10 kW; constant voltage operation resumed (25 volts).
194.6 – 227.0	Melt temperatures steadily declined to 1500 – 1600 °C at the end of the period. Debris cooling rate also fell from 120 to 75 kW/m^2. Input power at constant voltage declined to < 2 kW. Local plate heat fluxes remained in the range of 10 – 25 kW/m^2. Power split remained biased heavily upwards.
227.0	DEH input to melt terminated.
230.3	Data acquisition terminated.

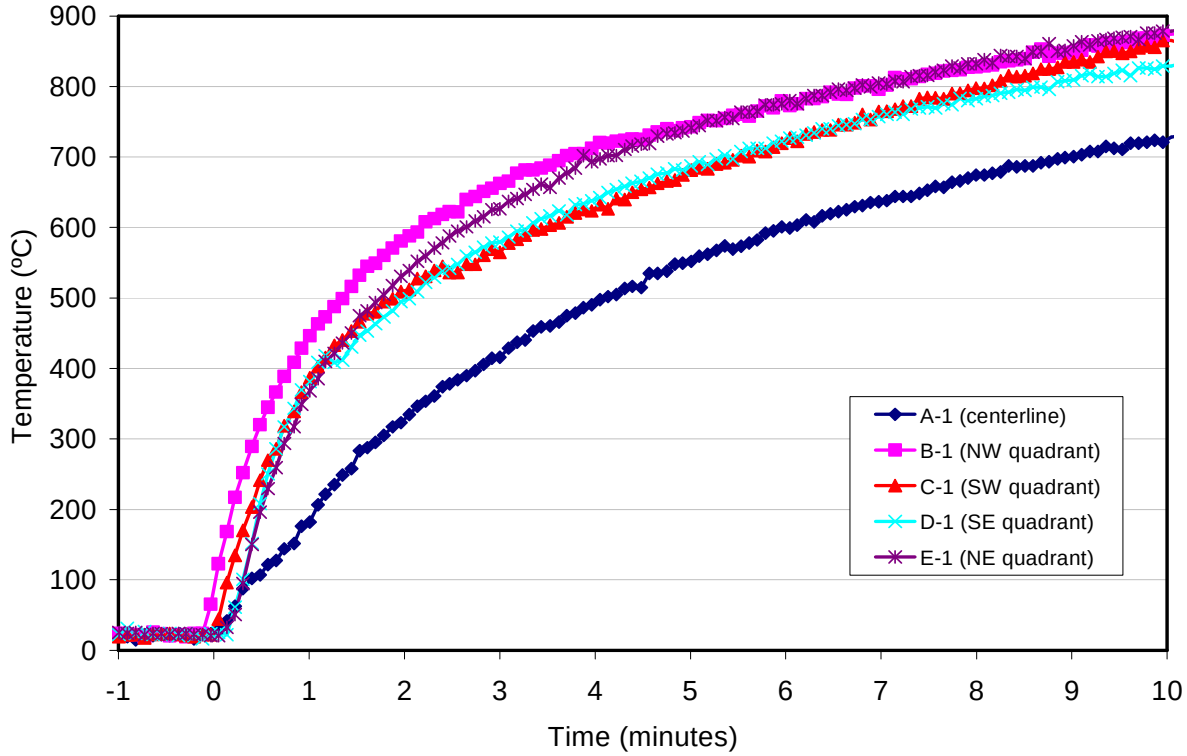

Figure 2-27. Concrete Surface Temperatures over the First 10 Minutes of the Interaction.

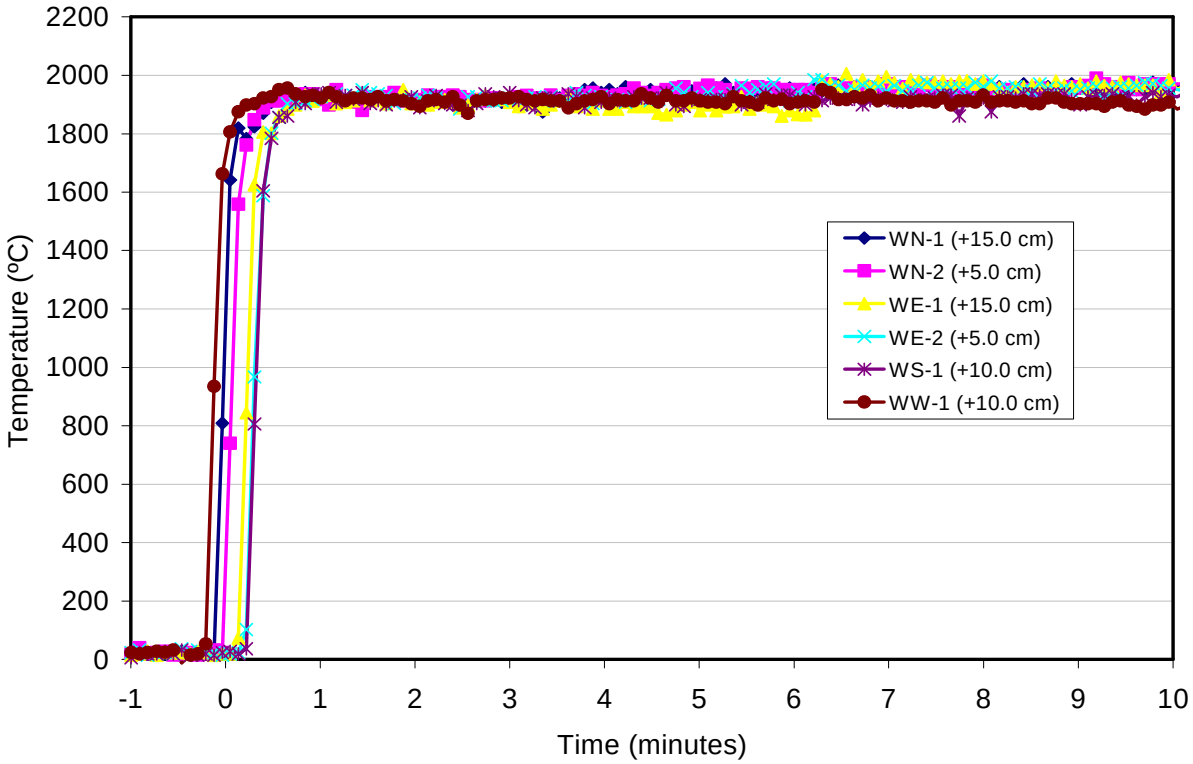

Figure 2-28. Bulk Melt Temperature Data over the First 10 Minutes of the Interaction.

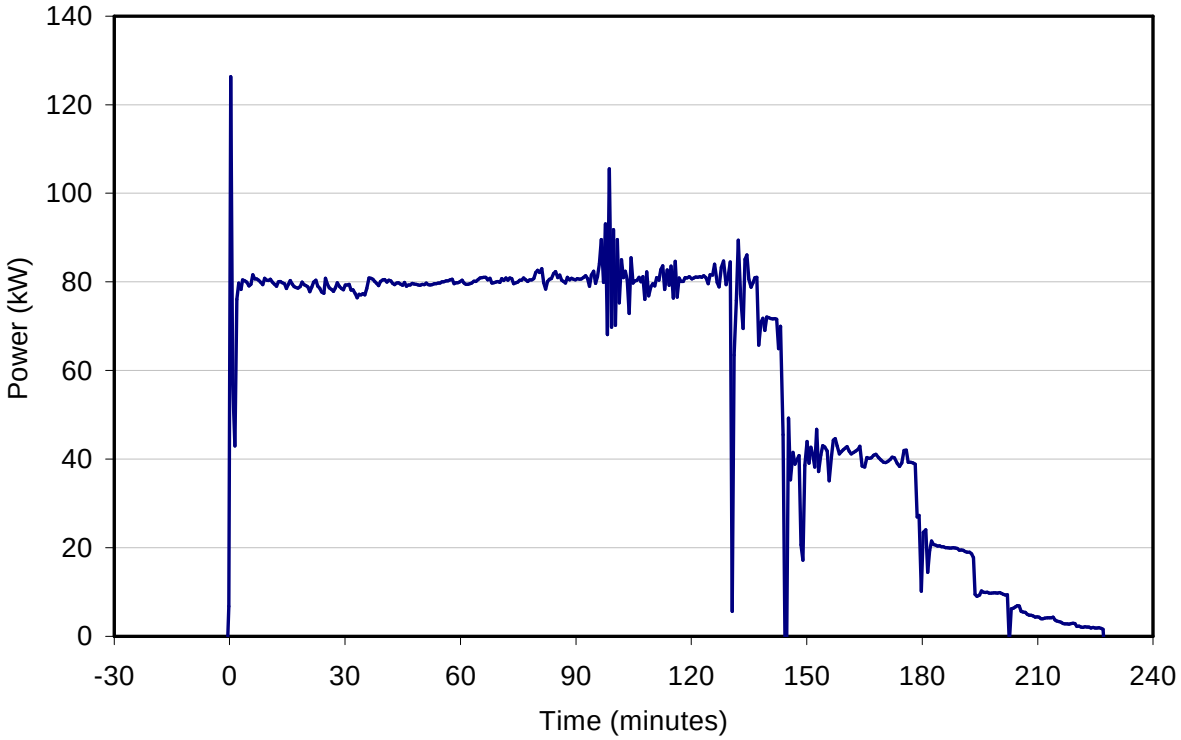

Figure 2-29. DEH Input Power for WCB-1.

As in previous tests, there was a calm period following melt formation in which the concrete surface was protected by an insulating crust. Over the time interval from 30.7 to 52.6 minutes, onset of ablation was detected at the basemat centerline and in all four quadrants. However, ablation continued to proceed slowly until ~ 90 minutes. Over the time interval from 86.6 to 99.5 minutes, the basemat ablation depth reached 2.5 cm at the basemat centerline and in all four quadrants. Past 90 minutes, the ablation rate picked up dramatically, with the ablation depth reaching 12.5 cm at the centerline and in the southwest quadrant over the time interval from 103.3 to 105.5 minutes. On this basis, preparations for flooding the cavity were initiated, and cavity flooding began at 106.1 minutes. Intermittent sparks were observed emanating from the melt surface until 107 minutes. The surface then went dark and remained that way for the balance of the experiment. The initial debris cooling rate peaked at 3.3 MW/m^2, and then steadily declined to 500 kW/m^2 by 120 minutes. Makeup water was periodically added throughout the balance of the test to maintain the water level over the melt roughly in the range 50 ± 5 cm.

By 130 minutes, the melt temperature measurements were scattered, but had stabilized in the range of 1700 to 1900 °C. The temperature of the upper surface of the water-cooled basemat plate had stabilized in the range of 100 to 250 °C at four out of the five measurement locations. The debris/water heat flux had fallen to 370 kW/m^2, while the DEH input power was equivalent to 320 kW/m^2 (i.e., 80 kW DEH input power divided by the test section planar area of 0.25 m^2). Conversely, heat fluxes to the plate were quite low relative to the design basis value of 150 kW/m^2 (see Appendix A); i.e., 10 to 20 kW/m^2. Thus, the up-down power split was biased heavily upwards.

At 134.8 minutes, the basemat ablation depth reached 12.5 cm in the northeast (E-array) quadrant. Subsequently, from 136.2 to 140.1 minutes, the plate surface temperature at this location rapidly increased from 143 °C to 813 °C, yielding a local heating rate of ~ 180 °C/minute. On this basis, the DEH input power was reduced to 70 kW at 137.1 minutes, and the power supply operating mode was switched from constant power to constant voltage. Backup water flows to channels C3, C4, and C5 were started; this increased the channel flowrate from ~ 10 to 12 lpm on the east side of the plate where the high temperature was observed. At 145.2 minutes, the plate surface temperature in the northeast quadrant continued to hover near 800 °C, and on this basis, the input power was reduced to 40 kW. Constant voltage operating mode was then resumed at the lower power level. By 152 minutes, the plate surface temperature in the northeast quadrant had fallen below 600 °C, and continued to decline thereafter.

Over the time interval from 145 to 165 minutes, melt temperatures were still scattered in the range of 1600 to 1950 °C. After the power reduction, the debris-water heat flux declined and then stabilized at 150 kW/m^2. The plate temperature in the northeast quadrant continued to decline, while the temperature near the centerline approached 500 °C. All other plate temperature measurements were $\leq$ 400 °C. Plate heat fluxes ranged from 10 to 40 kW/m^2, with an average value near 20 kW/m^2. The power split remained biased heavily upwards.

At 169.5 minutes, the ablation depth reached 12.5 cm in the northwest quadrant (B array location). From 168.2 to 181.5 minutes, the plate surface temperature in this quadrant steadily increased from 223 °C to 743 °C, yielding an average heating rate of ~ 40 °C/minute. At 178.4 minutes, the input power was reduced to 20 kW, and constant voltage operation was again resumed at the reduced power level. From 178.4 to 194.6 minutes, the melt temperatures remained scattered in the range of 1700 to 1900 °C. The plate surface temperature in the northwest quadrant stabilized in the range of 750 to 780 °C before starting to decline. The debris-water heat flux declined steadily to ~ 120 kW/m^2 and also stabilized. Local plate heat fluxes were in the range of 10 – 25 kW/m^2 at this time. The power split remained biased heavily upwards.

At 194.6 minutes, the input power was reduced to 10 kW, and constant voltage operation was resumed. From 194.6 to 227.0 minutes, melt temperatures steadily declined to within the range of 1500 – 1600 °C. The debris cooling rate also fell from 120 to 75 kW/m^2. Input power at constant voltage declined to < 2 kW. Local plate heat fluxes remained in the range of 10 – 25 kW/m^2. The power split was still biased heavily upwards. At 227 minutes, DEH input to the melt was terminated. Data logging continued until 230.3 minutes. At this point, the system was shutdown following normal termination procedures. The DAS was restarted to record the long-term cool down data. The experiment was left unattended to cool down overnight.

2.3 Test Results

2.3.1 Melt Temperatures

As described in Section 2.2.11, a total of sixteen Type C thermocouple junctions were used to measure melt temperatures at various locations, in addition to a two-color optical pyrometer mounted in the lid of the apparatus that provided data on the melt upper surface

temperature. Data from these instruments are shown in Figure 2-30. This collection of information indicates that in the time interval from melt formation up to the point at which rapid concrete ablation commenced at ~ 90 minutes, melt temperatures were scattered in the range of 1750 to 2000 ˚C. During this interval, melt sparging was minimal due to limited ablation, and so there was no convection within the melt to smooth out temperature variations that developed as a result of the input power to this refractory (i.e., low thermal conductivity) material. However, following onset of significant basemat ablation at ~ 90 minutes, the melt temperature measurements banded more closely together. The bulk temperature declined from ~ 2000 ˚C at 90 minutes to ~ 1800 ˚C at the time of cavity flooding at 106.1 minutes. In the five minute interval following flooding, the temperature declined an additional 100 ˚C before stabilizing at ~ 1700 ˚C. At this point, a stable crust probably formed at the melt upper surface, terminating the bulk cooling transient.

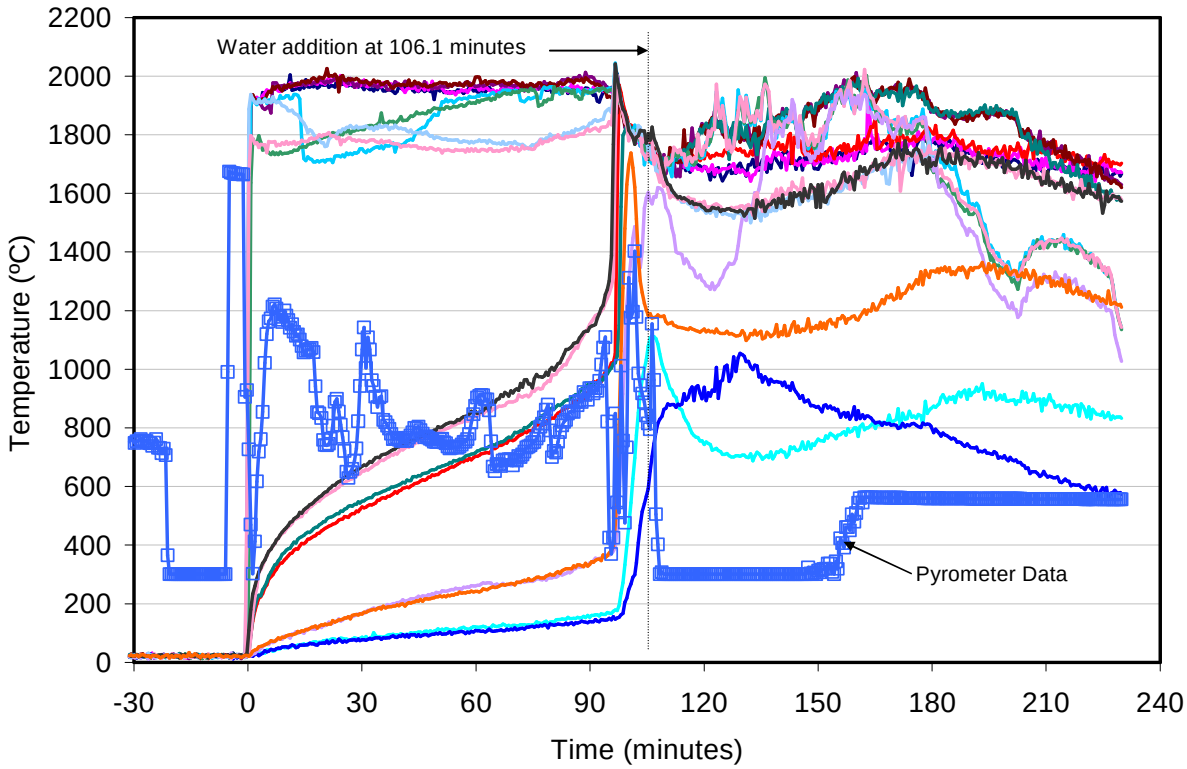

Figure 2-30. Data from all Melt Temperature Measurement Devices.

After the initial transient, effectively all of the concrete had been consumed over the water-cooled basemat plate. Thus, pool gas sparging would have ceased at this time. Past this point (~ 110 minutes), melt temperature measurements again diverged due to the lack of convection within the melt. The temperatures banded in the range of 1600 to 2000 ˚C until the power was reduced to 20 kW at 178.4 minutes. After this time, all remaining functional junctions indicated a steady melt temperature decline until test termination at 230 minutes.

As discussed in Section 2.2.2, views of the debris surface during the dry phase of the test generally indicated the sustained presence of a crust over the melt. The optical pyrometer data shown in Figure 2-30 supports this observation. Peaks in the readings from this instrument generally correspond to time intervals in which aerosols in the test section plenum cleared to

provide a view of the crust upper surface. The measurements during these intervals indicate crust surface temperatures that declined from ~ 1200 ˚C early in the interaction to ~ 900 ˚C just before onset of significant ablation at ~ 90 minutes. Past this time and up to the point of cavity flooding at 106.1 minutes, the surface temperature measurements escalated sharply up to ~ 1400 ˚C. After cavity flooding at 106.1 minutes, the pyrometer data are no longer reliable as the corium surface would have been quenched to the water saturation point of ~ 100 ˚C.

2.3.2 Basemat Ablation

The basemat was instrumented with five multi-junction Type K thermocouple arrays to monitor the axial progression of the ablation front, as well as the thermal response of the water-cooled basemat plate (Figure 2-22). The sequential rise in signals obtained from the A-array located near the basemat centerline is shown in Figure 2-31; the responses at the other four array locations were similar [10]. Figure 2-32 provides the axial ablation depth versus time that was deduced from the data provided by the five arrays. In general, the data from all units indicated a gradual heatup and ablation of the concrete basemat over the first ~ 90 minutes of the test. Thereafter, a rapid transient occurred in which the remaining ~ 10 cm of the concrete was consumed by erosion over a time interval of ~ 15 minutes. However, it is noteworthy that at all thermocouple locations, the progression of the ablation front was terminated as the water-cooled plate was approached. This observation was confirmed during posttest examinations, which indicated that the plate survived the experiment intact.

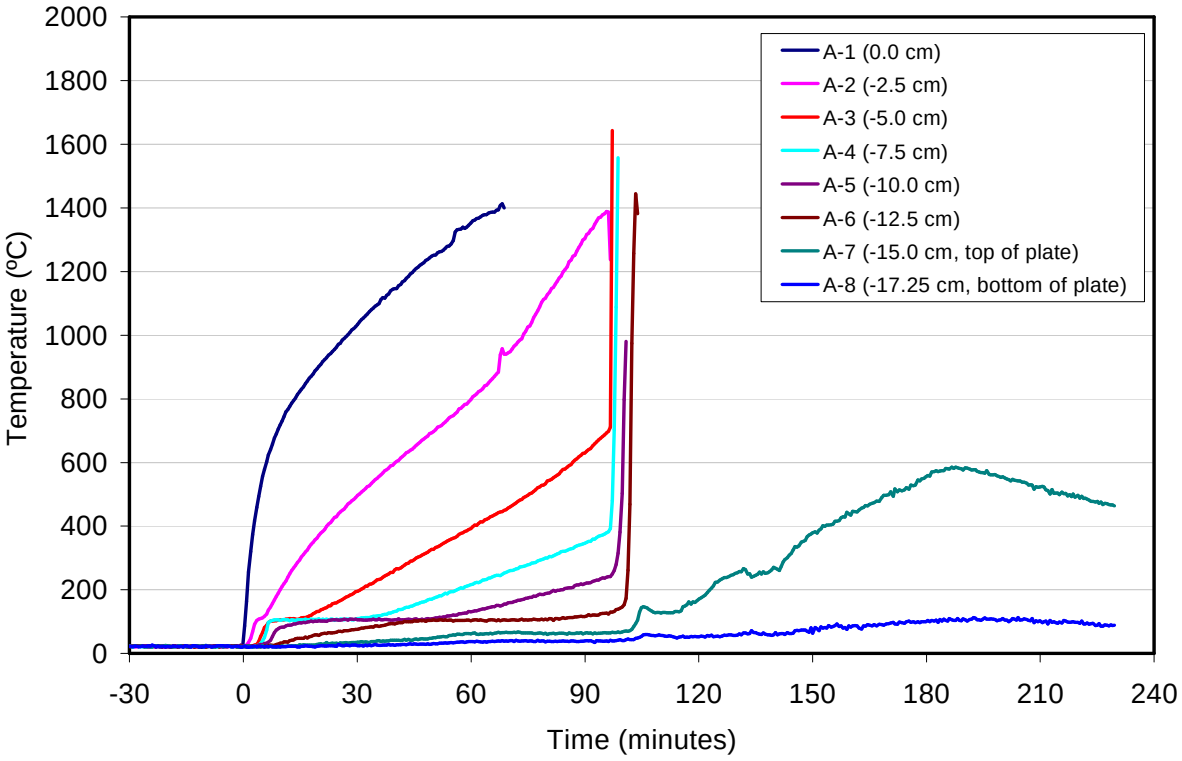

Figure 2-31. Basemat Thermal Response at the Centerline ("A" Array).

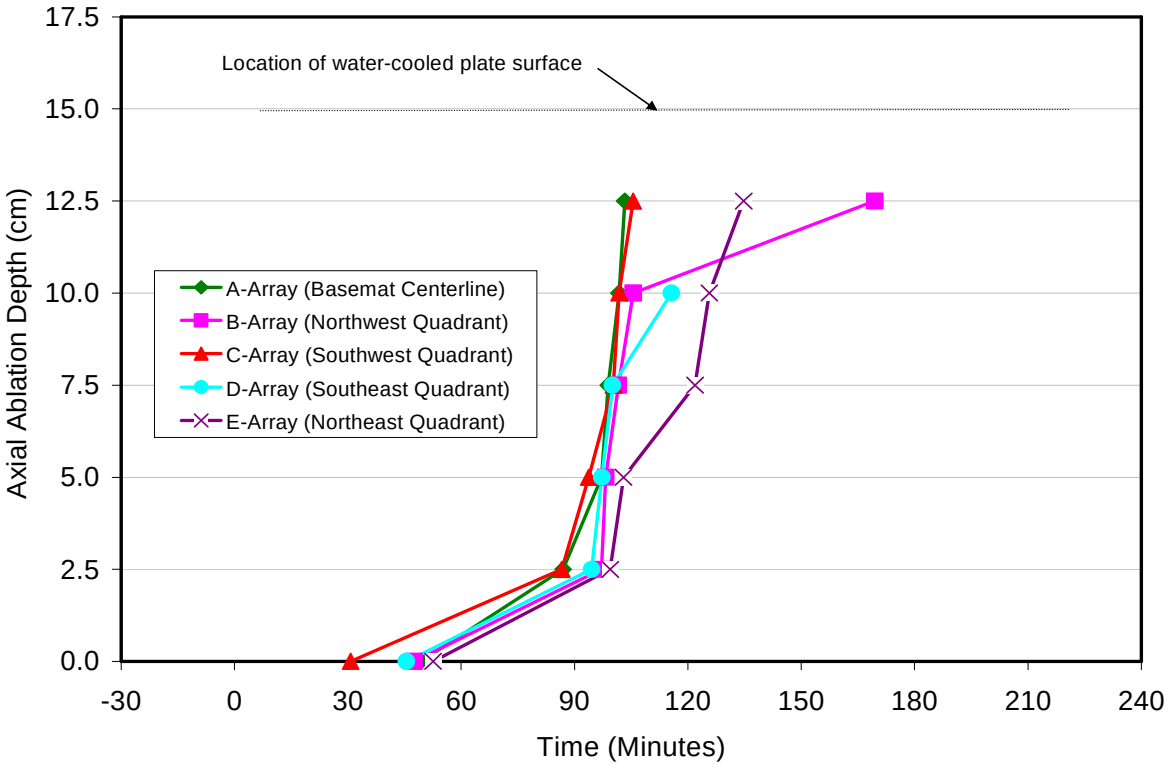

Figure 2-32. Basemat Axial Ablation Front Location.

2.3.3 Water-Cooled Plate Thermal Response

Evaluating both the local and global thermal performance of the basemat water-cooled plate was a key design objective for WCB-1. To that end, the plate was instrumented to measure local temperatures and heat fluxes, as well as water flowrate and coolant inlet and outlet temperatures. The design-basis heat flux to the plate was 150 kW/m^2, which roughly corresponds to a 50-50 up-down power split at the initial DEH input power level of 80 kW in the 50 cm x 50 cm test section. Based on design calculations [9], after the system equilibrated at the design heat flux, the water temperature rise across the water-cooled channels was expected to be ~ 9 ºC, with the boundary condition on the plate inner surface being highly subcooled nucleate boiling. The top surface of the plate was expected to come to equilibrium at ~ 373 ºC, with the plate protected by a ~ 1 cm deep corium (or concrete slag) crust.

In reality, the data indicates that the up-down power split after the concrete basemat was fully eroded was highly biased to the overlying water layer. The heat fluxes to the plate measured by the nine flux meters that were incorporated into the basemat are shown collectively in Figure 2-33. With the exception of one reading from meter C4M, located in the midpoint of the east-central channel (see Section 2.2.11), all measurements were exceedingly low, in the range of 10 to 25 kW/m^2, which is almost an order of magnitude below the design basis value of 150 kW/m^2. The one reading by C4M of slightly over 40 kW/m^2 at 146 minutes corresponded to the time at which the plate surface temperature peaked at slightly over 800 ºC in the northeast quadrant of the basemat; see Table 2-6. Surface temperatures measured on the upper and lower plate surfaces are shown in Figures 2-34 and 2-35, respectively.

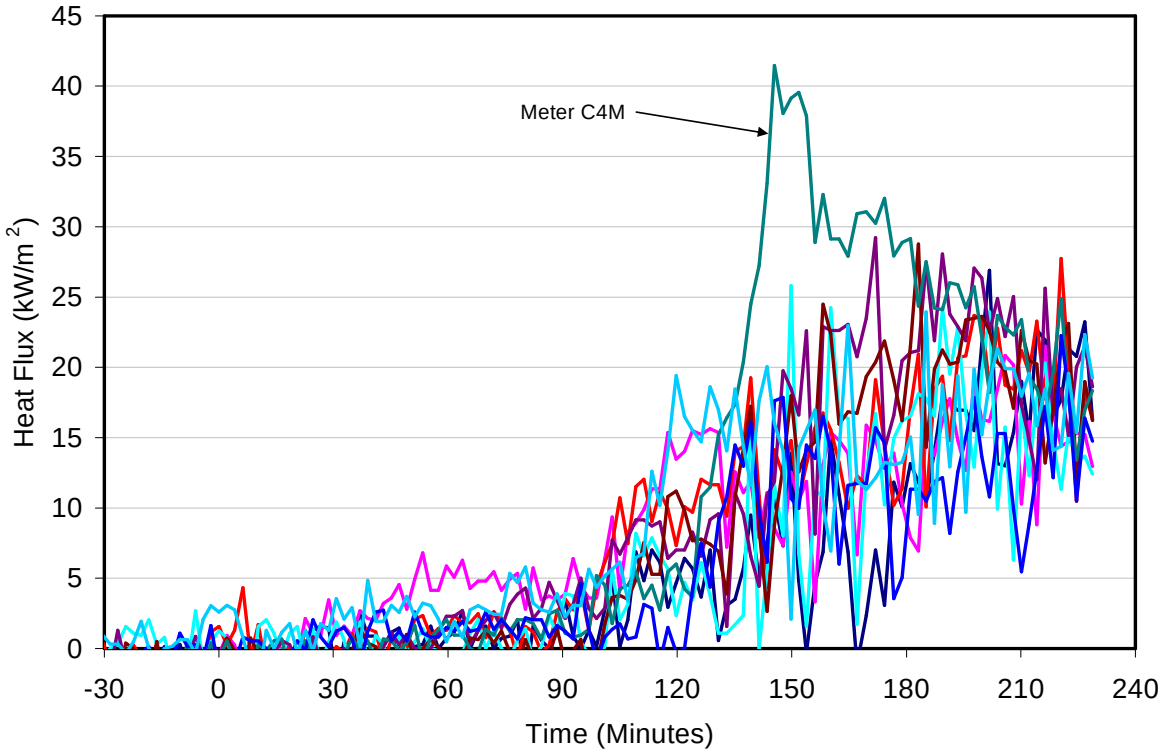

Figure 2-33. Data from All Water-Cooled Basemat Heat Flux Meters.

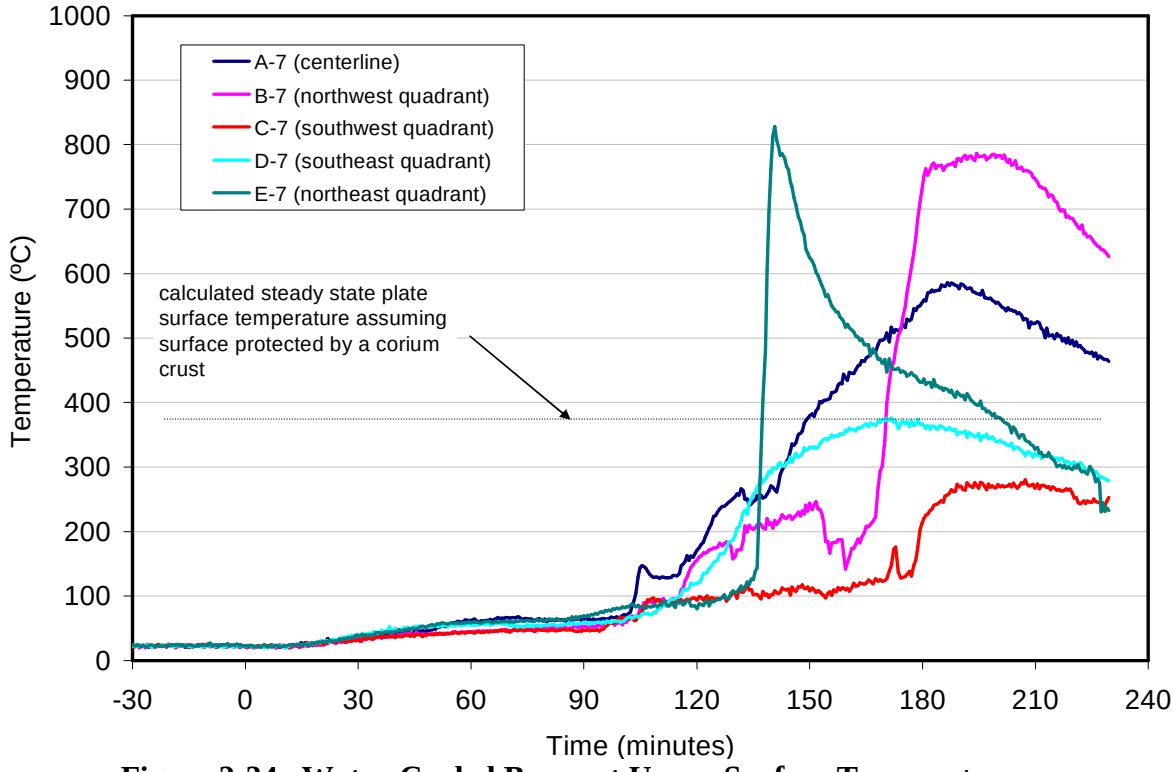

Figure 2-34. Water-Cooled Basemat Upper Surface Temperatures.

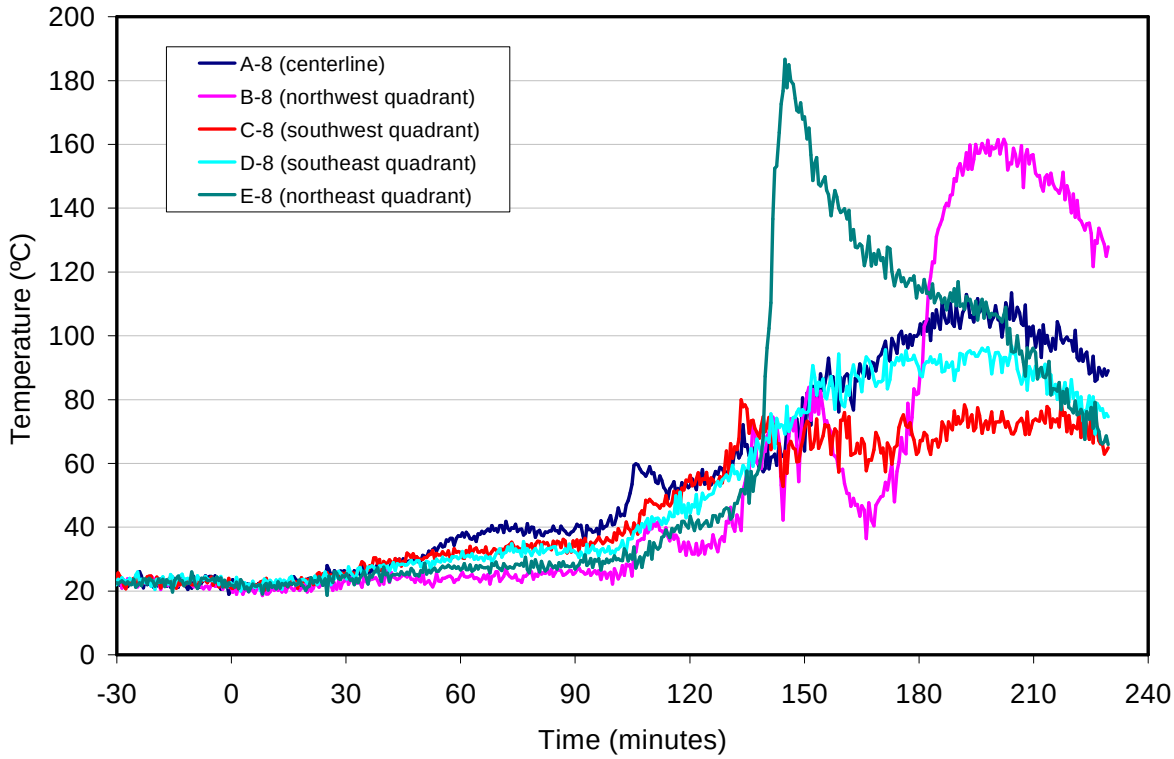

Figure 2-35. Water-Cooled Basemat Lower Surface Temperatures.

Measurements in the water channels also indicated that the plate heat fluxes were quite low. Flowrates to each of the five cooling channels are shown collectively in Figure 2-36, while water inlet and outlet temperatures, as well as temperatures measured 2 cm below the steel upper surface, are shown for the center coolant channel in Figure 2-37. The thermal responses for the other four coolant channels are similar to that measured for the center channel [10]. As shown in in Figure 2-36, at 137 minutes backup water flow was initiated in channels C3, C4, and C5; this was due to the high plate surface temperature observed in the northeast quadrant (see Figure 2-34). This action increased the flowrate to these channels from ~ 10 to ~ 12 lpm.

As previously noted, the expected coolant temperature rise across the channels at design conditions (i.e. 150 kW/m^2) was 9 ºC. As is evident from Figures 2-37, the actual temperature rises were much lower; i.e., 1-2 ºC. This degree of temperature rise is consistent with the heat fluxes shown in Figure 4-16. The steel temperatures measured 2 cm below the plate surface inside the cooling channels also remained relatively cool (< 100 ºC). This can be contrasted with several of the temperatures measured on the plate upper surface (see Figure 2-34). However, it should be noted that these high readings were recorded in the region of the plate that included the steel ribbing that divided each coolant channel (see Figures 2-4 and 2-22). The temperature at these locations should have been higher in comparison to those in the channel itself. However, the extent of this increase has not been estimated as part of this study since this would require a fairly detailed three-dimensional heat transfer analysis in a complicated geometrical configuration.

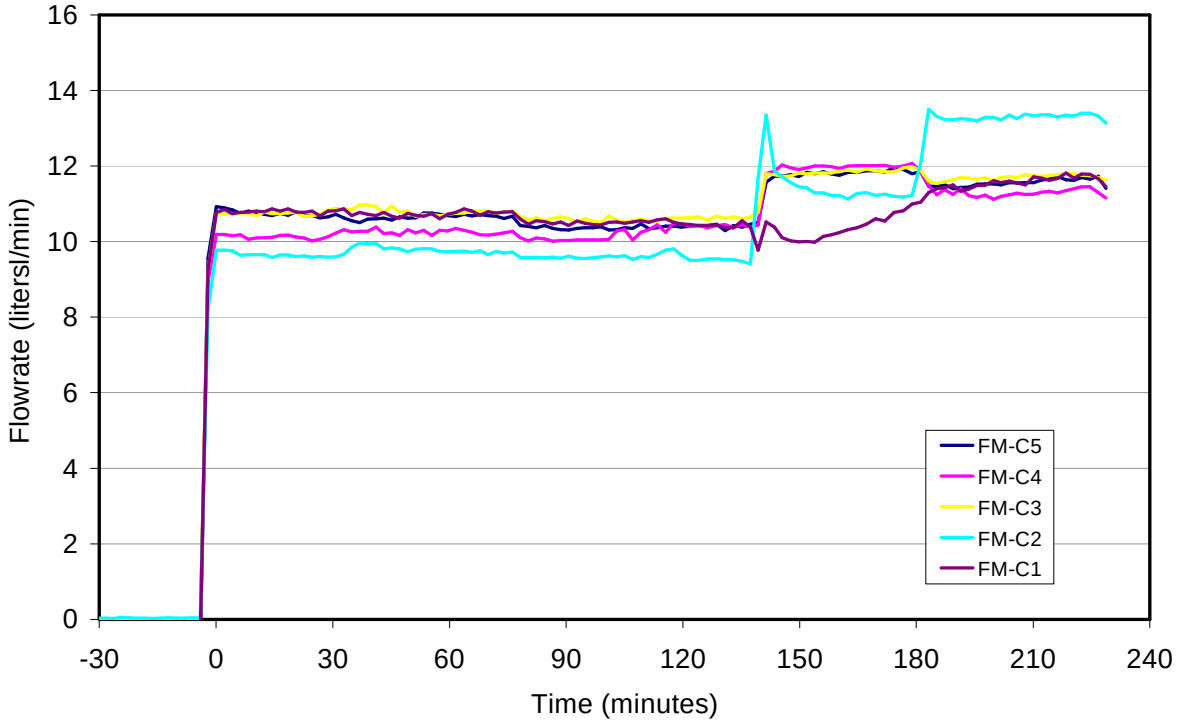

Figure 2-36. Basemat Cooling Channel Water Flowrates.

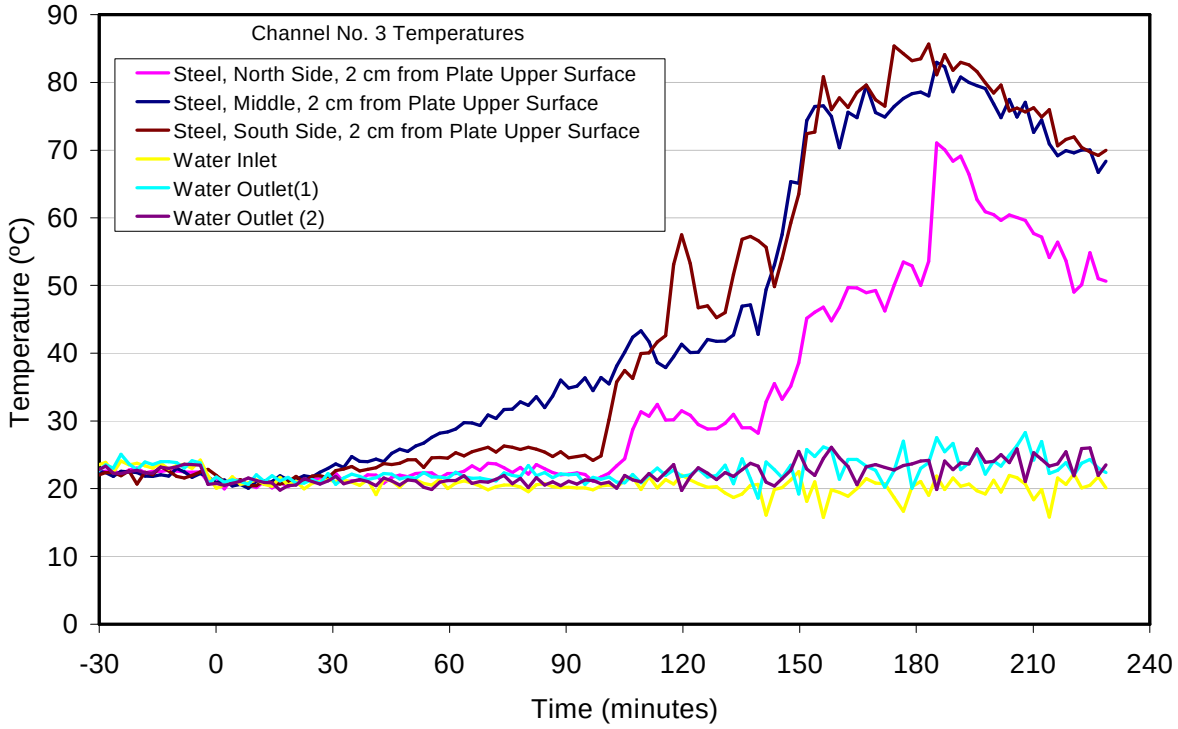

Figure 2-37. Channel No. 3 (central) Coolant Inlet/Outlet and Steel Temperatures 2 cm from Plate Surface.

2.3.4 Corium Top-Flooding Quench Rate

As dictated by the test procedure, after the basemat ablation depth reached the pre-defined level of 12.5 cm, the cavity was flooded to obtain data on the nature and extent of the corium cooling when flooding occurs over a water-cooled basemat plate. The debris-water heat flux was evaluated on the basis of the steaming rate from the interaction using the test section planar area of 0.25 m^2 [10]; the results are shown in Figure 2-38 and 2-39. These figures also include the DEH input power normalized with test section area for comparison with the debris cooling rate. The rate varied from 3.3 MW/m^2 immediately after cavity flooding, down to ~ 100 kW/m^2 at the time the test was terminated. For most of the test, the heat flux to overlying water met or exceeded the DEH input power. This indicates that the up-down power split was biased heavily upwards. Note that the same conclusion was drawn based on the plate thermal response results described in the previous section.

As described in Section 2.2.2, the test operating procedure was not only designed to evaluate the performance of the basemat water-cooled plate, but also to determine the dryout limit of the melt. The intended procedure was to systematically reduce (i.e. step down) the input power, followed by a 15 minute period of constant voltage operation at the new level obtained following the power reduction. If water ingression was initiated at the new voltage level, then the input power should decrease as the melt quenched (by reduction in conductor area, which is the same as increasing load resistance), and this would be the indicator that the corium dryout limit had been reached. Unfortunately, the power reductions in WCB-1 were not as structured as planned in the original test procedure due to the development of hot spots on the plate. Nonetheless, a first order comparison can still be made.

The first step is to estimate the dryout limit for the WCB-1 corium from the SSWICS correlation [3] for comparison with the heat flux data from the experiment. The correlation is shown graphically in Figure 2-40. As shown in Table 2-1, the 400 kg corium charge for WCB-1 contained 8 wt % siliceous concrete as an initial constituent. The 15 cm thick basemat weighed 85.1 kg, which resulted in the addition of 73.4 kg of slag to the melt after dryout of the water vapor and CO_2 from the concrete (see Table 2-2). Thus, at the end of the test the melt contained ~ 23 wt % siliceous concrete. From Figure 2-40, the dryout limit for the melt was ~ 53 kW/m^2 based on the SSWICS correlation at that time. This heat flux is shown in Figure 2-39 for comparison with the debris-water heat flux, along with the normalized DEH input power. For this relatively low dryout limit, water ingression would not have been initiated until late in the experiment sequence when the input power was substantially reduced. At 145.2 minutes, input power was reduced to ~ 40 kW (equivalent to a flux of ~ 160 kW/m^2). As is evident from Figure 2-40, the power stayed fairly constant past this time indicating that ingression was not occurring. Power was reduced to 20 kW at 178.4 minutes (equivalent to a flux of ~ 80 kW/m^2) and after this time, the input power does seem to indicate a negative slope. The power was reduced again to ~ 10 kW (40 kWm^2 equivalent flux) at 194.6 minutes, and the input power curve continues to show a similar negative slope. During these last two power reductions, the debris-water heat flux drifted down to ~ 120 kW/m^2 at 190 minutes, and remained at this level over the last 30 minutes of the experiment. Thus this collection of data suggests a dryout limit of ~ 100 kW/m^2 for the end-of-test core melt composition. This is slightly higher than the 53 kW/m^2 predicted from the SSWICS correlation, but of the same order of magnitude.

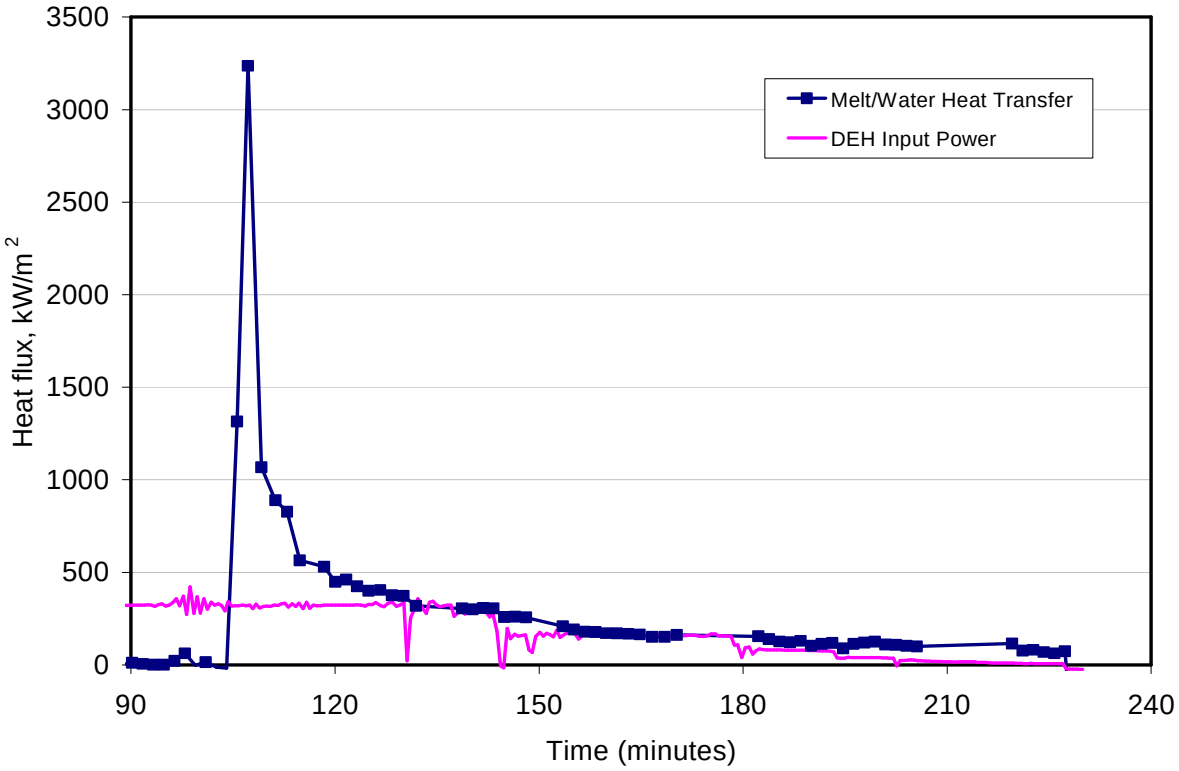

Figure 2-38. Heat Flux to Overlying Water Pool.

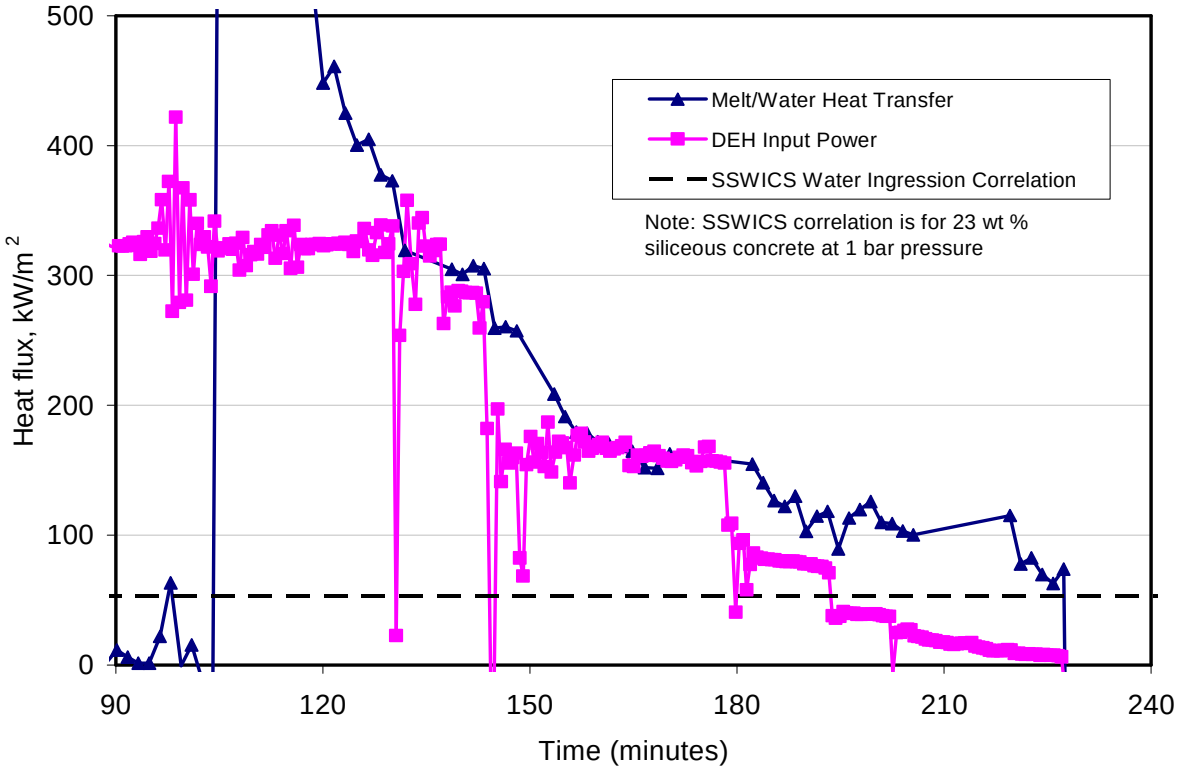

Figure 2-39. Heat Flux to Overlying Water Pool: Expanded Scale.

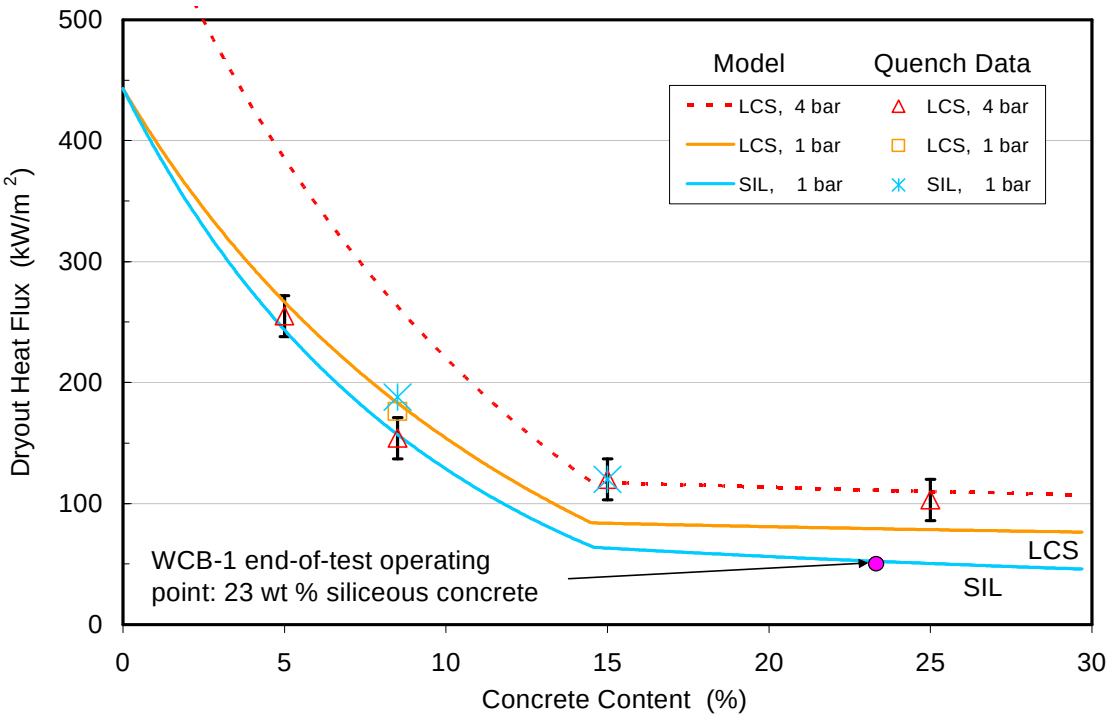

Figure 2-40. SSWICS Dryout Heat Flux Test Data and Correlation [3].

2.3.5 Posttest Examinations

Following the experiment, the apparatus was carefully disassembled to document the posttest debris configuration. Figure 2-41 provides a picture of the top surface of the debris after removal of the top sidewall section. Elevation measurements at this point indicated that the upper surface of the debris was near the initial collapsed pool height of + 25 cm relative to the initial concrete surface elevation.

As the debris was removed, physical characteristics and dimensions were recorded so that accurate renderings of the posttest debris configuration could be produced; the results are provided in Figures 2-42 and 2-43. Since the key objective of this experiment was to examine the performance of the water-cooled plate, the corium was completely removed from the test section to reveal the plate so that it could be physically examined and photographed.

During the latter phase of the experiment, gas sparging from concrete decomposition was absent, and so an anchored crust configuration with an intervening void between the melt pool should not have formed in this test. The posttest examinations confirmed that this was indeed the case. The overall debris configuration consisted of an upper, 10-15 cm thick porous layer that probably formed during the initial phase of the quenching process when gas sparging was still present (i.e., as the remaining ~ 2 cm thick layer of concrete was eroded from the plate upper surface). Beneath the porous layer was a 25 to 30 cm thick monolithic layer of solidified corium with minimal porosity. This layer of material was most likely the balance of the melt pool that was not initially quenched, and thus underwent the longer-term interaction with the water-cooled plate.

Figure 2-41. Top View of Debris after Removal of Top Sidewall Section.

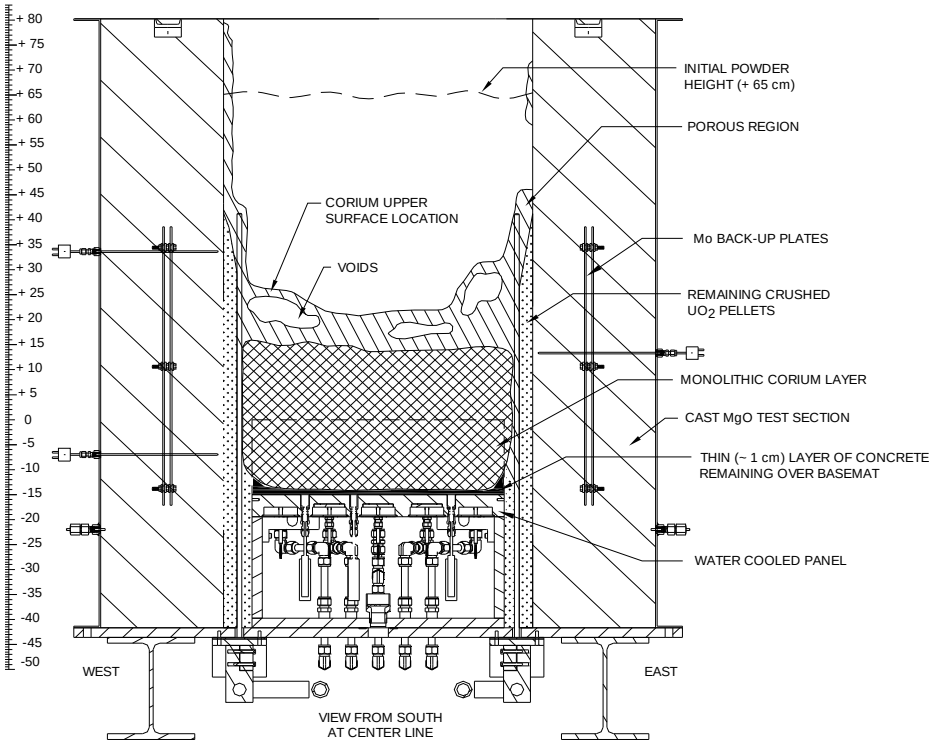

Figure 2-42. Rendering of Posttest Debris as Viewed from the South.

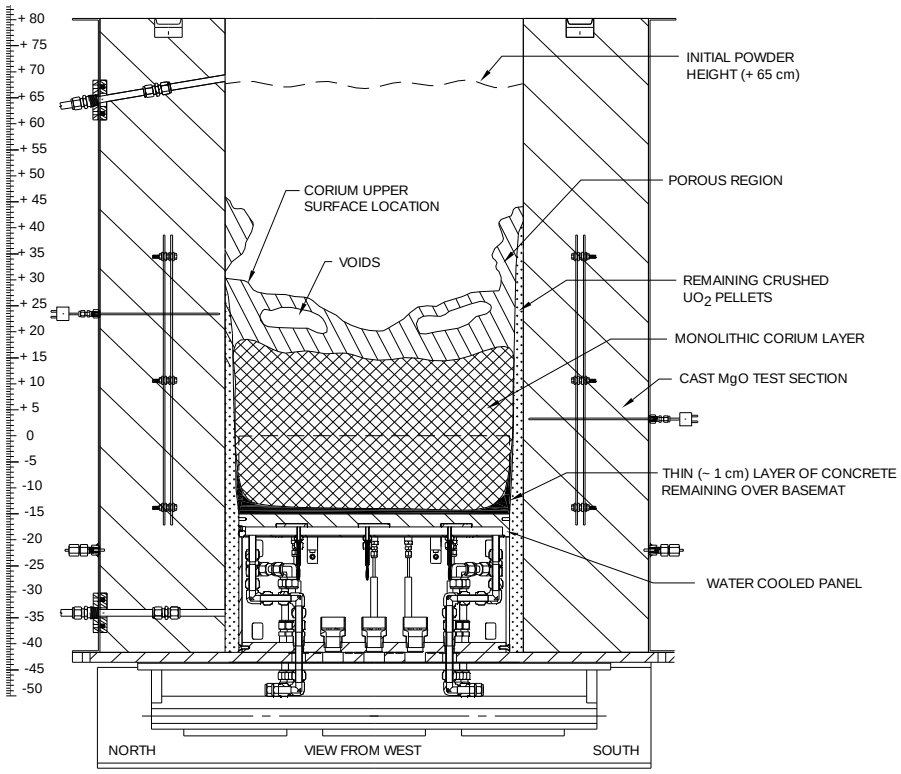

Figure 2-43. Rendering of Posttest Debris as Viewed from the West.

Finally, beneath the solid corium layer was a thin (~ 1 cm) layer of concrete that completely covered the plate upper surface. This layer of material was not ablated during the test, confirming that the water cooling was successful in halting the progression of the ablation front. Photographs showing the upper surface of the water-cooled plate are provided in Figure 2-44. Examination of the plate provided no evidence that the plate had melted. A few darkened areas are evident in the photographs that would not wash off. These may be locations where the plate heated up and locally corroded.

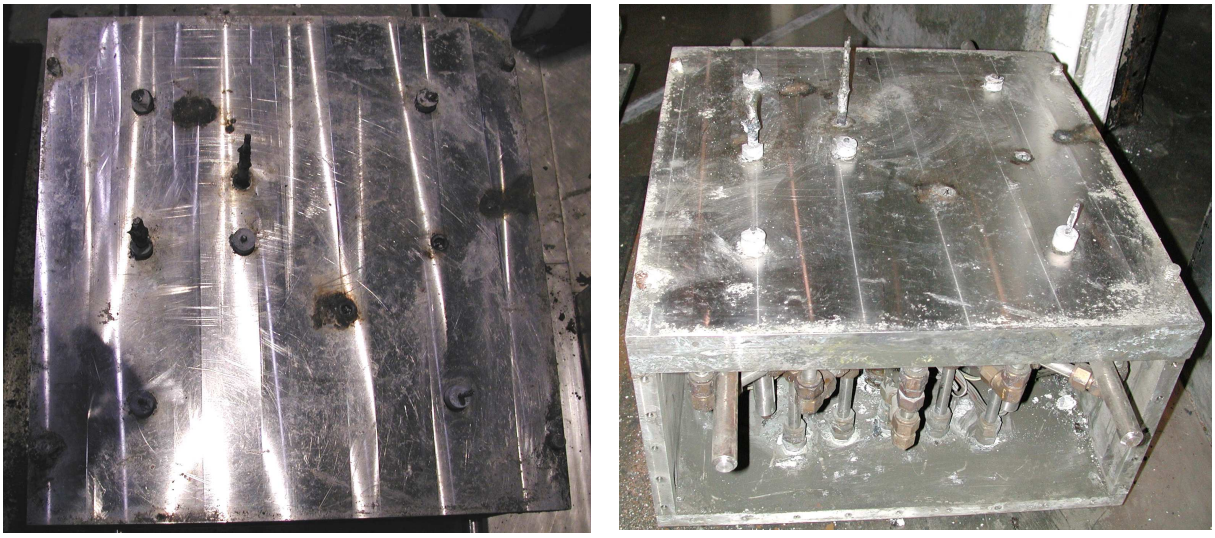

(a) **(b)**

Figure 2-44. (a) Face-On and (b) Side Views of Water-Cooled Plate (views from south).

2.4 Discussion

The high-level experiment objective of WCB-1 was to provide reactor material test data on the transient evolution and stabilization of a core melt within a generic water-cooled core catcher design for advanced plant applications. In this regard, the experiment was felt to be operationally successful. A core melt at 1950 °C was produced over a water-cooled basemat that was originally protected by a 15 cm thick layer of siliceous concrete. As in previous core-concrete interaction tests, there was a quiescent period following melt generation in which the concrete surface was most likely protected by an insulating corium crust that formed on initial melt contact with the cold concrete surface. However, continued heating of the corium eventually led to heatup of the concrete beneath and the crust eventually remelted or failed, leading to onset of rapid basemat ablation. The test data indicated that this transition point occurred at ~ 90 minutes following initial melt contact with the concrete surface. During the quiescent period, melt temperatures were scattered in the range of 1750 to 2000 ˚C. The melt sparging would have been reduced during this phase due to limited ablation ($\leq$ 2.5 cm) and so there was no convection within the melt to smooth out temperature variations that developed as a result of the input power to this refractory (i.e., low thermal conductivity) material.

After onset of ablation at ~ 90 minutes, a rapid transient occurred in which the remaining ~ 10 cm of the concrete was consumed by erosion over a time interval of ~ 15 minutes, resulting in an average 'ablation' rate of ~ 6.7 mm/minute. This rapid concrete erosion rate can partially be rationalized by considering the preceding 90 minutes of the interaction, wherein the concrete beneath the corium crust would have undergone significant heatup and dryout (see Figure 2-31). Thus, when erosion finally commenced, the effective concrete decomposition enthalpy was significantly reduced, thereby allowing for an accelerated rate of ablation for a given heat flux to the concrete surface. However, it is noteworthy that at all basemat thermocouple locations, the progression of the ablation front was terminated as the water-cooled plate was approached. This observation was confirmed during posttest examinations, which verified that the plate survived the experiment intact. During this phase, the melt temperature measurements banded more closely together due to convection from gas sparging in the melt pool. The bulk temperature declined from ~ 2000 ˚C at 90 minutes to ~ 1800 ˚C at the time of cavity flooding. Up until this time, the water-cooled basemat plate remained relatively cool due to the insulating properties of the overlying concrete.

At 105 minutes, the ablation depth had reached the 12.5 cm depth at several locations within the basemat, and on this basis, the cavity was flooded according to the normal test procedure. In the five minute interval following flooding, the melt temperature declined an additional 100 ˚C before stabilizing at ~ 1700 ˚C. At this point, a stable crust probably formed at the melt upper surface, terminating the bulk cooling transient. Following the initial transient, effectively all of the concrete had been consumed over the water-cooled basemat plate. Thus, pool gas sparging would have ceased at this time, and melt temperature measurements again diverged due to the lack of melt convection. The temperatures banded in the range of 1600 to 2000 ˚C until the power was reduced to 20 kW at 178.4 minutes. After this time, all remaining functional junctions indicated a steady melt temperature decline until the test was terminated at 230 minutes. In terms of the melt-water heat transfer rate, the heat flux varied from 3.3 MW/m^2

immediately after cavity flooding, down to ~ 100 kW/m^2 at the time the test was terminated. The data indicates that the heat flux to overlying water met or exceeded the DEH input power over the entire test, indicating that the up-down power split was biased heavily upwards.

Aside from the above information, additional data was gathered regarding the plate thermal response during the experiment. The design-basis heat flux to the plate was 150 kW/m^2, which corresponds to a 50-50 up-down power split at the initial DEH input power level of 80 kW in the 50 cm x 50 cm test section. Based on this value, the plate cooling system was expected to evolve such that the temperature rise across the water-cooled channels would approach 9 ºC, with the boundary condition on the plate inner surface being highly subcooled nucleate boiling. The top surface of the plate was expected to come to equilibrium at ~ 373 ºC, with the plate protected by a ~ 1 cm deep corium (or concrete slag) crust. In reality, the plate thermal response data also indicated that the up-down power split after concrete erosion was biased heavily towards the overlying water. In particular, the measured heat fluxes to the plate were exceedingly low, in the range of 10 to 25 kW/m^2, which is almost an order of magnitude below the design basis value of 150 kW/m^2. Measurements on the water side of the channels were also consistent with this finding; i.e., the coolant temperature rise was only 1-2 ºC, which is much lower than the 9 ºC based on the design basis heat flux.

The collection of data from this experiment thus indicates that for a configuration in which a corium melt pool is covered by overlying water with an underlying water-cooled plate, the power split will be biased heavily towards the overlying water. From a different point of view, these findings are also consistent with the previous SSWICS test results [3] that indicate that cracks and fissures that form in the debris during quench result in cooling rates that exceed the conduction limitation. Results from the current Category 1 test program [28] indicate that when this quench process occurs in the presence of sparging gas, the cooling rate is increased even further. Heat transfer to the underlying impervious water-cooled plate would have been limited by conduction across a crust to a heat sink temperature that at most would have approached the water saturation temperature. The heat sink temperature established by the overlying water pool would have also corresponded to the water saturation temperature. Thus, given that the heat sink temperatures on the top and bottom of the melt were effectively identical, the data from this test supports the concept that corium quenched by overlying water forms a morphology in which the heat flux to the coolant does indeed exceed the conduction limitation.

Aside from these positive overall findings, several hot spots were noted to form on the coolant plate steel surface during the course of the experiment that significantly exceeded the peak temperature expected on the basis of the engineering design calculations (i.e,. 373 ºC). These hot spots seemed to form rapidly, and this resulted in the operators reducing the input power from the initial target value. However, it should be noted that these high temperature measurements were taken in the region of the plate that included the steel ribbing that divided each coolant channel. The temperature at these locations should have been higher in comparison to those in the channel itself. However, the extent of this increase was not estimated as part of this study since this would require a fairly detailed three-dimensional heat transfer analysis in a complicated geometrical configuration.

3.0 SSWICS BOTTOM WATER INJECTION TEST RESULTS

The high-level experiment objective of the SSWICS bottom water injection tests was to examine the influence of water injection characteristics on the debris cooling rate when the coolant is introduced into the bottom of the melt from isolated nozzles that are cast in the basemat. As shown in Table 1-2, two experiments were conducted as part of this test series. The first, denoted SSWICS-12, examined the influence of nozzle water pressure on the debris quenching rate. The second test, denoted SSWICS-13, investigated the effect of concurrent noncondensable (i.e., N_2) gas injection on the local debris cooling rate, since the presence of non-condensable gas during melt-water interaction is postulated to suppress the possibility of an energetic fuel-coolant interaction [13]. The facilities for these two experiments were quite similar. Thus, the SSWICS-12 facility is described first, followed by a section that describes hardware changes that were made for SSWICS-13. The results from the two tests are then presented and discussed. Full details regarding the facility designs and test results can be found in dedicated test plans [7,8] and data reports [11,12] that were developed for each test.

3.1 SSWICS-12 Facility Description

3.1.1 Test Apparatus

The SSWICS reaction vessel (RV) was designed to hold at least 100 kg of melt at an initial temperature of 2500^{o}C. The RV lower plenum consists of a 67.3 cm long, 45.7 cm outer diameter carbon steel pipe (Figure 3-1). The pipe was insulated from the melt by a 6.4 cm thick annulus of cast MgO that was denoted the “liner”. The selected pipe and insulation dimensions resulted in a melt diameter of 30 cm and a surface area of 707 cm^2. The melt depth for a typical corium charge of 75 kg was about 15 cm. The RV lower flange was insulated with a 6.4 cm thick slab of cast MgO (the “basemat”) that spanned the entire inner diameter of the pipe. The basemat and liner formed the crucible that held the corium.

The RV upper plenum consisted of a second section of pipe with a stainless steel protective liner. Three 10 cm pipes welded near the top of the vessel provided 1) a vent line for the initial surge of hot noncondensable gases generated by the thermite reaction, 2) a pressure relief line with a rupture disk (7.7 bar at 100^{o}C), and 3) an instrument flange for the absolute pressure transmitter that measured the reaction vessel pressure. A baffle was mounted below the upper flange to prevent water droplets from being carried up towards the condenser, which would have adversely affected the heat flux measurement. A fourth 10 cm pipe welded to the top flange provided an outlet for steam from the quenching melt to four cooling coils. The water-cooled coils condensed the steam, which was collected within a 200 cm high, 20 cm diameter condensate tank (CT). Figure 3-2 provides an overview of the entire SSWICS test facility.

For SSWICS-12, the corium was divided into quadrants by 10 mm thick tungsten plates. The partitions had machined slots so that one fits over the other in an interlocking cruciform. They were supported by 20 mm deep grooves in the liner to limit shifting under lateral loads. The partition consisted of two stacked sections, each with a height of 20 cm, creating a 40 cm high wall within the melt. Figure 3-3 provides a detailed view of the lower plenum and basemat including the tungsten partitions, while Figure 3-4 shows photographs of the test article during assembly.

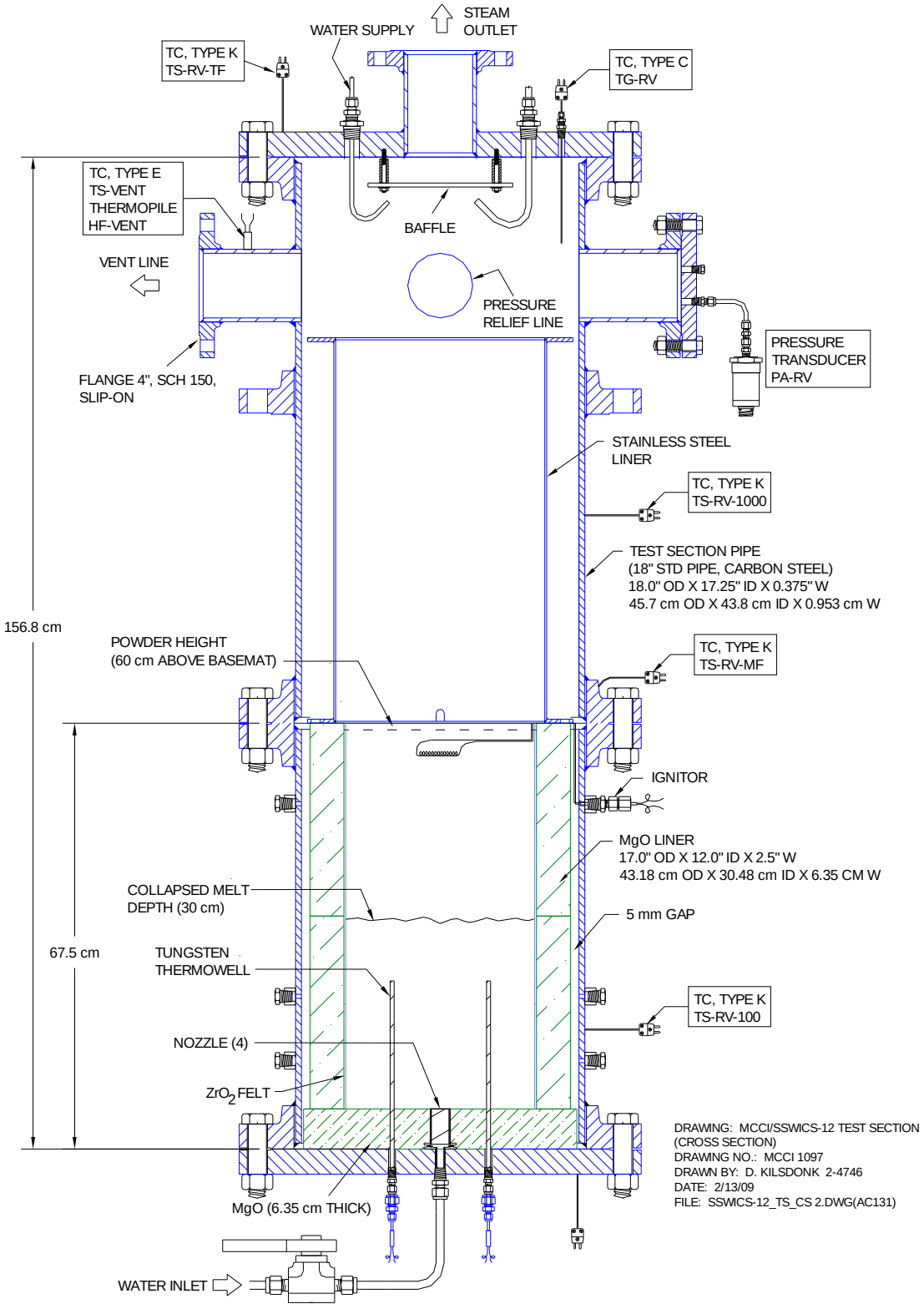

Figure 3-1. Side View of Reaction Vessel.

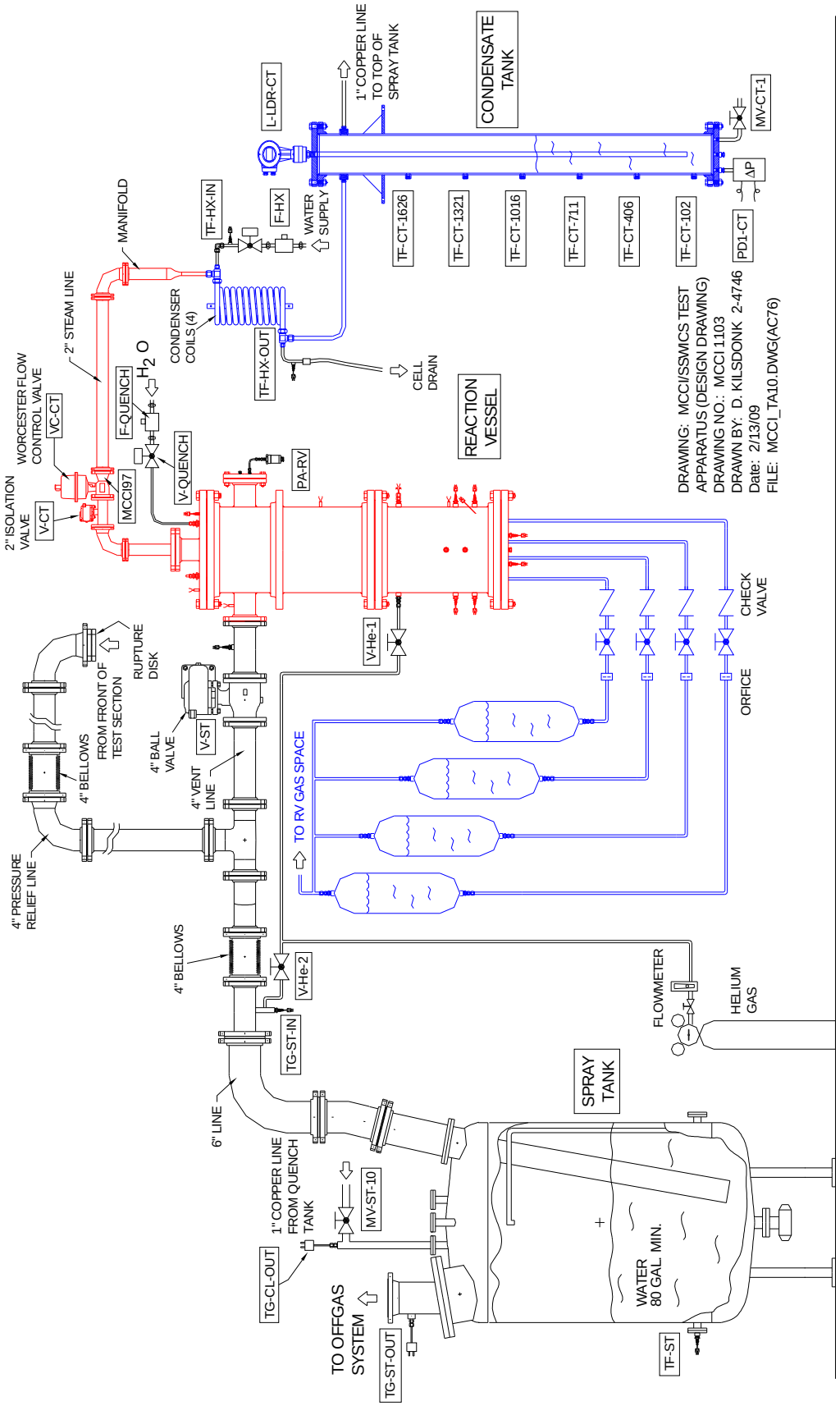

Figure 3-2. SSWICS Melt Quench Facility.

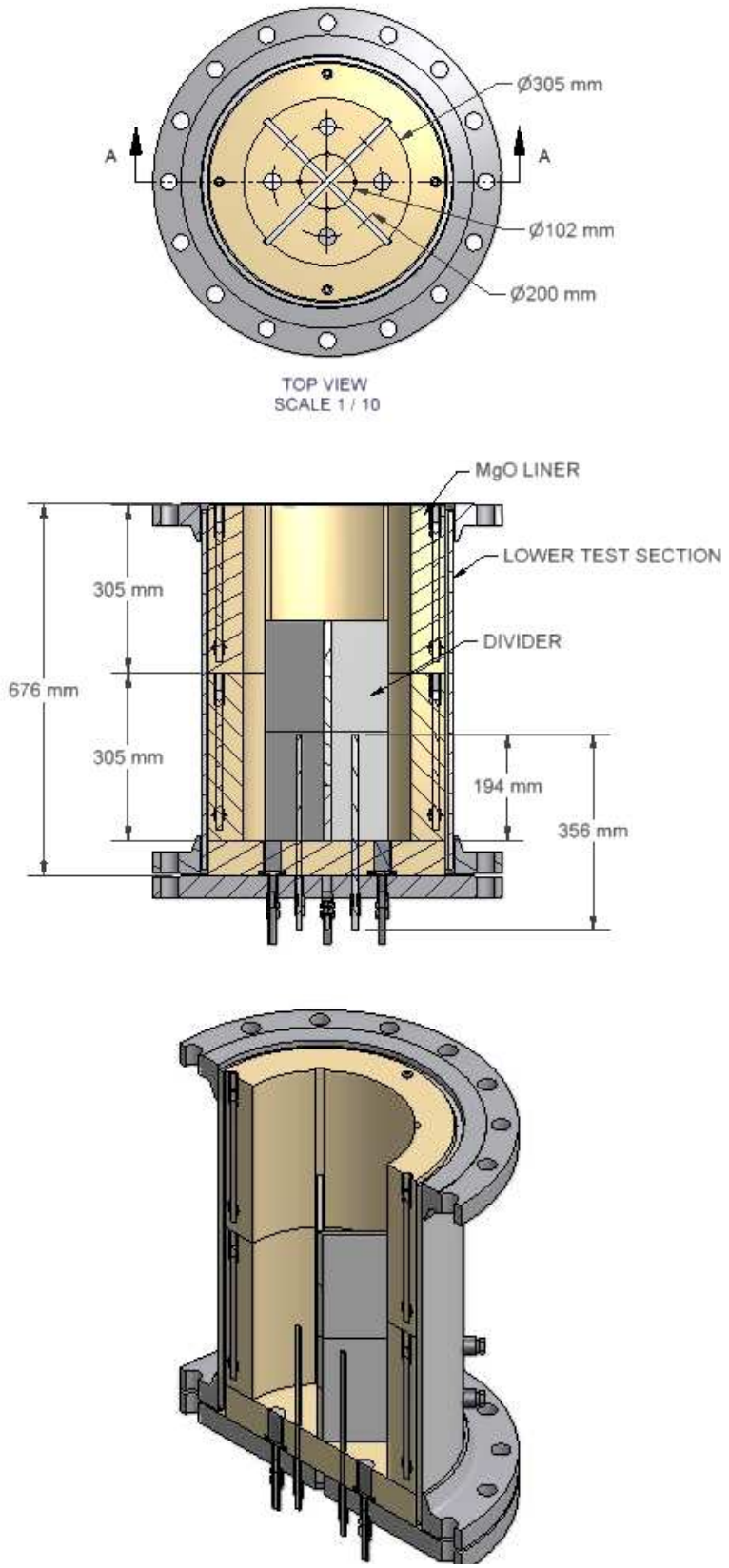

Figure 3-3. SSWICS-12 Lower Plenum and Basemat Details.

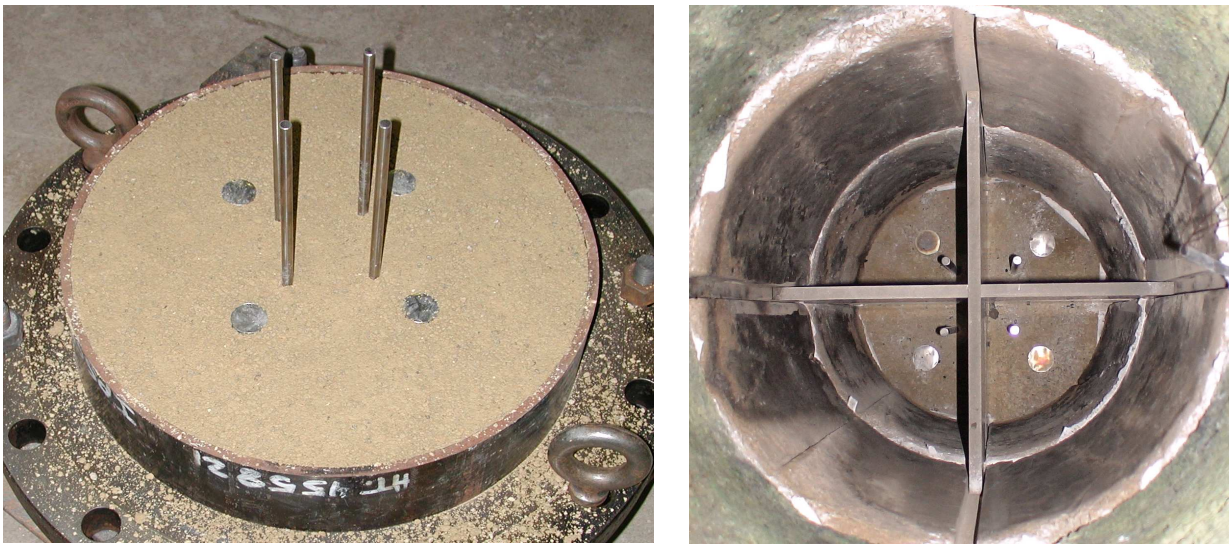

(a) ***(b)***

Figure 3-4. SSWICS-12 Basemat Assembly (left) and Assembled Lower Section Assembly Showing Tungsten Cruciform (right).

3.1.2 Injection Supply System

Four 36-liter tanks provided independent reservoirs to supply the nozzles with water. The nozzles were gravity fed and so the driving pressure for injection was set by the elevation difference between the nozzle and the tank water level (Figure 3-5). A check valve in each line prevented back flow up into the tank and isolation valves were opened when the RV preheat phase of the test began.

For SSWICS-12, the tanks were positioned at different levels to generate the desired range of driving pressures. A pressure equalization line linked the RV gas space to the gas spaces of all four tanks, ensuring that the head was set only by the nozzle - tank elevation difference. This was necessary because the RV pressure routinely spiked for a short period following initial water injection. If the reservoirs were not at the absolute pressure of the RV, then the initial pressure spike would halt water injection, causing steam production and RV pressure to drop, which in turn would permit continued water injection. It is likely that the system would have oscillated during the early period of the test.

The tanks were positioned to provide initial net driving heads of 0.05, 0.1, 0.15, and 0.2 bar. The net driving head ΔP is defined here as the head remaining after subtracting the hydrostatic head associated with the melt; i.e.,

$$\Delta P = \rho_l g L - \rho g h \Big|_{corium} \tag{3-1}$$

where h is the height of the corium (30 cm), L is the distance from the bottom of the corium pool to the tank water surface, and ρ_l and ρ are the coolant and corium densities, respectively. The head associated with the corium was calculated to be 0.18 bar by assuming a density of 6000 kg/m^3. Assuming a water head of 10 meters per bar, the tanks were positioned so that the water surfaces were 2.3, 2.8, 3.3, and 3.8 meters above the bottom of the corium pool.

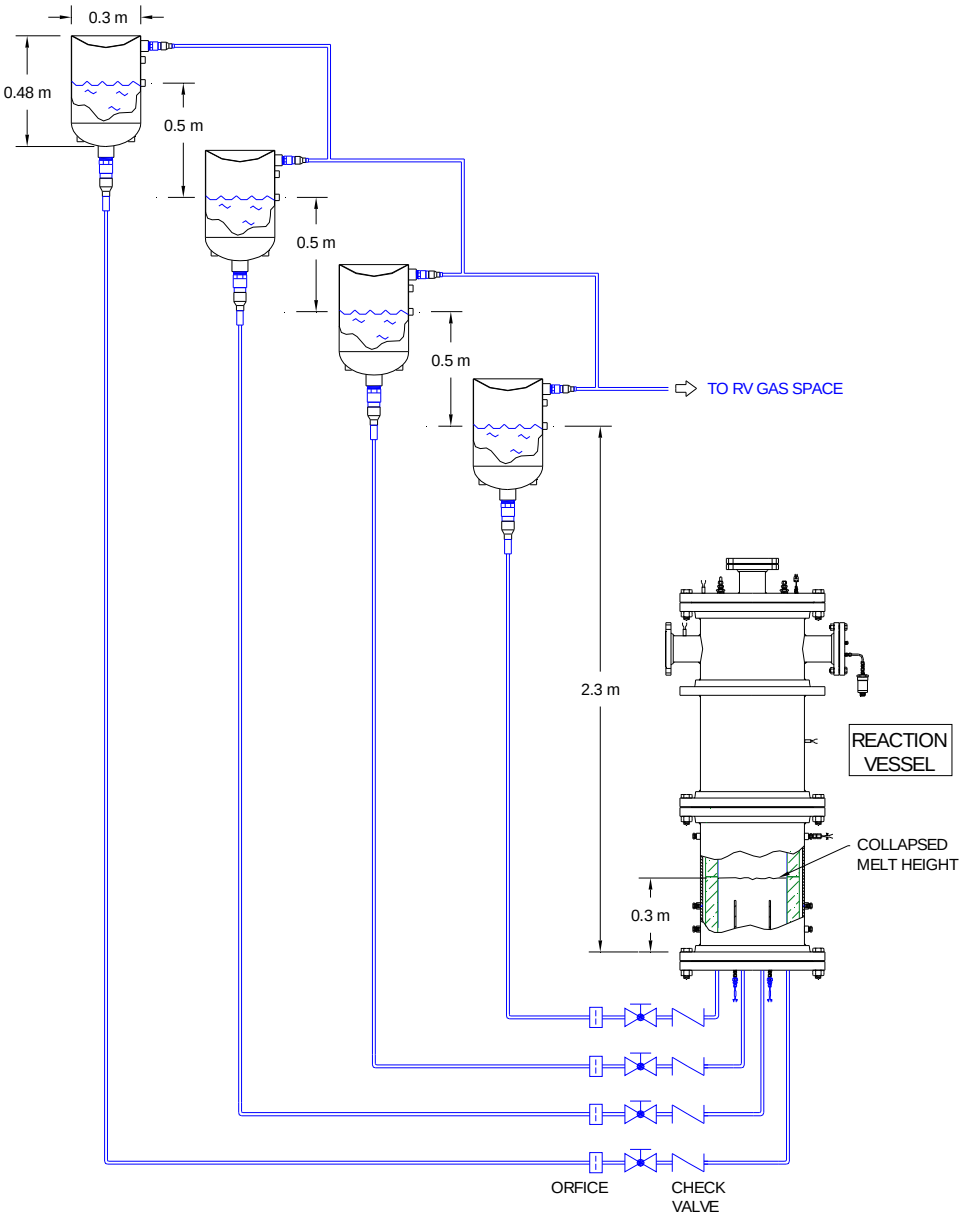

Figure 3-5. SSWICS-12 Water Injection System Geometry (drawn to scale).

In the interest of simplicity, no system was used to replenish the tanks during the test to maintain water level and so the driving head fell as water was injected into the melt. The drop in water level can be made small by using large-diameter tanks, but they serve as pressure vessels during the test and so there is a strong incentive to minimize their size. On this basis, commercially available 30 cm diameter pressure vessels were selected for use. The initial water inventory for each tank was 15 liters for SSWICS-12, yielding a total inventory of 60 liters. This volume was selected to ensure that there would be sufficient water available to completely quench the 136 kg core melt mass to the saturation temperature. The tank level would thus decline by 20 cm during injection of the entire water inventory.

3.1.3 Injection Nozzles

The design for the concrete nozzles that were used in SSWICS-12 is shown in Figure 3-6. Four nozzles were cast within the basemat and positioned so that they were roughly equidistant from the liner and neighboring partitions. The top of each nozzle was flush with the basemat surface and each was filled with porous concrete [7] to provide a path for water flow up into the melt while preventing melt flow downward into the nozzle. A photograph showing the nozzles after installation in the basemat is provided in Figure 3-4. The porous concrete filled nozzle was of interest because it mimicked a proposed engineered corium cooling system. This separate effect test offered the opportunity to determine the behavior of the nozzle with prototypical corium. A leak-tight 0.05 mm-thick stainless steel diaphragm was welded over the top of each nozzle to serve as a temporary seal to prevent water flow from the feed line up into the thermite during the vessel preheat phase of the experiment. Melt contact following the thermite burn was expected to rapidly ablate through these thin diaphragms, thereby initiating the water injection phase of the experiment.

As part of pretest operations, orifices (i.e., needle valves) on each of the supply lines from the header tanks to the nozzles were adjusted so that the peak water flowrate to the nozzles would be limited to 0.01 kg/sec each. This action effectively capped the peak corium quenching rate at a level of ~ 1.2 MW/m^2 at saturated coolant conditions if all four nozzles opened completely. This step was taken since the results of previous COMET tests [20] on the same test stand indicated that melt dispersal within the test section could be significant if the steaming rate was not limited.

3.1.4 Instrumentation and Data Acquisition

The test design for SSWICS-12 featured a partitioned melt with an injector in each of the four quadrants. This approach effectively combined four quench experiments into one. Sufficient instrumentation was provided to determine the boundary conditions and cooling behavior of the individual partitions. The flow rate and driving pressure of each nozzle was measured along with melt temperatures. The condensate collection and measurement system used in past tests to determine the steaming rate was also used, but it could not provide the cooling rate of any particular partition. Rather, the gross melt cooling rate was measured. Only indirect indications of individual partition cooling rates, obtained through measurements of melt temperature and water flow rate into each quadrant, were available for these tests.

Figure 3-7 shows the thermocouple layout in the basemat and the liner for SSWICS-12. Each partition was allotted a 5-junction C-type thermocouple in a tungsten thermowell. The thermocouples were spaced every 51 mm so that the uppermost thermocouple was 190 mm above the basemat surface. The tungsten thermowells were 9.5 mm diameter, which is the same size used in the WCB-1 (see Section 2.0), but larger than that used in previous SSWICS tests (6 mm). Though thermowell size should be minimized to limit fin cooling effects, the thermowells for this test were too long to fabricate in a diameter less than 9.5 mm.

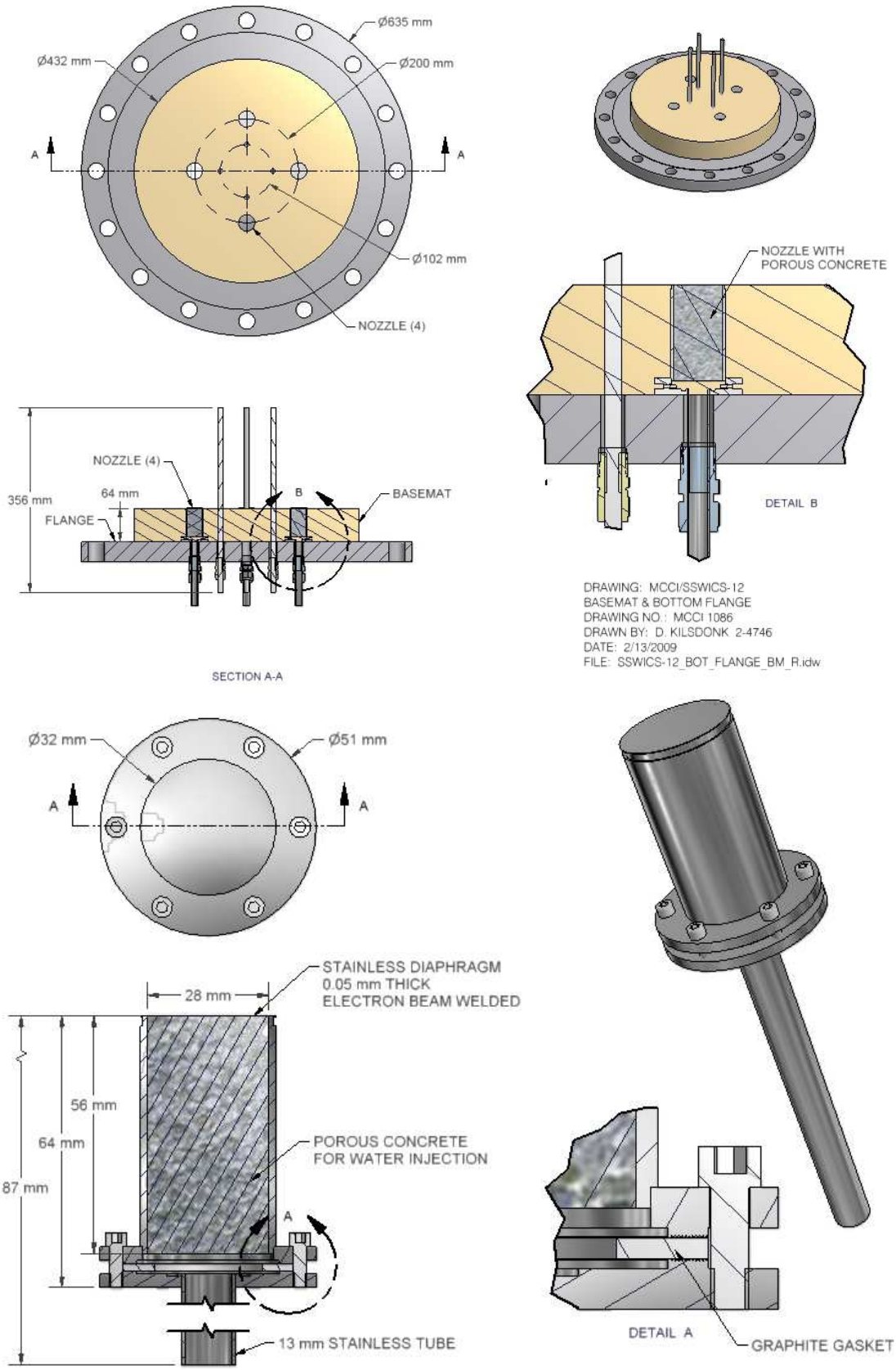

Figure 3-6. SSWICS-12 Nozzle Layout on Basemat (top) and Nozzle Detail (bottom).

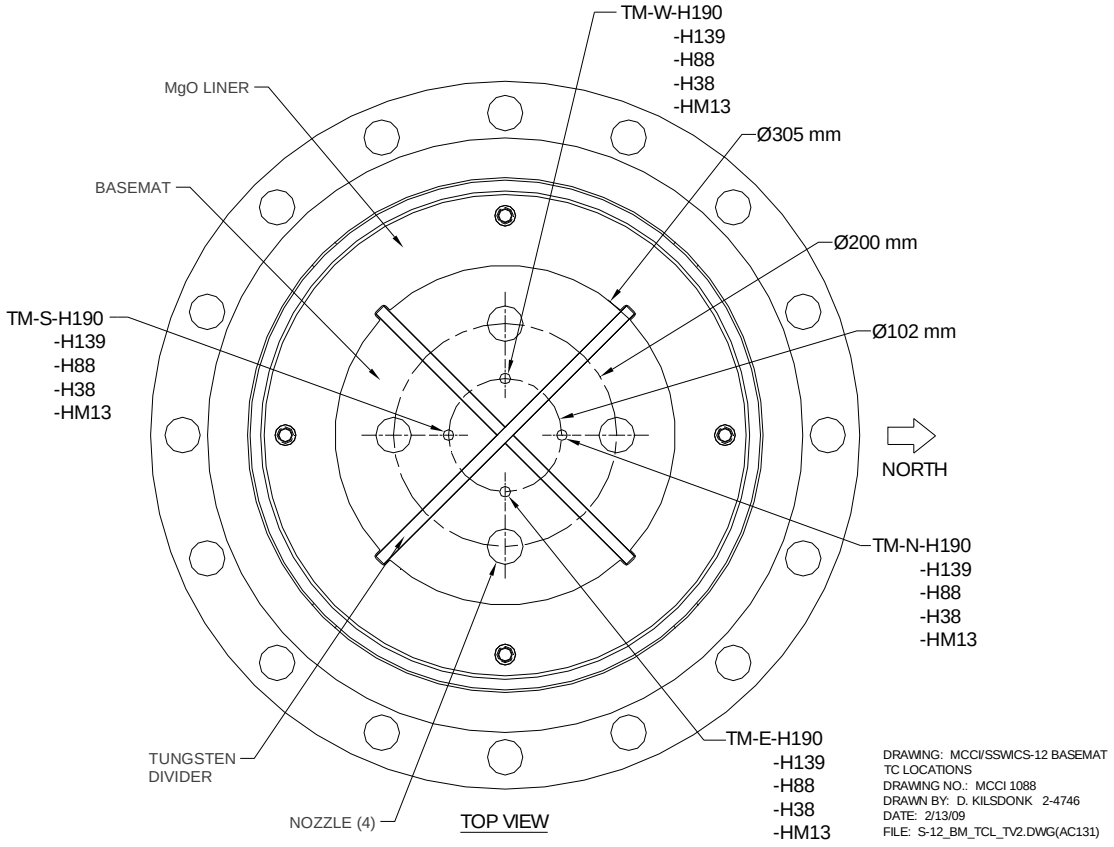

Figure 3-7. Melt Thermocouple Locations for SSWICS-12.

The nomenclature used to identify thermocouples is as follows: TM (temperature within the corium melt), TF (fluid temperature), TG (gas space temperature), TS (structure temperature), H# (height above the bottom of the melt), in mm, and N, S, E, W representing the cardinal points. The partition was oriented so that the "wedges" faced towards the cardinal points. For example, TM-N-H190 is the melt thermocouple in the north facing wedge, 190 mm above the bottom of the melt.

Aside from the test section, the balance of the facility was instrumented in order to provide the necessary information to assess the nozzle injection flowrates as well as the overall steaming rate from the test section. The instrument locations and nomenclature are shown in Figure 3-2. Water levels in the header tanks were monitored with differential pressure transducers; the time-derivative of this data was intended to provide the estimate of water flow rate to the nozzles. Temperature rise across the condenser was measured with Type K thermocouples, while water flow rate through the condenser was measured with a paddlewheel flowmeter. The water level in the CT was monitored with a time domain reflectometer with a redundant measurement provided by a differential pressure transducer. Measurement uncertainties for the various instruments utilized in the tests are summarized in Table 3-1.

Table 3-1. Summary of Data Measurement Uncertainties for SSWICS Tests.

Measurement	Instrument	Accuracy
Temperature (other than melt)	Type K thermocouple	± 2.2 ºC or ± 0.75 %
Temperature (melt)	Type C thermocouple	± 4.5 ºC or ± 1.0 %
Pressure	Pressure transducer	Differential: ± 0.4 kPa Absolute: – test section: ± 14.0 kPa – tasemat gas sparger: ± 2.0 kPa
Water flow rate	Paddlewheel flowmeter	± 0.3 lpm
Gas flow rate	Mass flowmeter	± 0.003 lpm
Water level	Time domain reflectometer	± 3.0 mm
Corium-water heat flux	Calculated	± 17 kW/m^2 [(a)]

[(a)] See Reference [10] for basis.

All data acquisition and process control tasks for the SSWICS tests were managed by a PC executing LabVIEW 8.2 under Windows XP. Sensor output terminals were connected to model HP E1345A 16-channel multiplexers and the signals were digitized by an HP E1326B 5 ½ digital multimeter located within the test cell (Figure 3-8). Signal noise was reduced by integration over a single power line cycle (16.7 ms). The digitized sensor readings were routed from the test cell to the PC in the control room via two HP-IB extenders. The extenders allowed the ASCII data from the HP to be sent through the cell wall over a BNC cable. The extender within the control room then communicated with a GPIB card within the PC. This configuration also permitted remote control of the multimeter through LabVIEW. The power line cycle integration resulted in a minimum (theoretical) time of 0.75 s to scan the channel list. In practice, however, the acquisition of a single scan was at a frequency of ~ 0.5 Hz.

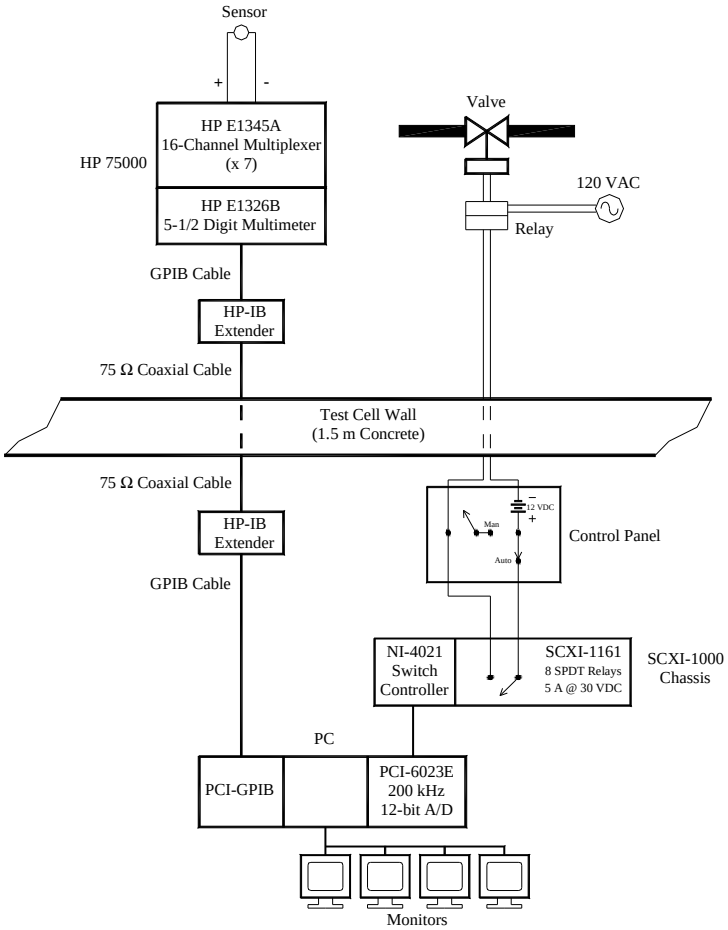

Figure 3-8. SSWICS Data Acquisition and Control Systems.

Valves were controlled with the PC using a relay card housed within an SCXI chassis (National Instruments). These electromechanical relays were capable of switching up to 8 A at

125 VAC or 5 A at 30 VDC. They were operated via a switch controller in the SCXI chassis, which communicated with the PC through a general-purpose data acquisition card. As shown in Figure 3-8, the relays in the control room operated devices within the test cell indirectly, through a second relay. This was intended to provide an additional level of electrical isolation between the NI switching hardware and high voltage sources within the cell. As an added safety measure, all wiring was routed through a control panel that could be switched from automatic (PC) control to manual control in the event of computer failure.

3.1.5 Corium Composition

The oxide phase of the corium composition for SSWICS-12 and -13 was the same as that used in SSWICS-6 (i.e., 60.3/24.7/15.0 wt % UO_2/ZrO_2/siliceous concrete [29]). The thermite was, however, slightly reformulated to react at a higher temperature to minimize crust formation on the basemat that might impair initial water flow through the nozzles. The initial melt temperature for SSWICS-6 was ~1950˚C while the target initial temperature for these tests was ~ 2100˚C. Reformulation of the thermite to produce the higher reaction temperature resulted in a slightly higher Cr metal byproduct content of 7.6 wt % in the melt, which can be compared to the level of 6.4 wt % for the SSWICS-6 thermite. The initial thermite powder loading for both SSWICS tests is shown in Table 3-2, while the pre-and post-reaction compositions are provided in Table 3-3.

Table 3-2. Thermite Charge for SSWICS Tests.

Constituent	Mass (kg)
U_3O_8	78.61
CrO_3	19.90
CaO	2.96
Zr	22.98
Mg	0.10
Si	3.51
SiO_2	7.49
Al	0.45
Total	136.0

Table 3-3. SSWICS Thermite Reaction Compositions.

Constituent	Wt %	
	Reactant	Product
U_3O_8	57.80	-
UO_2	-	55.61
Zr	16.90	-
ZrO_2	-	22.84
Si	2.58	-
SiO_2	5.51	11.03
Mg	0.07	-
MgO	-	0.11
Al	0.33	-
Al_2O_3	-	0.63
CaO	2.18	2.18
CrO_3	14.63	-
Cr	-	7.60

3.2 Facility Modifications for SSWICS-13

The overall facility design for SSWICS-13 was similar to that used for SSWICS-12, but with the following exceptions: i) the apparatus was modified such that the melt was partitioned into two sectors instead of four, ii) the injector design was changed from porous concrete to a tubular steel construction, and iii) the supply system to the injectors was modified to provide a two-phase gas-water mixture to selected injectors. These changes required some instrumentation modifications, principally to characterize the two-phase flow to the nozzles. These various facility modifications are summarized in this section. Conversely, the corium composition and data acquisitions for the two tests were identical; refer to Section 3.1 for details.

3.2.1 Test Apparatus

The reaction vessel and overall quench facility layout for SSWICS-13 were identical to that used in SSWICS-12 (see Figures 3-1 and 3-2). However, for SSWICS-13 the corium was divided into two sectors as opposed to four. The results of SSWICS-12 indicated

that the 10 mm thick tungsten plates that were used to partition the melt survived the test intact, and that they functioned as well as could be expected in terms of maintaining a well-defined experiment configuration. Thus, the same design (but new material) was used for SSWICS-13. The test section was divided into two by a 60 cm-high wall made up of three 20 cm high, 10 mm thick plates. The partition was supported by grooves that were cast in the MgO liner to prevent shifting under lateral loads. The SSWICS-13 basemat detail is provided in Figure 3-9, while a photographs showing the lower section at various stages of assembly is provided in Figure 3-10.

Another modification for SSWICS-13 was the fact that the upper 25 mm of the basemat was fabricated from locally obtained limestone/common sand concrete. As shown in Figure 3-9, the injection nozzles were positioned 10 mm beneath the concrete surface. To ensure that the nozzles did not plug during pouring of the concrete, the surface of each unit was covered with a layer of Scotch tape. The purpose of the concrete overlayer was to protect the nozzles from coming into immediate contact with the melt following the thermite burn, as this might have plugged the nozzles before the operators had a chance to open valves and establish the basemat water flow.

3.2.2 Injection Supply System

As for SSWICS-12, each nozzle was fed by a single supply tank so that a differential pressure transmitter could be used to measure the flow rate to individual nozzles. The nozzles were gravity fed so that the driving pressure for injection was set by the elevation difference between the nozzle and the tank water level (Figure 3-11). A check valve was also placed in each line prevent back flow up into the tank. One change for SSWICS-13 was that an isolation valve was added on each line that could be opened remotely from the control room once the melt had contacted the basemat. This feature was added due to the fact that the SSWICS-13 injection tubes were not sealed at the top as they were (using a thin steel diaphragm) in SSWICS-12. Thus premature opening of these lines would have led to water seepage into the thermite, and this would have severely degraded the thermite reaction.

As discussed in the previous section, the water flowrate to each injector for SSWICS-12 was limited to 0.01 kg/s in an attempt to minimize melt dispersal from the expanding steam in the early portion of the test. However, the results (see next section) indicated that even with this restriction, melt was ejected from the lower plenum leaving a coating over most of the inside of the RV that caused a peak plenum temperature of 1700^{o}C. On this basis, provisions were made in SSWICS-13 for supplementary injection of 20 liters of water from the top shortly after water flow from below was established. The purpose was to cool the superheated steam generated in the very early stages of the test. As a further step in limiting melt dispersal, metering valves on each supply line were adjusted to allow a peak water flowrate of 0.005 kg/s at the initial fill level, which was half of that for SSWICS-12. This step limited the maximum achievable debris cooling rate by bottom water injection to a level ~ 600 kW/m^2 at saturated coolant conditions.

3.2.3 Injection Nozzles

The nozzle design is illustrated in Figure 3-12. Water left the nozzle and entered the melt through four 1 mm-diameter holes. The holes were positioned 4.5 mm from the nozzle center. The nozzle itself had a diameter of 12 mm and all components were made of stainless steel. The

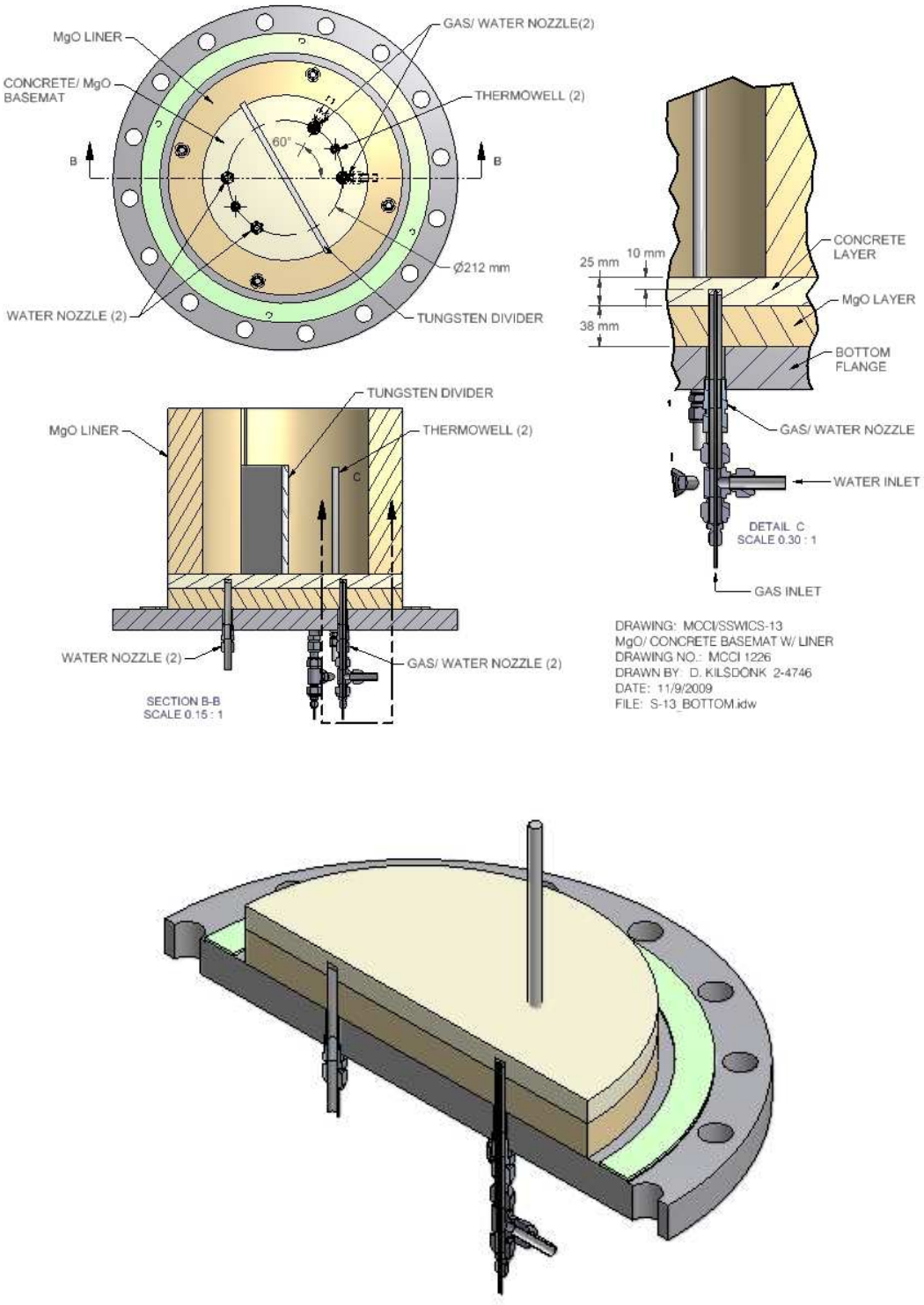

Figure 3-9. SSWICS-13 Lower Plenum and Basemat Detail.

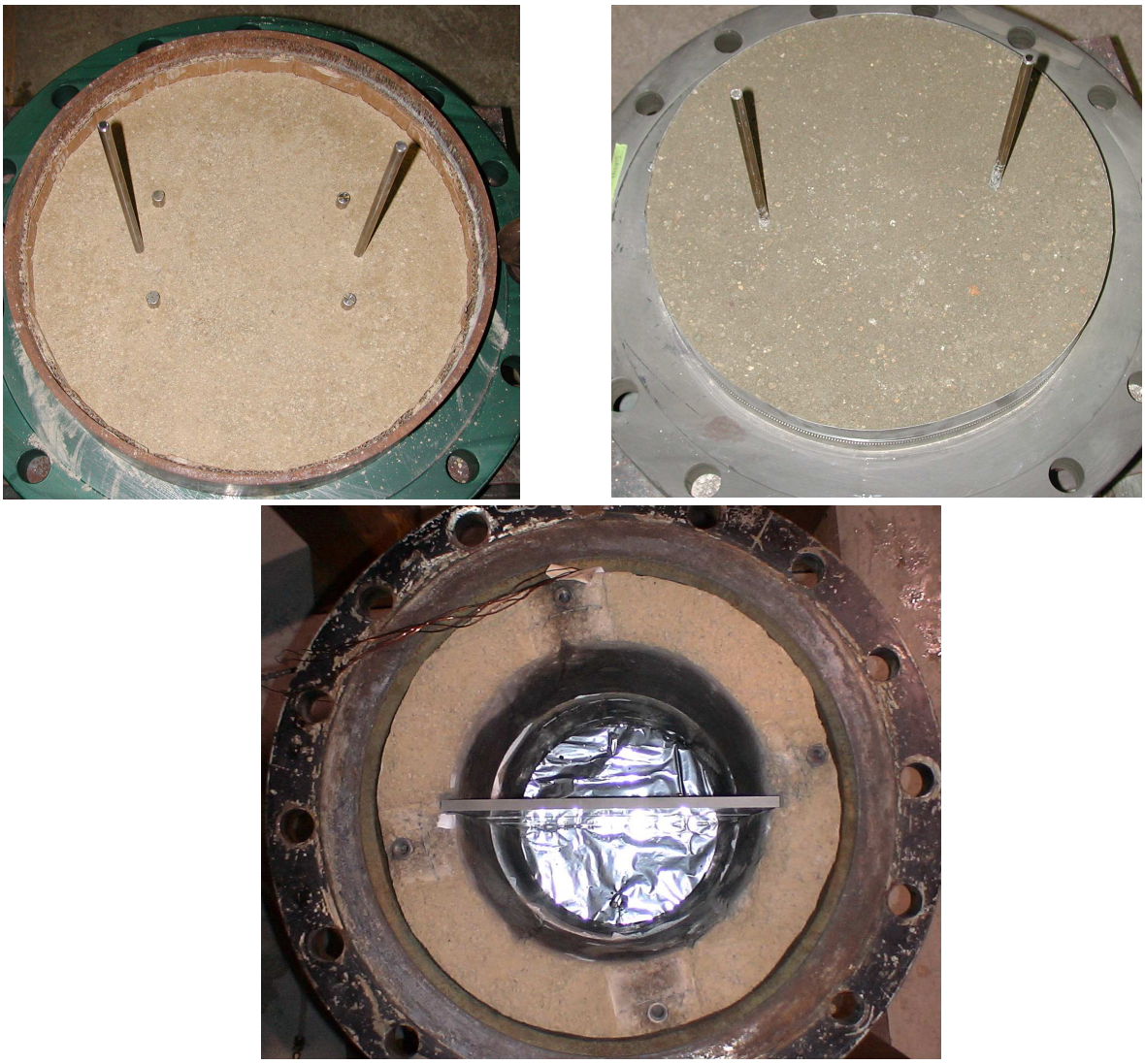

Figure 3-10. SSWICS-13 Basemat Before (top-left) and After (top-right) Concrete Placement, and Assembled Lower Section (bottom).

two nozzles injecting nitrogen had an additional 1-mm hole at the center. The nitrogen and water were expected to mix together as they entered the melt. As shown in Figure 3-9, the nozzles were all cast in the basemat such that the nozzle surfaces were 10 mm below the concrete surface.

The gas flowrate to the two nozzles that were to inject a two-phase mixture was specified to be 20% of the initial volumetric flow rate of the water. The original plan was to deliver the gas using a flow controller set at a constant flow rate. However, there was concern that the forced gas flow might suppress the natural circulation water flow since the two are combined beneath a heavy corium pool. There was also concern that the combination of forced and natural circulation flow would not generate good gas/water mixing near the nozzle. To address these concerns, the decision was made to switch to a pressure regulated flow.

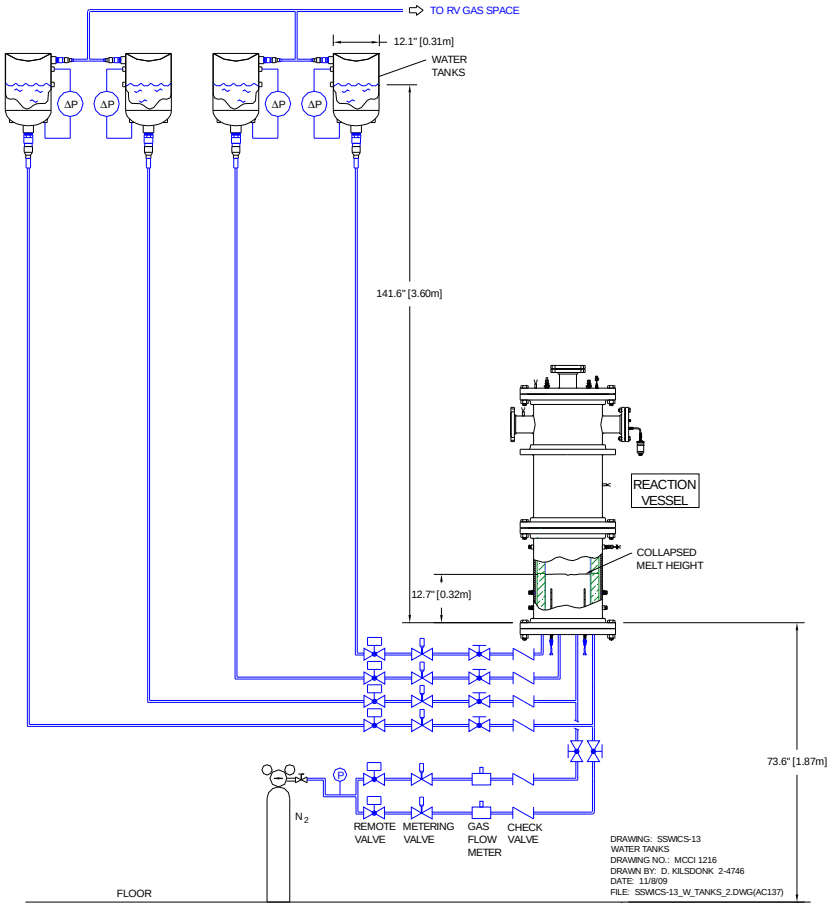

Figure 3-11. SSWICS-13 Water Injection System Geometry (drawn to scale).

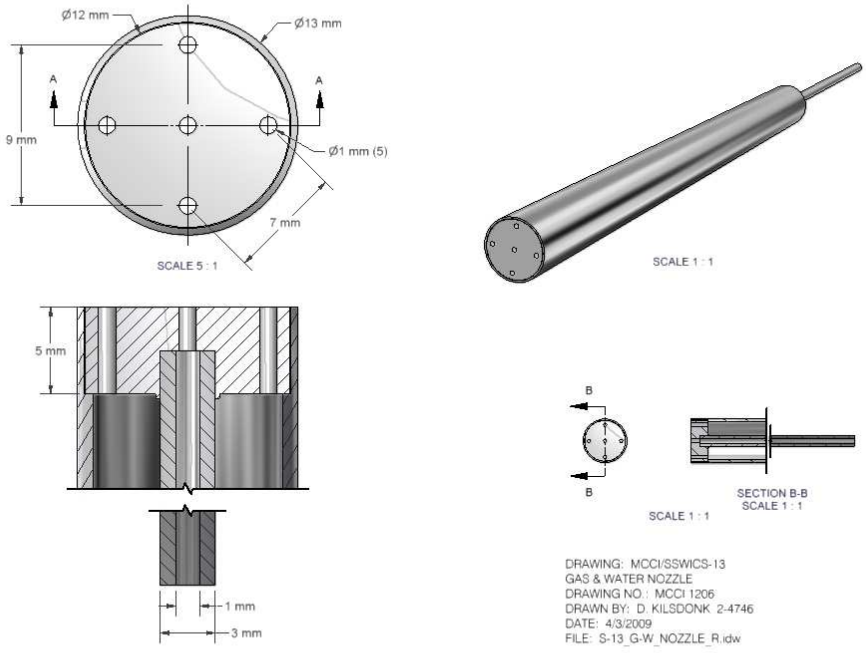

Figure 3-12. SSWICS-13 Nozzle Detail.

The gas system shown in Figure 3-13 was configured with an approach similar to that used for the water. The initial flow rate to each nozzle was defined (0.06 lpm), as was the maximum driving pressure at the nozzle exit (0.2 bar to match the initial net driving head set for the water). The head associated with the corium was 0.15 bar and so the gas source pressure was set at 0.35 bar to provide the net 0.2 bar driving pressure.

The metering valve was used to adjust the line losses to achieve the target flow rate. Since the corium was not present beforehand to contribute to the net head, the adjustment had to be made without it. The capillary was removed from the fitting at the Swagelok tee shown in Figure 3-13. With the source pressure at 0.35 bar, the pressure drop between the source and the end of the gas line was 0.35 bar rather than the 0.2 bar expected during the test. The correct valve position was determined by considering the relationship between flow and pressure drop:

$$\dot{V} = N\, C_v\, \Delta P^{1/2} \tag{3-2}$$

where $\dot{V}$ is the volumetric flow rate, N is a constant, C_v the metering valve loss coefficient, and ΔP the pressure drop across the valve. Most of the pressure drop between the source and nozzle occurs across the metering valve. The required C_v (valve position) for 0.06 lpm at 0.2 bar ΔP is found by using the above equation along with the 0.35 bar used to adjust the metering valve; i.e.,

$$\frac{0.06}{x} = \left(\frac{0.2}{0.35}\right)^{1/2} \Rightarrow x = 0.079\, lpm \tag{3-3}$$

Thus, the metering valve position that would provide 0.06 lpm at a ΔP of 0.2 bar would give 0.079 lpm at 0.35 bar. The metering valves were adjusted until the flow meters showed 0.079 lpm as a part of the pretest setup. The isolation valves were then closed and the tubing was reattached to the Swagelok tee.

3.2.4 Instrumentation

As for SSWICS-12, sufficient instrumentation was provided to determine the boundary conditions and cooling behavior of the two partitions. The flow rate and driving pressure of each nozzle was measured along with melt temperatures. The nitrogen gas flow to each of the two nozzles was also measured. The condensate collection and measurement system was also used to characterize the overall debris cooling rate.

Figure 3-14 shows the thermocouple layout in the basemat and the liner for SSWICS-13. Each partition was allotted one 5-junction C-type thermocouple assembly in a tungsten thermowell. The thermocouples were spaced every 51 mm so that the uppermost thermocouple was 195 mm above the basemat surface. The tungsten thermowells and nomenclature used to identify thermocouple locations are the same as those used in SSWICS-12 (see Section 3.1.4).

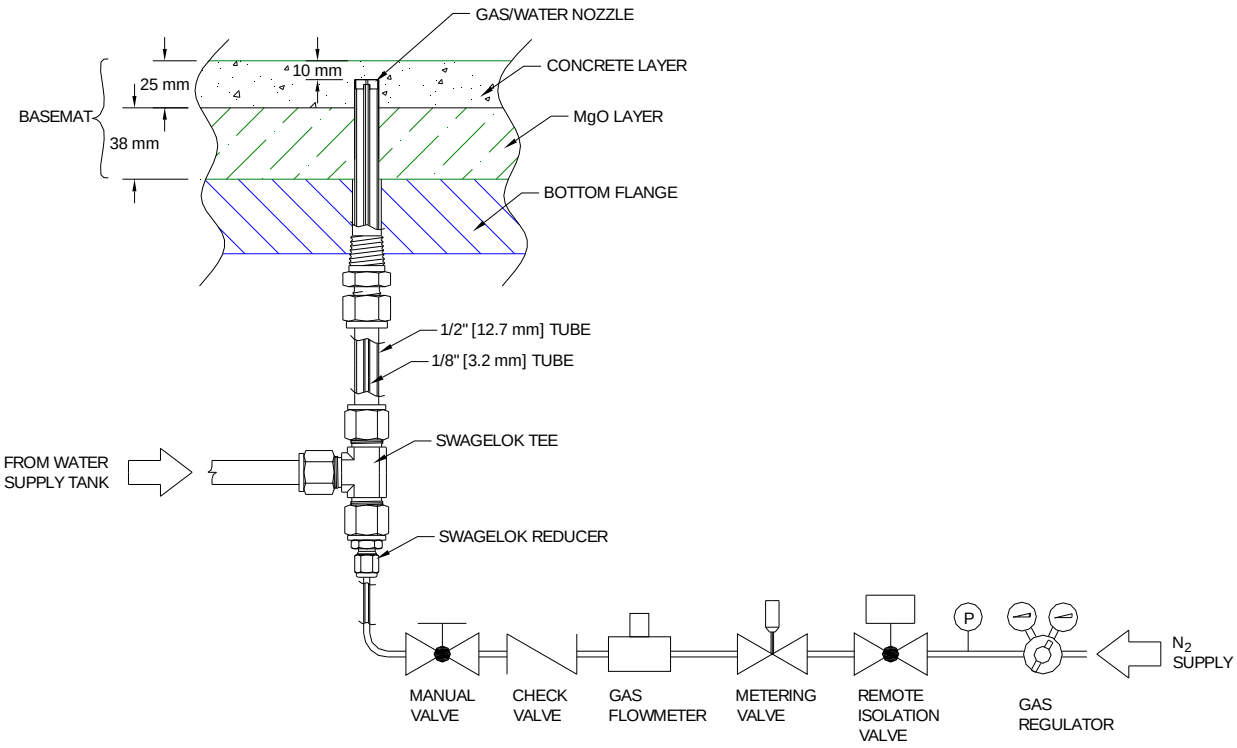

Figure 3-13. Details of Nozzle Design with Gas Injection.

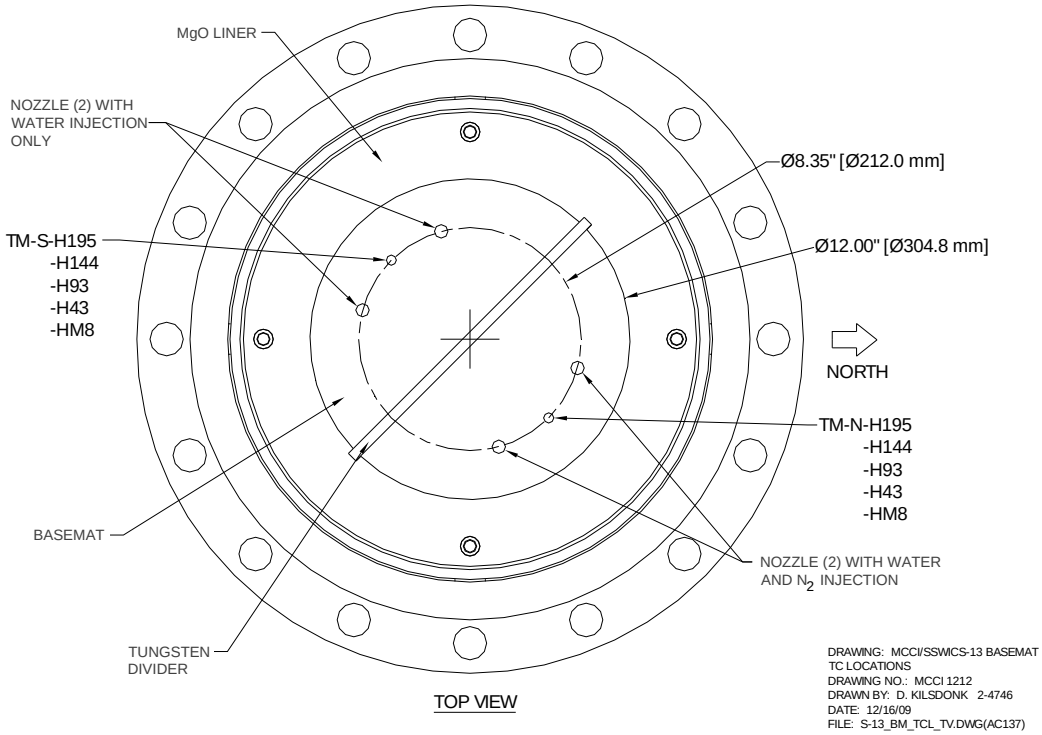

Figure 3-14. SSWICS-13 Melt Thermocouple Locations.

3.3 SSWICS-12 Test Results

3.3.1 Test Operations

The day before the test, the water injection line orifices were adjusted so that each tank would provide an initial flow rate of 0.01 kg/s. The adjustments were made over several fill and drain runs. The day of the test, the tanks were each filled with water to a level of ~0.4 m to provide the initial net driving heads of 0.05, 0.1, 0.15, and 0.2 bar. The isolation valves were opened shortly before the cell was closed for ignition of the thermite.

The RV structures were preheated to ~100°C to minimize heat sink effects after water injection. The igniter coil was then energized to initiate thermite ignition, which was first detected by a sudden rise in the upper plenum gas temperature TG-RV; see Figure 3-15. All data have been plotted such that the x-axis origin corresponds with the initial rise in plenum gas temperature as measured by TG-RV. Thermocouples within each melt partition began rising 30-60 seconds after thermite ignition.

Within the first minute following ignition the video monitors showed evidence of a small fire around the top RV flange. The operators took no action for the next two minutes in the hopes that water injection and steam generation would begin cooling the melt and extinguish the fire. However, it was not possible to confirm early water injection through reservoir level changes because of system pressure fluctuations produced by the thermite ignition (and possibly the water injection itself).

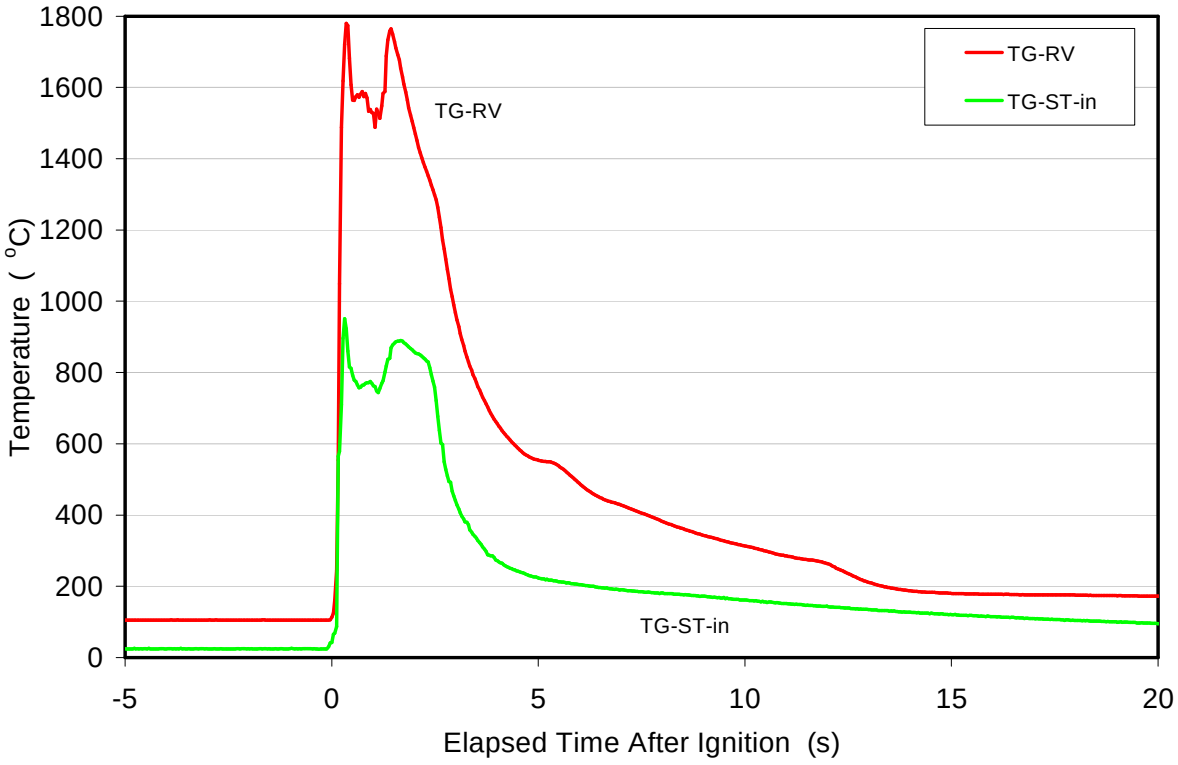

Figure 3-15. SSWICS-12 RV Plenum and Surge Tank Inlet Temperatures.

Sporadic signs of fire continued and after two minutes there was still no clear evidence of water injection from the reservoirs. However, subsequent data analysis and posttest examinations indicated that water injection had indeed been initiated by this time, and the resulting steam generation had ejected melt upward to coat the entire inner surface of the RV, including the lid.

The operators noted gas temperature readings in the test section plenum that exceeded 1700 ºC, and on this basis water injection from above was initiated at 2.3 minutes by opening the isolation valve on the back-up supply line. The line was open for approximately 9 minutes. A temperature increase on the heat exchanger outlet appeared at 2.5 minutes and the condensate tank water level began to rise at 3.2 minutes. Note that the valve to the surge tank was open until ~ 3.7 minutes (Figure 3-16) and so it is likely that, until then, most of the steam flowed to the surge tank rather than the condenser. The reading from the test section pressure transducer (Figure 3-16) indicated an initial ramp up in pressure that began with thermite ignition and then a drop at 2.8 minutes, about 30 seconds after top flooding was started. The pressure drop continued until the surge tank valve was closed. It then quickly rose to the test peak of 1.9 bar.

Melt temperature readings in each of the four quadrants reached a peak of ~ 2000 ^{o}C within three minutes. However, these temperatures began to rapidly decline after water injection and all melt thermocouples reached the saturation temperature by 73 minutes, at which point the test was terminated using normal shutdown procedures.

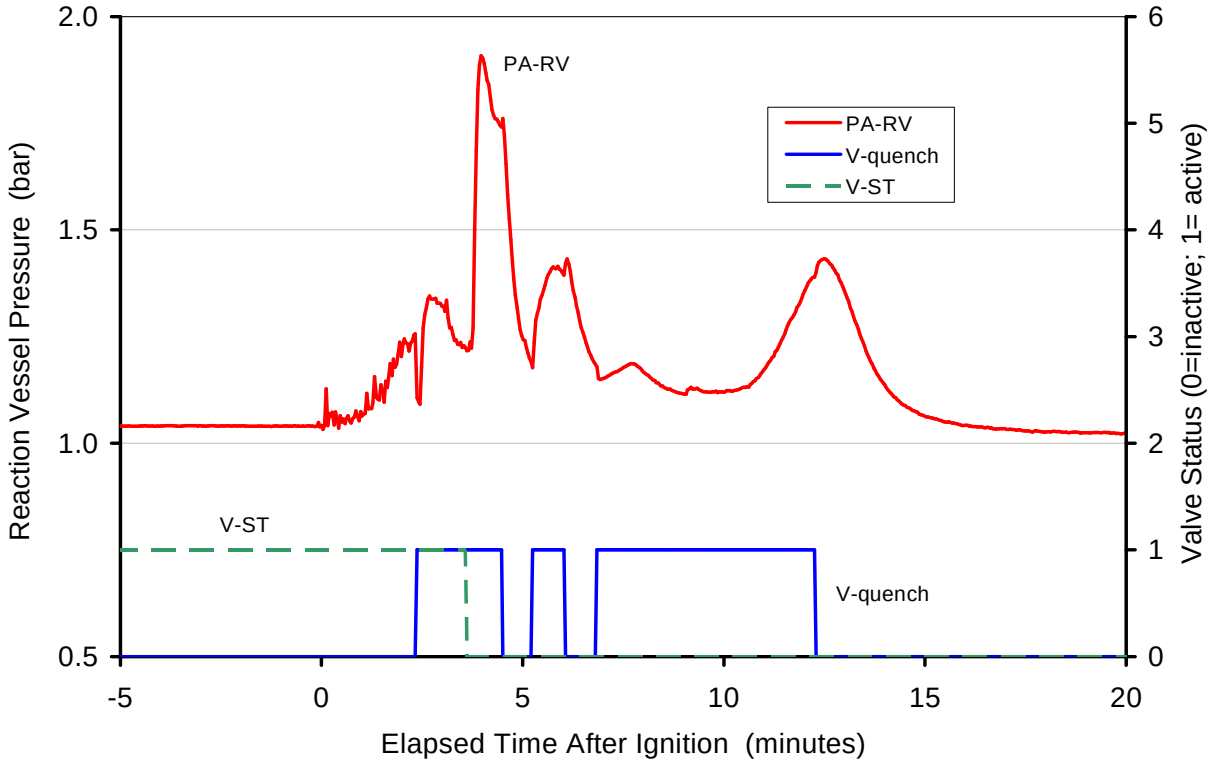

Figure 3-16. SSWICS-12 Test Section Pressure and Valve Positions.

3.3.2 Thermalhydraulic Results

Operationally, SSWICS-12 deviated from the planned procedure in that bottom water injection through the porous nozzles was supplemented by injection from above out of concern for the integrity of the RV. There was no flow meter on this emergency line and it is estimated that ~40 liters were injected from above. Secondly, the reservoir level measurements are considered to be in error, which is likely due to corium plugging of the plenum pressure equilibration line between the test section and reservoir tanks early in the experiment when corium coated the upper internals of the RV [10]. Nonetheless, the data did show that the tanks were all emptied at about the same rate.

Figures 3-17 through 3-20 show melt temperatures measured in each of the four basemat quadrants. The peak temperature of ~ 2000 ^{o}C was reached within 3 minutes. Thereafter, the temperatures turned rapidly around and declined steadily to the coolant saturation temperature. The time for complete quench in the four quadrants ranges from 50 to 73 minutes, with no clear relationship between water head and time to quench. This implies that the water injection rate and subsequent corium cooling behavior are not strong functions of the injection pressure. However, there does seem to be a correlation between the junction location within the melt and the local debris cooling rate. In particular, the junctions at the lowest (i.e., +16 mm) and highest (+168 mm) elevations above the basemat seem to exhibit higher cooling rates in comparison to the rates recorded in the intervening region.

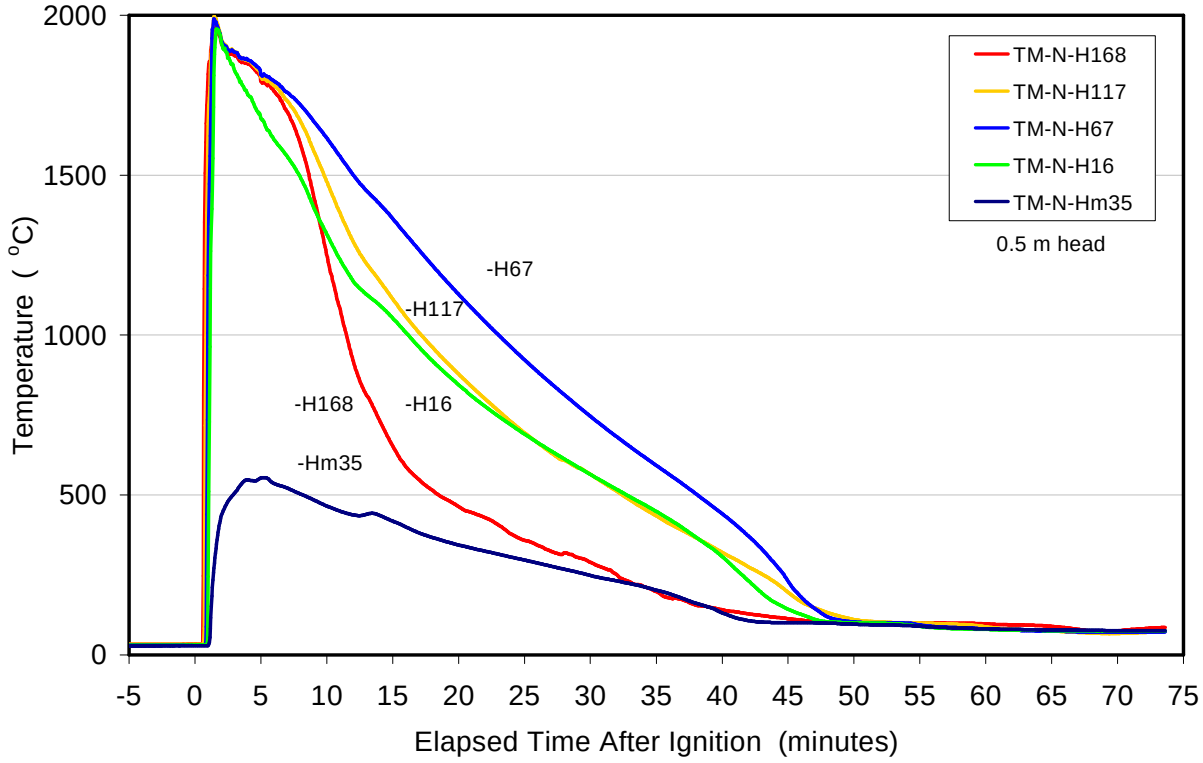

Figure 3-17. SSWICS-12 Melt Temperatures in North Quadrant (Water Head = 0.5 m)

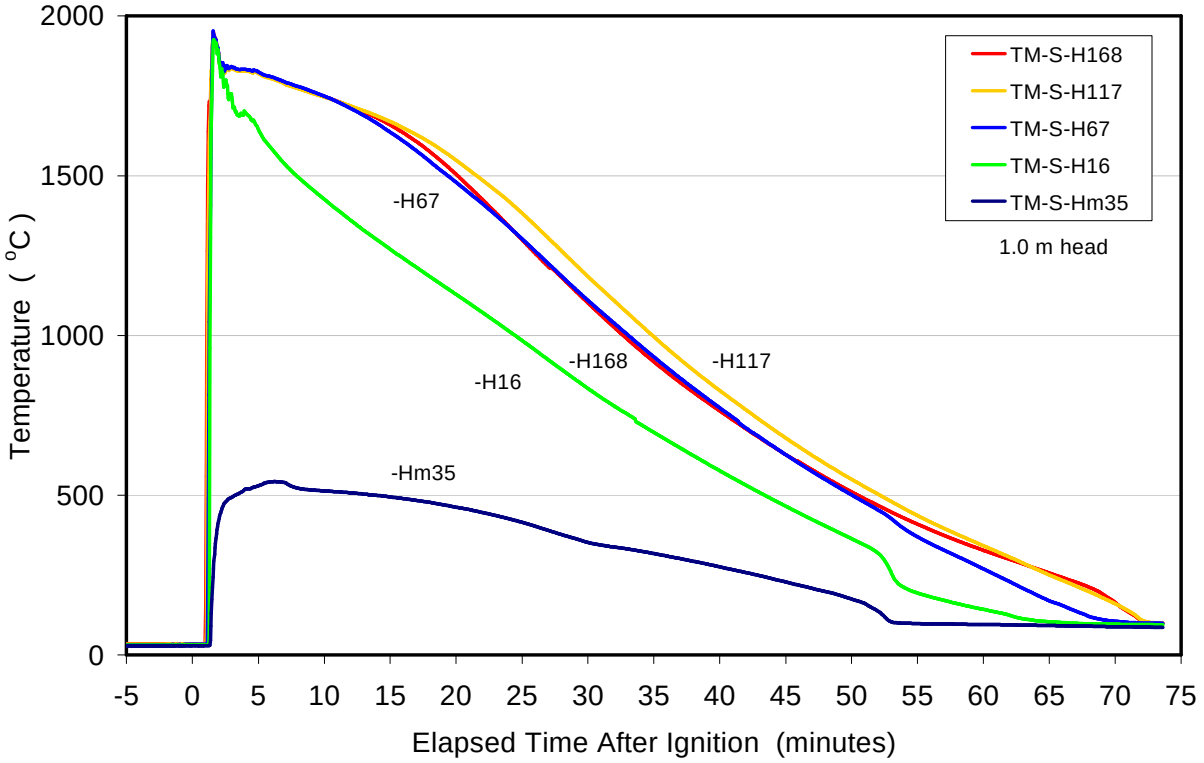

Figure 3-18. SSWICS-12 Melt Temperatures in South Quadrant (Water Head = 1.0 m)

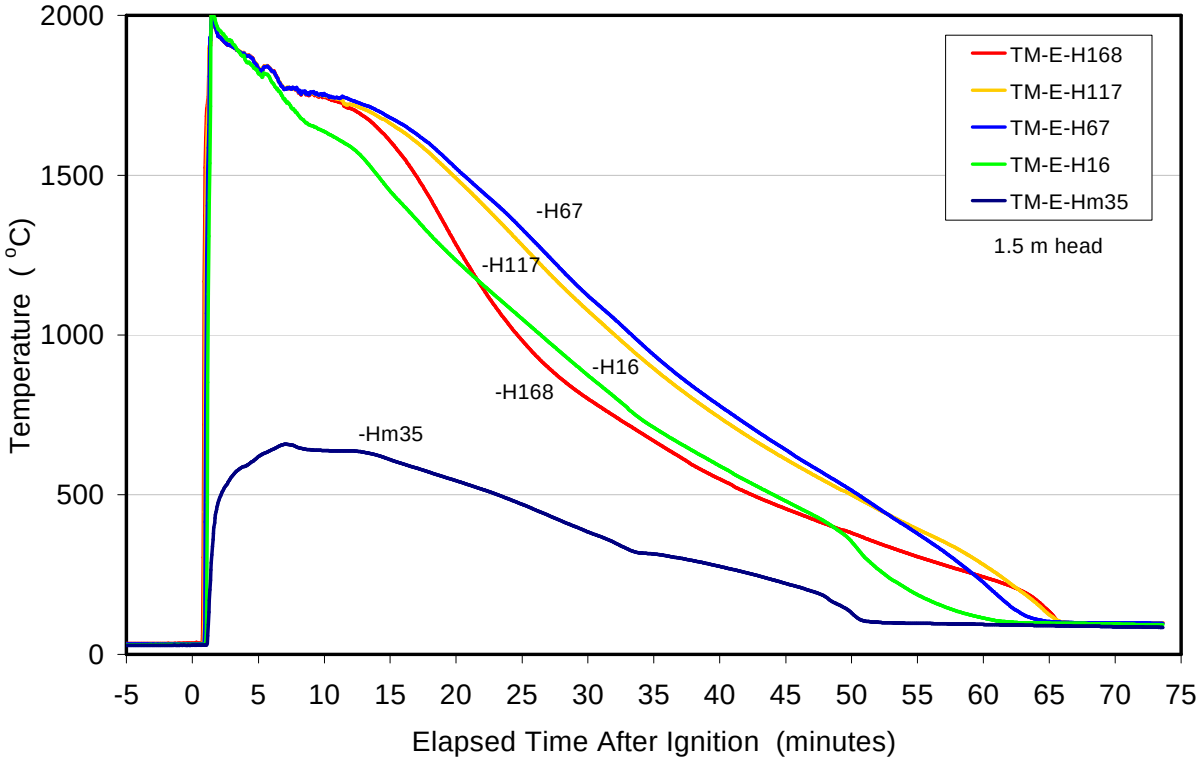

Figure 3-19. SSWICS-12 Melt Temperatures in East Quadrant (Water Head = 1.5 m)

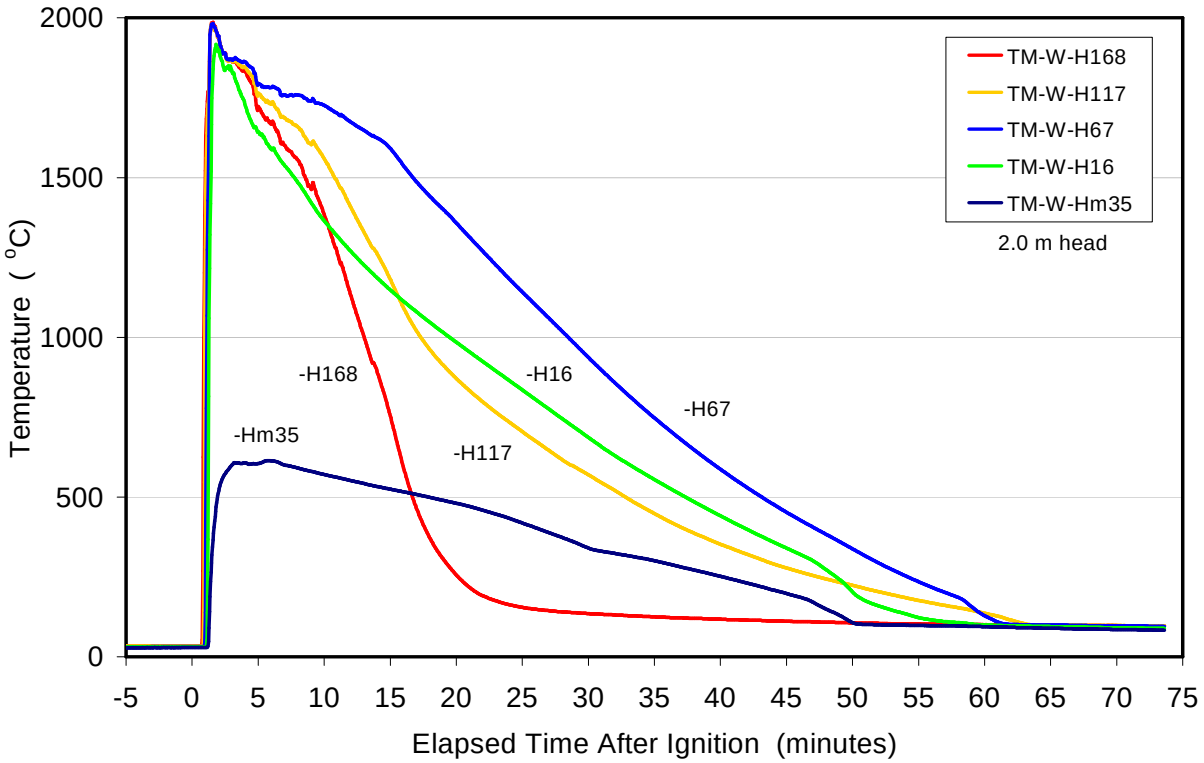

Figure 3-20. SSWICS-12 Melt Temperatures in South Quadrant (Water Head = 2.0 m)

Figure 3-21 provides the debris-water heat flux derived from measurements of condensed steam flow and from an energy balance on the heat exchanger that condenses the steam. Two independent measurements were used within the condensate tank: a differential pressure sensor (DP) that measured water column head and a time domain reflectometer (TDR) that measured water column height. The heat exchanger energy balance was derived from a flow measurement on the HX secondary side along with inlet and outlet thermocouples. Details of the data reduction can be found in the data report [10]. As described in Section 3.1.3, metering valves on the injection lines were adjusted to limit the peak water flow to a level that would yield a corium quenching rate of ~ 1.2 MW/m^2 at saturated coolant conditions. However, in the early portion of the test (t < 12.5 minutes), the debris was cooled from both below and above due to the fact that water was added from the top to reduce the RV plenum temperature. Thus, comparison of the heat flux with this value is not that meaningful. However, by 65 minutes the data indicate that the corium had been effectively quenched. The specific enthalpy change upon complete quench of the SSWICS-12 melt composition from 2000 ºC to saturation was estimated to be 1.3 MJ/kg. Given the quench time (65 minutes), initial melt mass (136 kg), and the test section planar area (0.071 m^2), the average heat flux during the transient was thus calculated to be 640 kW/m^2. This heat flux is noted to be significant in comparison to the fluxes observed in previous SSWICS tests [3] in which the melt was only flooded from the top.

With respect to the derived heat flux data shown in Figure 3-21, note that the underlying calculation assumes a well-defined corium surface area equivalent to the test section planar area [10,11]. In early tests, nearly all the corium remained within the bottom liner to form an ingot with a surface area defined by the inner diameter of the MgO liner. However, for both Tests 12

and 13 with water injection from the bottom, melt was ejected throughout much of the test section and so corium surface area was not well defined. The heat flux plot shown in Figure 3-21 is useful mainly for comparing the heat load with previous tests. This could also be done without assumptions of corium geometry by comparing condenser heat loads in Watts. Previous test results were presented in terms of heat flux due to the interest in measuring the dryout heat flux and so results have been presented here with the same scaling even though the corium surface area is not as well defined, at least in the early part of the test when the relatively thin layer of material covering the upper surfaces is undergoing quench to coolant saturation.

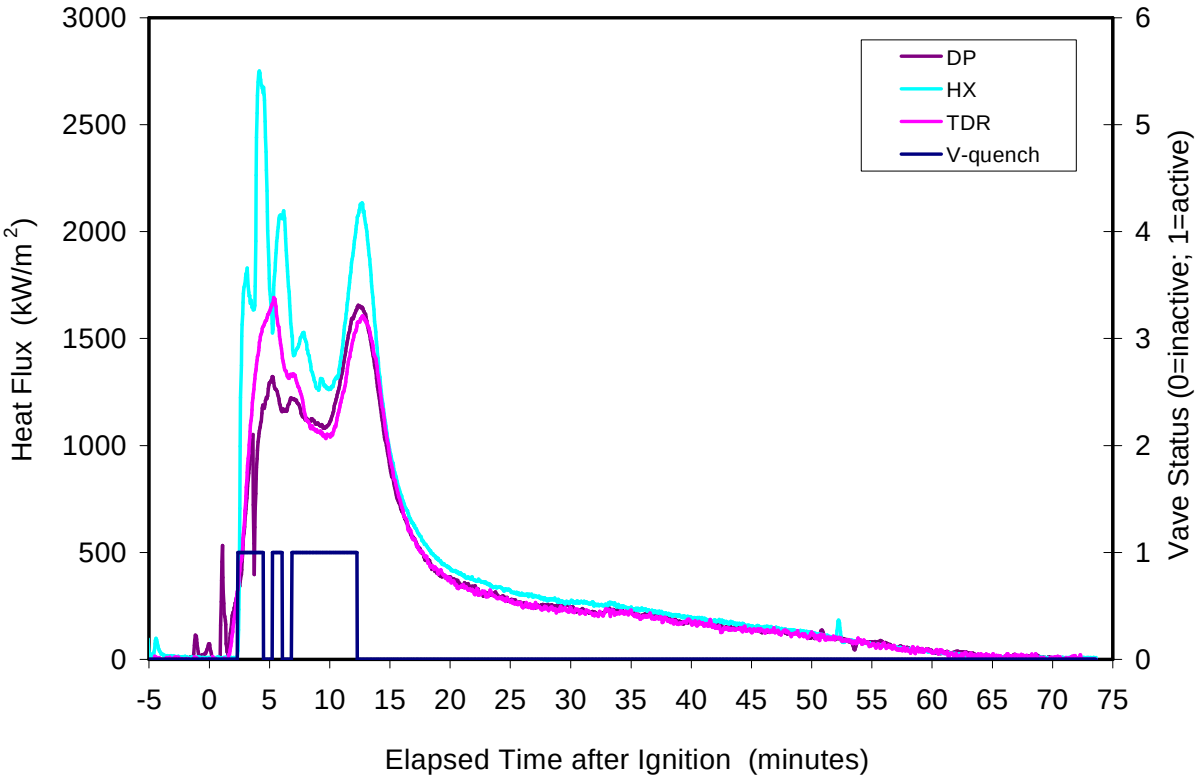

Figure 3-21. SSWICS-12 Debris-Water Heat Flux.

3.3.3 Posttest Examinations

Despite the fact that the water injection flowrate was limited in SSWIC-12, the melt was still ejected above the MgO liners. This can be compared with the results of previous SSWICS tests in which the maximum corium height was essentially limited to the initial thermite powder height. Photographs were taken in order to document the corium distribution. Figure 3-22 shows the lower assembly with all three MgO liners in place before and after the test. The figure also shows the lower assembly after the test. Only two of the liners are present in the second photograph. The corium coating the liner walls and tungsten plates was approximately 2 cm thick. Figure 3-23 shows a wider view of the assembly that includes the pressure vessel; this photograph illustrates the characteristics of this crust material.

Additional examinations revealed that the corium had also coated the upper internals of the RV. Figure 3-24 provides a view from below of the upper plenum after the lower assembly

had been removed. The circular plate seen in the center of this photograph is the baffle used to prevent water droplets from flowing directly up into the steam line (see Figure 3-1). The 6 mm stainless steel tubes used for the four water injection lines were completely melted away by the melt that was splattered into the upper regions of the RV. The steel liner above the third MgO liner was also completely coated with corium, as was most of the baffle plate.

Figure 3-22. SSWICS-12 Pretest (left) and Posttest (right) Views of Lower Test Assembly.

Figure 3-23. SSWICS-12 Lower Plenum Showing Crust above Tungsten Partition.

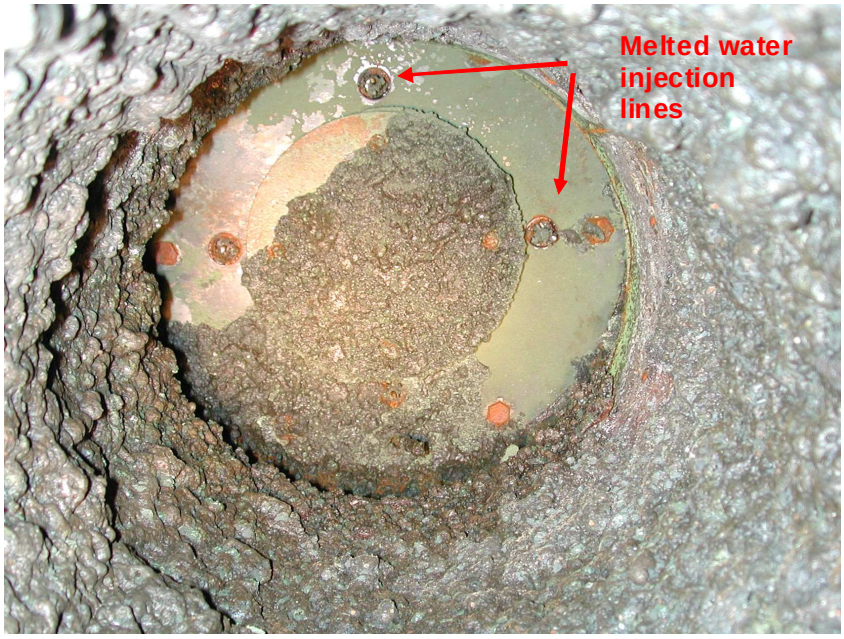

Figure 3-24. SSWICS-12 View of Top Flange Looking Upward Through Upper Plenum.

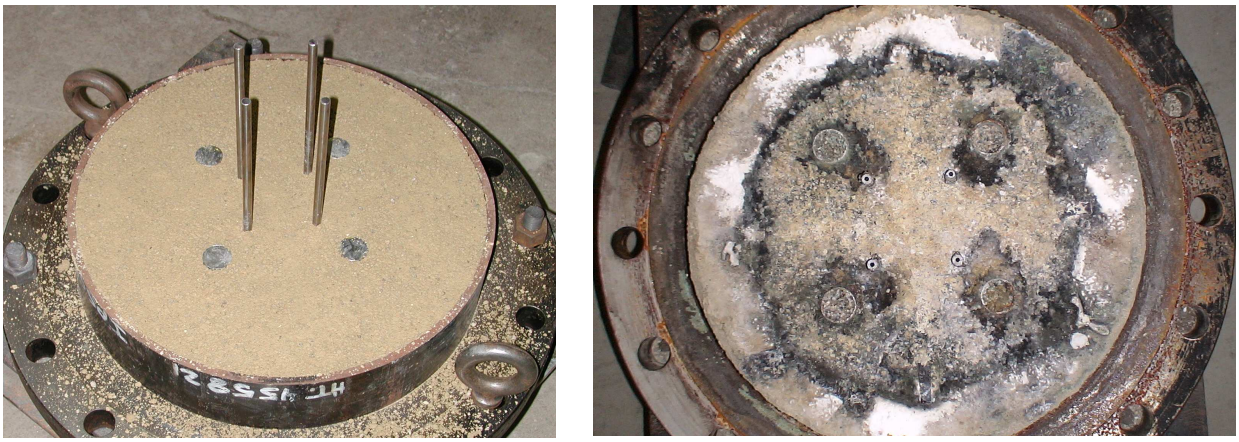

Figure 3-25. SSWICS-12 Pretest (left) and Posttest (right) Views of Basemat Assembly.

The lower section of the RV was subsequently lifted free from the test section bottom flange using the cell crane in order to reveal the remnants of the basemat. Figure 3-25 provides pretest and posttest photographs. Close examination of these figures confirms that each nozzle diaphragm melted as planned and that the porous concrete remained within the nozzle housing.

Figure 3-26 shows the distribution of corium collected from the vessel. As the apparatus was disassembled, corium was scraped from selected zones, collected and weighed. The top zone includes the underside of the flange and baffle and the sides of the pressure vessel above the steel liner. The second zone consists of the steel liner and the third corresponds to the top MgO liner. The fourth zone extends from the top of the second liner down to the top of the tungsten partition and corium in the remainder of the vessel is grouped into the fifth zone. The mass for this lowest zone was assumed to be the balance from the initial 136 kg thermite charge.

Note that corium occasionally fell from the walls during disassembly. Also, corium from one zone might have fallen off during collection of corium from a neighboring zone and so there was some mixing of material from various zones. The uncertainty in the mass values given in Figure 3-26 is estimated to be ± 20%. It is likely, however, that the uncertainty is not random and that the masses for the upper regions are skewed slightly low while those of the lower plenum are high (as some corium fell into the lower plenum during disassembly).

Finally, level measurements were made in each of the four quadrants in order to determine the final debris depths remaining over the basemat. These data are shown in Figure 3-27. The level was measured from the corium surface to the top of MgO liner, which was 60 cm above the basemat. Thus, corium depths in each of the four quadrants were as follows: north 19 cm, east 18 cm, south and west 15 cm. These depths can be compared with the initial target collapsed pool depth of 30 cm. The fact that the final heights are significantly less than the target depth is consistent with the debris dispersal that occurred within the test section.

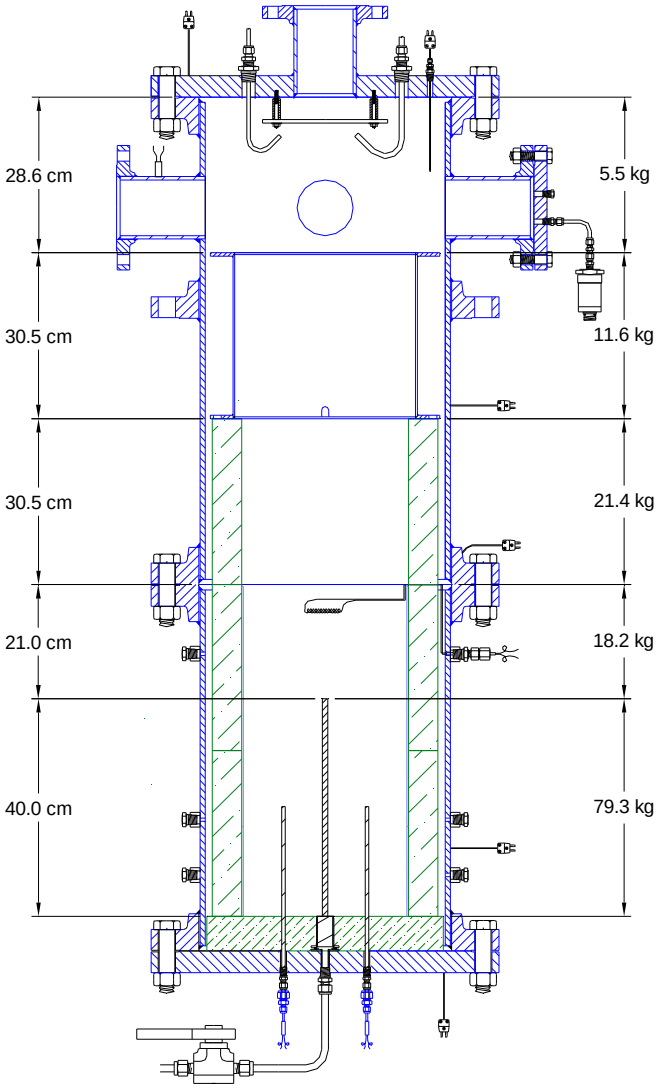

Figure 3-26. SSWICS-12 Posttest Corium Distribution.

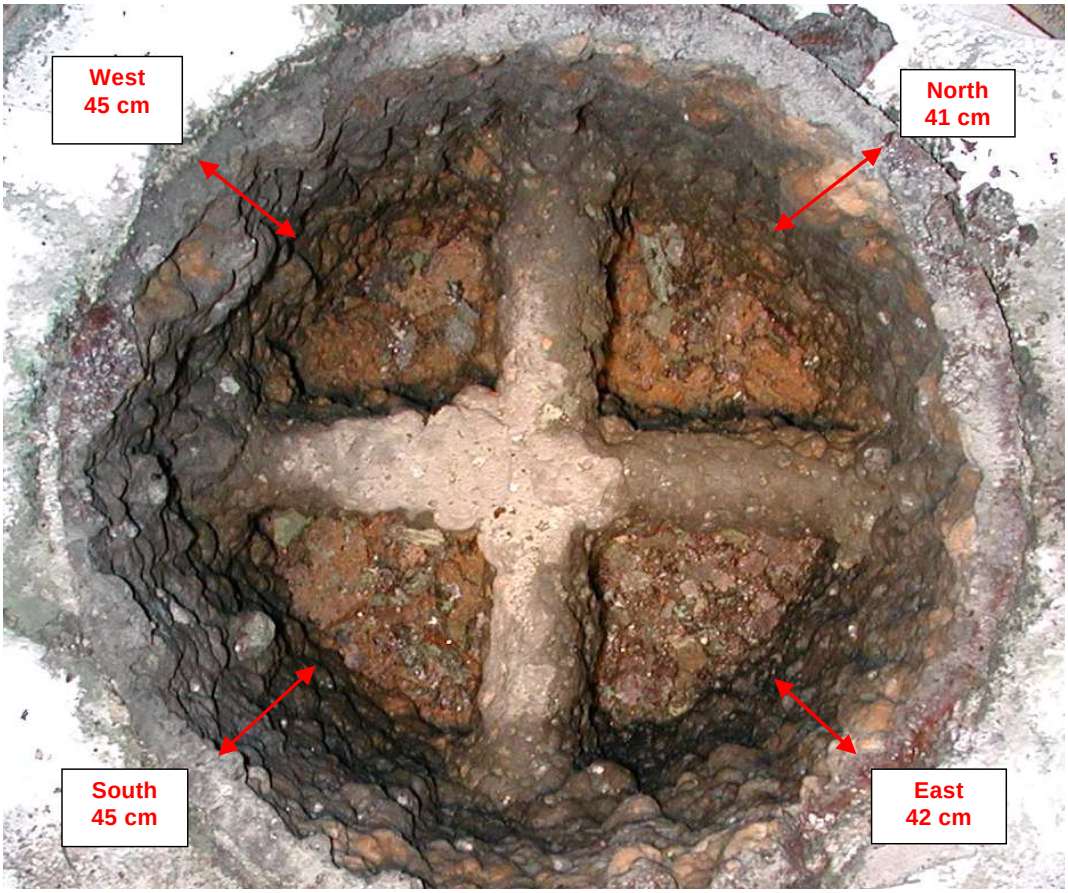

Figure 3-27. SSWICS-12 Corium Levels in Each Partition.

3.4 SSWICS-13 Test Results

3.4.1 Test Operations

The day before the test, the metering valves on the water lines were adjusted so that each tank would provide an initial flow rate of 0.005 kg/s. The adjustments were made over several fill and drain runs. The day of the test, the tanks were each filled with water to a level of ~0.3 m to provide the initial net driving heads of 0.2 bar. The source pressure for the nitrogen sparging lines was then set to 0.35 bar and the metering valves were adjusted until the flow to each meter showed 0.079 lpm.

The day of the test, the RV structures and water supply for top injection were preheated to ~ 100^{o}C to minimize heat sink effects after water injection. The thermite ignition system was then armed and the cell closed. The igniter coil was energized to initiate the thermite reaction, which was first detected by a sudden rise in the upper plenum gas temperature TG-RV; see Figure 3-28. As for SSWICS-12, all data have been plotted such that the x-axis origin corresponds with the initial rise in plenum gas temperature as measured by TG-RV. Peak melt temperatures of ~2000^{o}C were recorded in the north and south partitions at 70 and 80 seconds, respectively.

At one minute into the test sequence the valve on the steam line to the condensate tank was opened and at 1.4 minutes the signal to close the surge tank valve was sent so that steam would be routed to the condenser and condensate tank. The surge tank valve takes 10-15 s to fully close. When closure of the surge tank valve was confirmed, the isolation valves on the water and sparge lines were opened. The first rise in the HX outlet temperature was detected at 1.2 minutes while the first increase in the TDR level occurred at roughly 2.5 minutes. Gas injection began from both lines at 1.23 minutes. Reservoir level measurements fluctuated, but by roughly 5 minutes it became clear that water inventories were dropping in three of the four tanks. The reading from the RV pressure transducer (Figure 3-29) showed that after closure of the surge tank valve and onset of bottom water injection, the pressure steadily rose to a peak level of 1.15 bar at 3.2 minutes. Thereafter, the pressure declined and stayed below 1.1 bar for the balance of the test. By 92 minutes, three of the four tanks had emptied. The fourth tank, which was connected to one of the water/gas nozzles, did not inject any water.

No further action was taken until 112 minutes, when water injection from the top was initiated because the melt cooling rate seemed to be limited by the lack of water from the fourth tank. Top injection was repeated three more times before the end of the test. The thermocouples for the north melt sector (water nozzles, both tanks functioned) reached saturation temperature at ~ 108 minutes. The thermocouples in the south melt sector (water/gas nozzles, one tank functioned) reached saturation temperature at ~ 150 minutes. The test was subsequently terminated at 151.1 minutes.

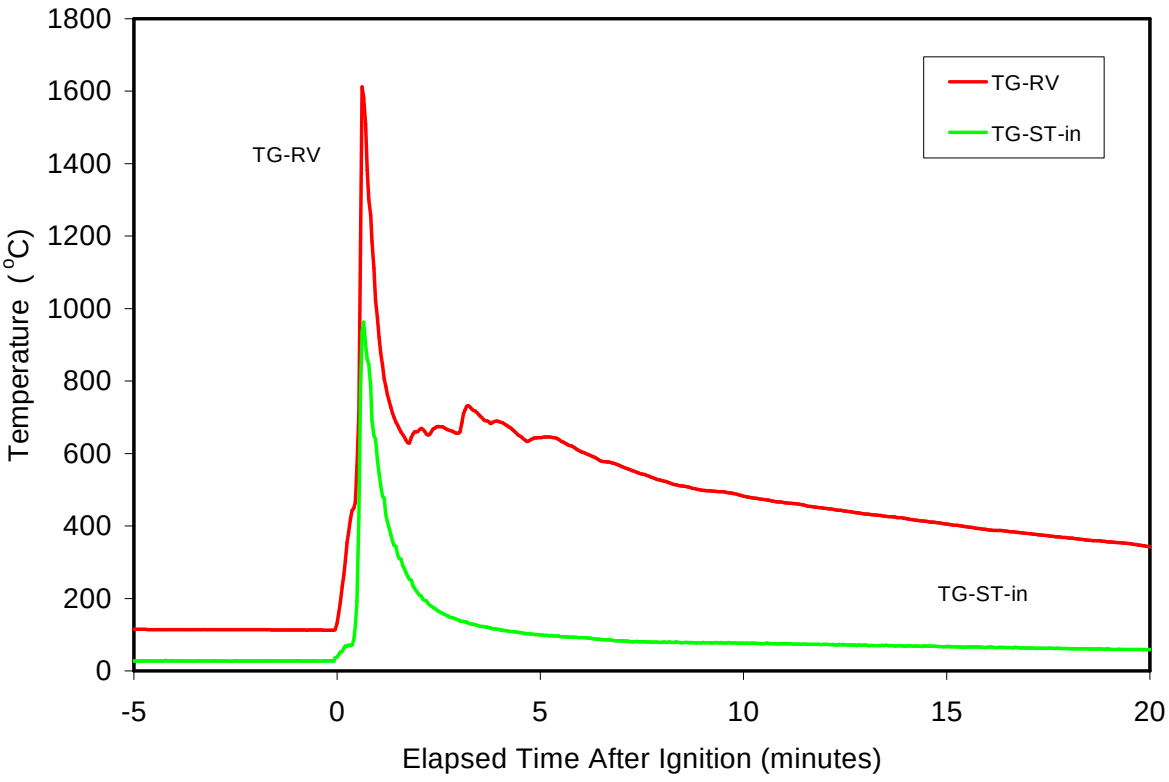

Figure 3-28. SSWICS-13 RV Plenum and Surge Tank Inlet Temperatures.

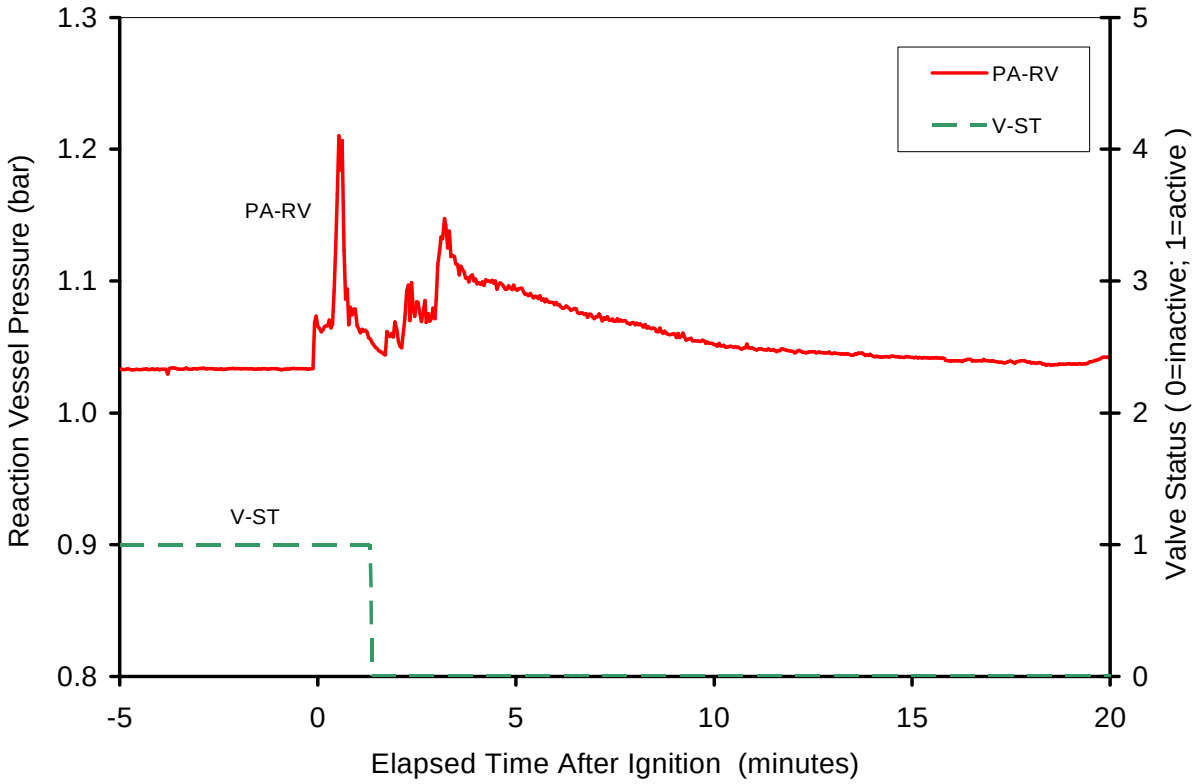

Figure 3-29. SSWICS-13 Test Section Pressure and Valve Positions.

3.4.2 Thermalhydraulic Results

Operationally, SSWICS-13 called for water injection from the top shortly after injection from the bottom was observed. This was intended to suppress the temperature of superheated steam early in the transient and avoid damage to the pressure vessel. This early injection was not performed because the upper plenum gas temperature fell quickly to < 720 ^{o}C at 1.3 minutes, and remained below this value for the balance of the test. Instead, water was added from the top only late in the transient when it appeared that the melt cooling rate might be limited by a lack of water. As the data presented later in this section shows, the cooling rate did indeed rise each time water was injected. There may have yet been water covering the bottom of the melt and the surge in heat flux could have been due to cooling of melt attached to the sides of the liners.

In terms of the bottom coolant injection system, water flow was established from only three of the four reservoirs. Level data from the reservoir tanks is provided in Figure 3-30, while the corresponding injection flowrates (calculated by differentiating the tank level data with respect to time) are shown in Figure 3-31. However, the injection rate from each of the three that functioned was ~ 4.5 g/s, close to the target rate of 5 g/s. Two of the emptied reservoirs were connected to water nozzles on the north partition, which cooled to saturation temperature first at ~108 minutes. One of the two tanks connected to the water/gas nozzles in the south partition did not drain. The south partition did not reach saturation temperature until ~ 150 minutes. As shown in Figure 3-32, both sparge lines began to inject gas at 1.2 minutes, but line 2 spiked at around 3.0 minutes and then fell to zero at ~ 4.7 minutes. Flow through line 1 was roughly 0.02 lpm for the first 83 minutes. Neither line reached the target rate of 0.06 lpm.

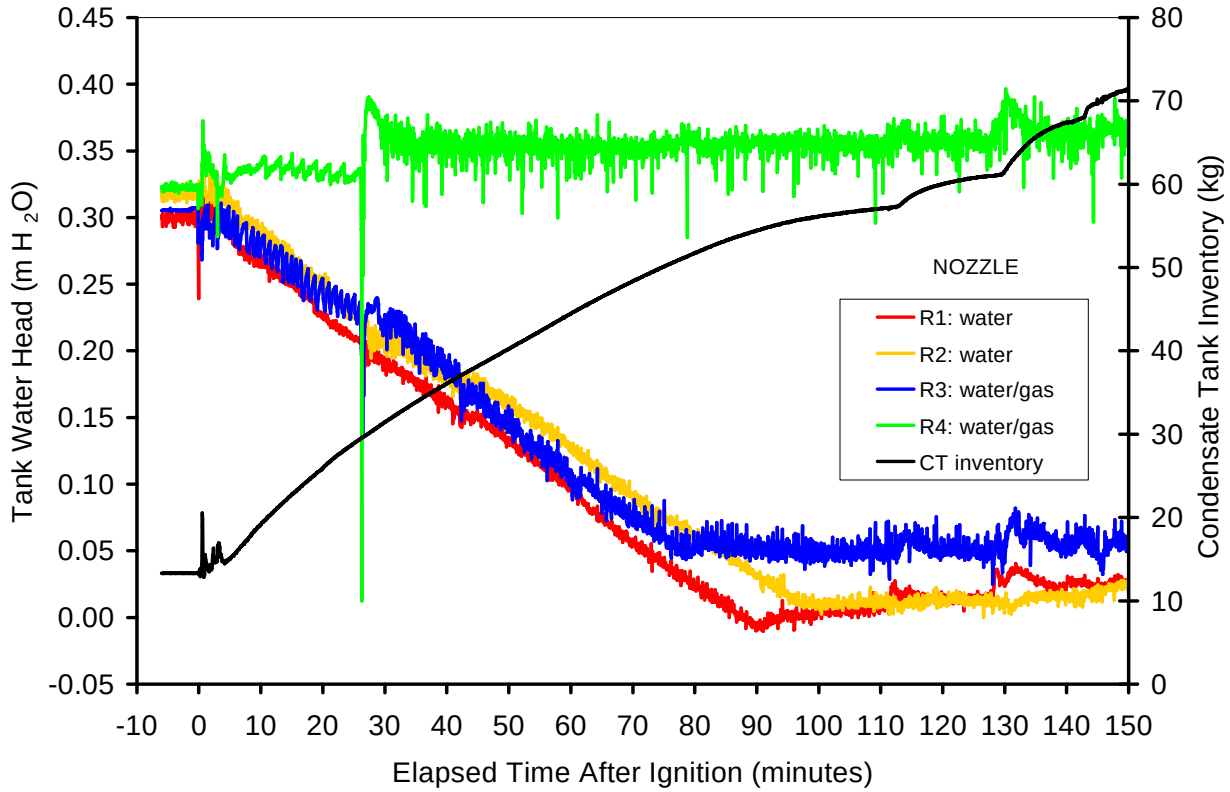

Figure 3-30. SSWICS-13 Nozzle Reservoir Tank Water Level Data.

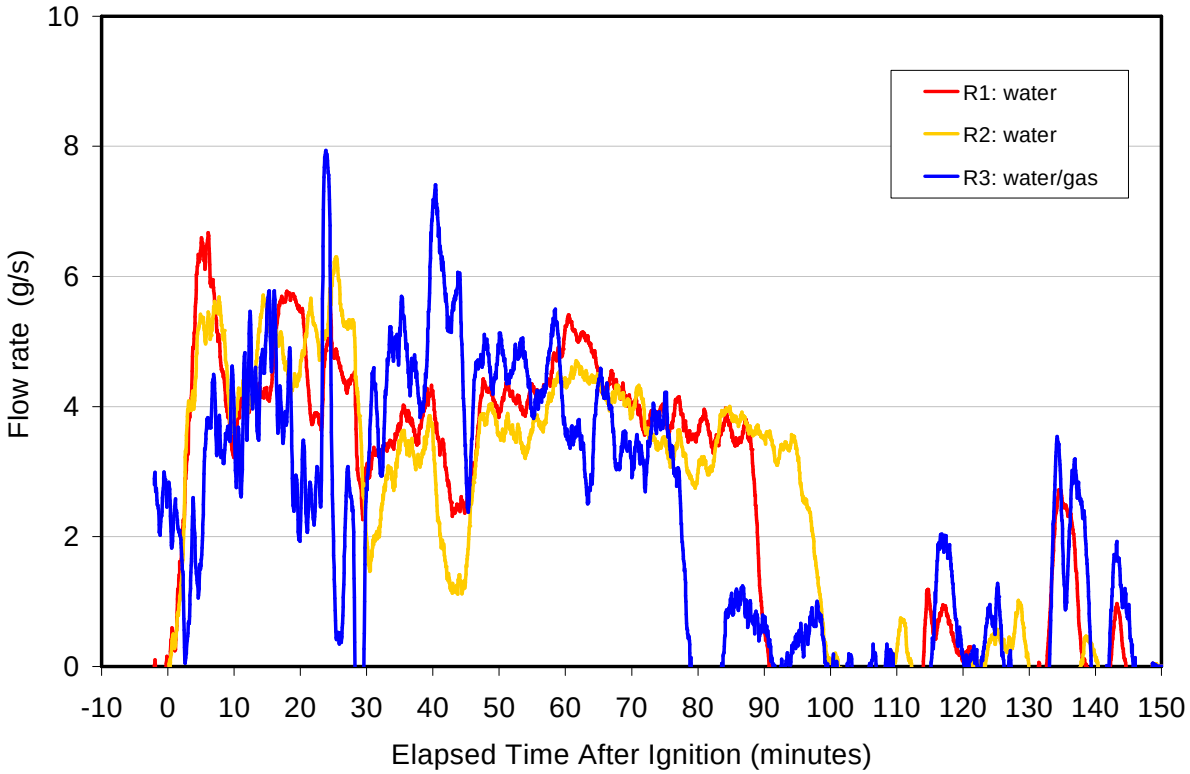

Figure 3-31. SSWICS-13 Nozzle Water Flowrates.

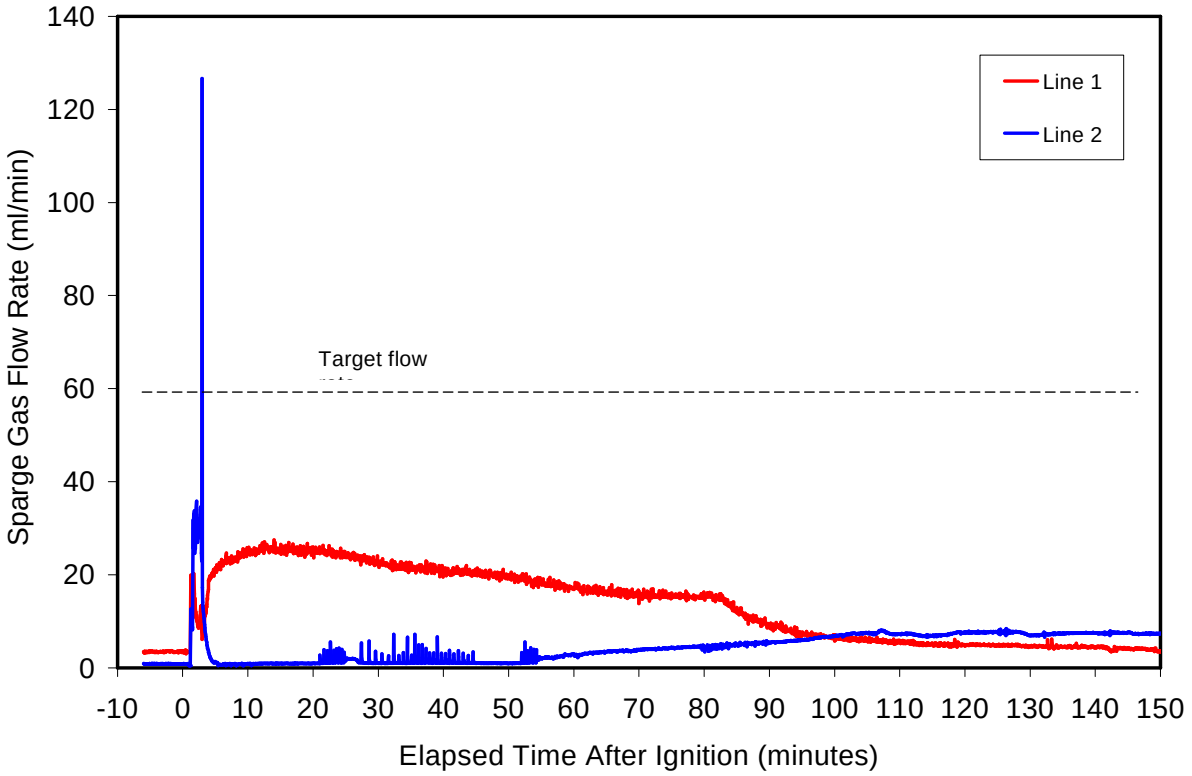

Figure 3-32. SSWICS-13 Nozzle Gas Flowrates.

Figures 3-33 and 3-34 show the melt temperatures measured in the north (water nozzle) and south (gas/water nozzle) melt sectors, respectively. The peak temperature of ~ 2000 ^{o}C was reached within 1.3 minutes. Thereafter, the temperatures in both sectors declined steadily to the coolant saturation temperature. As noted earlier, the time for complete quench in the north sector was less than that in the south (i.e., ~ 108 minutes vs. 150 minutes), but this is most likely due to the fact that coolant flow was not established to one of the nozzles in the south sector. Thus, it is not possible to determine from the melt temperature data whether gas injection had any influence on the cooling behavior. In addition, there seems to be no clear correlation between the junction elevations within the melt and the local debris cooling rate for this test.

Figure 3-35 provides the debris-water heat flux derived from measurements of condensed steam flow (DP and TDR) and from an energy balance on the heat exchanger that condenses the steam (HX).[1] The flux evaluated from the heat exchanger data (HX) provides the best estimate of the heat removal rate for this test since the superheated steam produced by the bottom quenching process passed directly into the condenser, as opposed to being cooled to saturation by an overlying water layer as occurred in SSWICS-12. This can be contrasted with the flux

[1]As for SSWICS-12, two independent measurements were used within the condensate tank: a differential pressure sensor (DP) that measures water column head and a time domain reflectometer (TDR) that measures water column height. The heat exchanger energy balance was derived from a flow measurement on the HX secondary side along with inlet and outlet thermocouples. Details of the data reduction can be found in the data report [11].

estimates based on the condensate collection rate that assume saturated steam conditions, since the steam inlet conditions to the condenser are not precisely known.

As described in Section 3.2.2, metering valves on the injection lines were adjusted to limit the peak water flow to a level 5 g/s, which yields a maximum corium quenching rate of ~ 600 kW/m^2 at saturated coolant conditions. This was half the flowrate limit set for SSWICS-12, and the reduction was motivated by a desire to further limit the melt dispersal that occurred in that test. As is evident from Figure 3-35, the heat flux during the early phase of the experiment exceeded this limit (due to superheating of the steam as it passed up through the melt). During the middle portion, the flux hovered near 250 kW/m^2 before tapering off to zero as the material cooled to saturation. Since one of the nozzles did not open in the south sector, that region was water-starved late in the test sequence because half the coolant required to quench the melt was retained in the reservoir tank. On this basis, additional water was added using the top flooding system at 111, 128, 140, and 145 minutes, and the debris in the south sector was finally quenched at 150 minutes.

On the other hand, the debris in the north sector was fully quenched by bottom injection alone at 108 minutes. The specific enthalpy change upon complete quench of the melt from 2000 ºC to saturation is estimated as 1.3 MJ/kg (same as that assumed for SSWICS-12). Given the quench time (108 minutes), initial melt mass in the north sector (78 kg), and the sector cross-sectional area (0.035 m^2), the average heat flux during the transient was thus calculated to be 450 kW/m^2. This heat flux is noted to be significant in comparison to the fluxes observed in previous SSWICS tests [3] in which the melt was only flooded from the top.

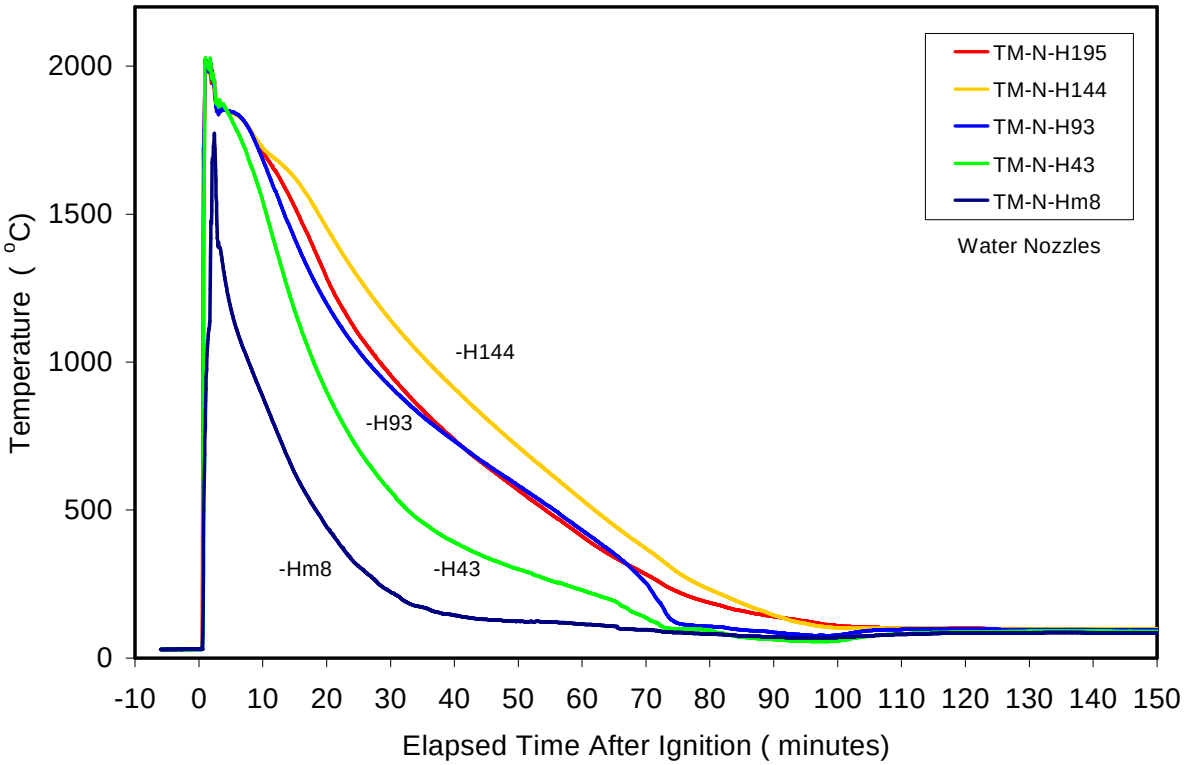

Figure 3-33. SSWICS-13 Melt Temperatures in North Quadrant (water nozzles).

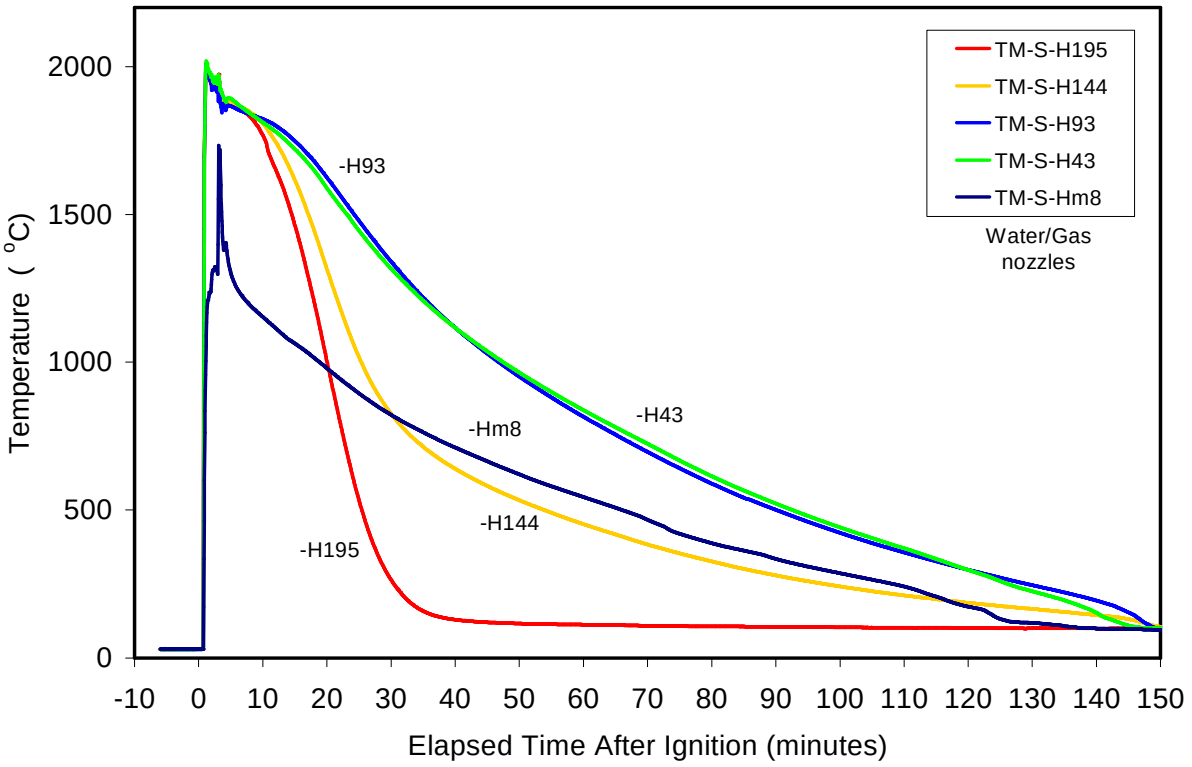

Figure 3-34. SSWICS-13 Melt Temperature in South Quadrant (water/gas nozzles)

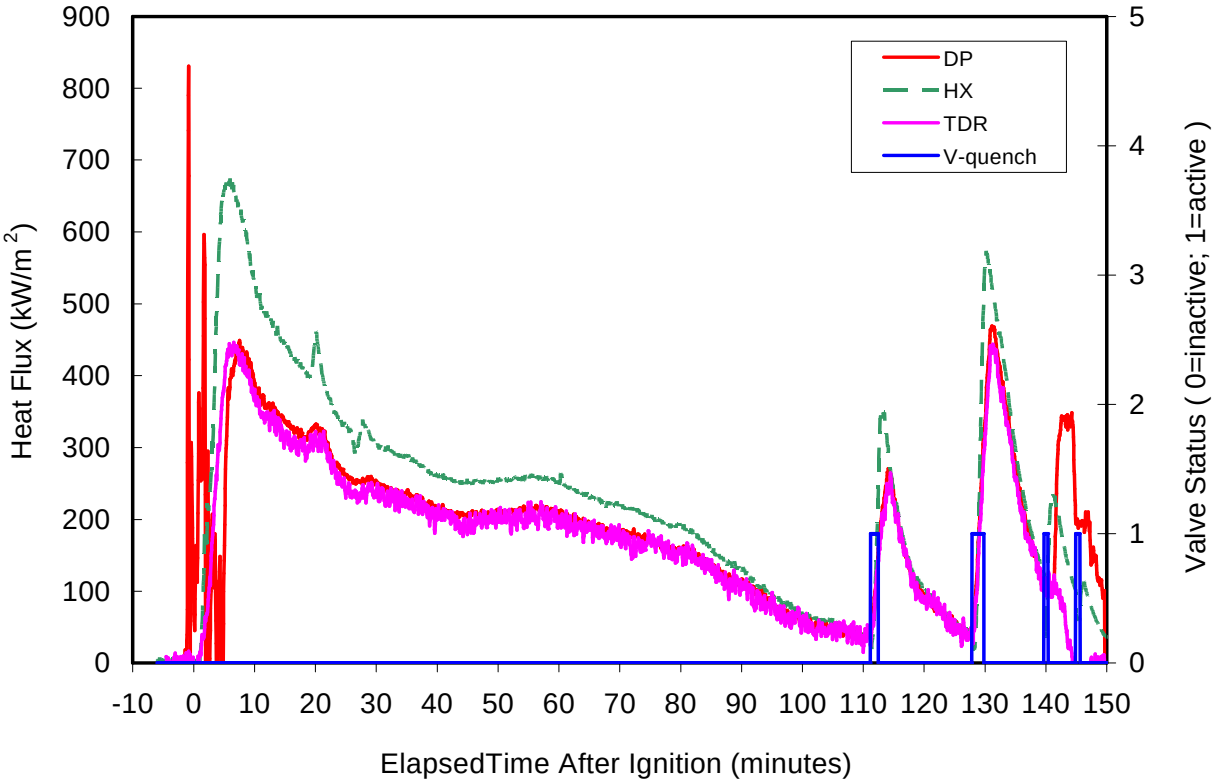

Figure 3-35. SSWICS-13 Debris-Water Heat Flux.

3.4.3 Posttest Examination

Disassembly of the pressure vessel indicated that melt was ejected upwards in a fashion similar to that of SSWICS-12. However, there was much less corium in the upper liners and none on the lid. The stainless steel liner was coated with a rather even layer of corium with a thickness of 1-2 mm. It was not possible to weigh this corium separately because it was not firmly attached to the steel and much of it fell into the lower plenum with other debris during disassembly. Figure 3-36 shows top views of the lower plenum before and after the test, while closeups of the posttest debris configuration in the north and south basemat sectors are provided in Figure 3-37.

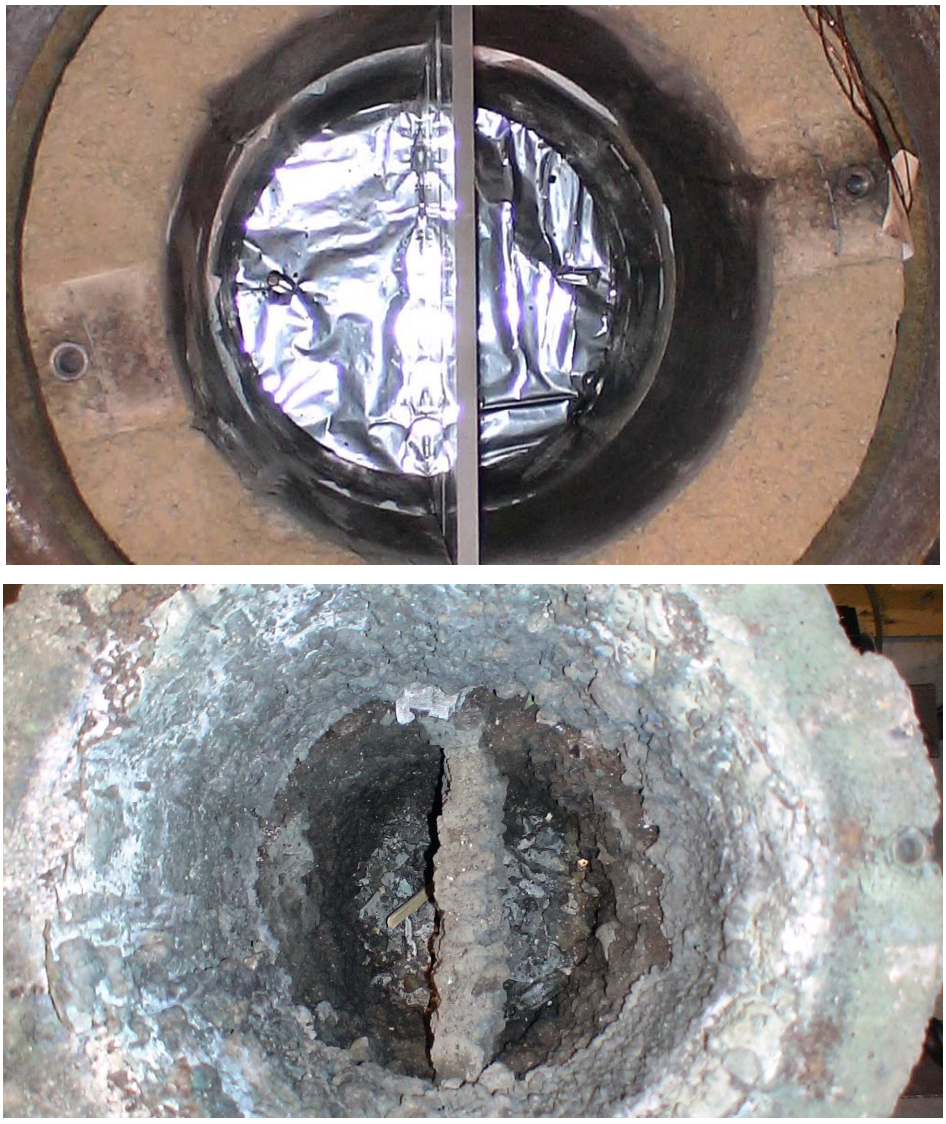

Figure 3-36. SSWICS-13 Pretest (top) and Posttest (bottom) Views of Lower Test Assembly.

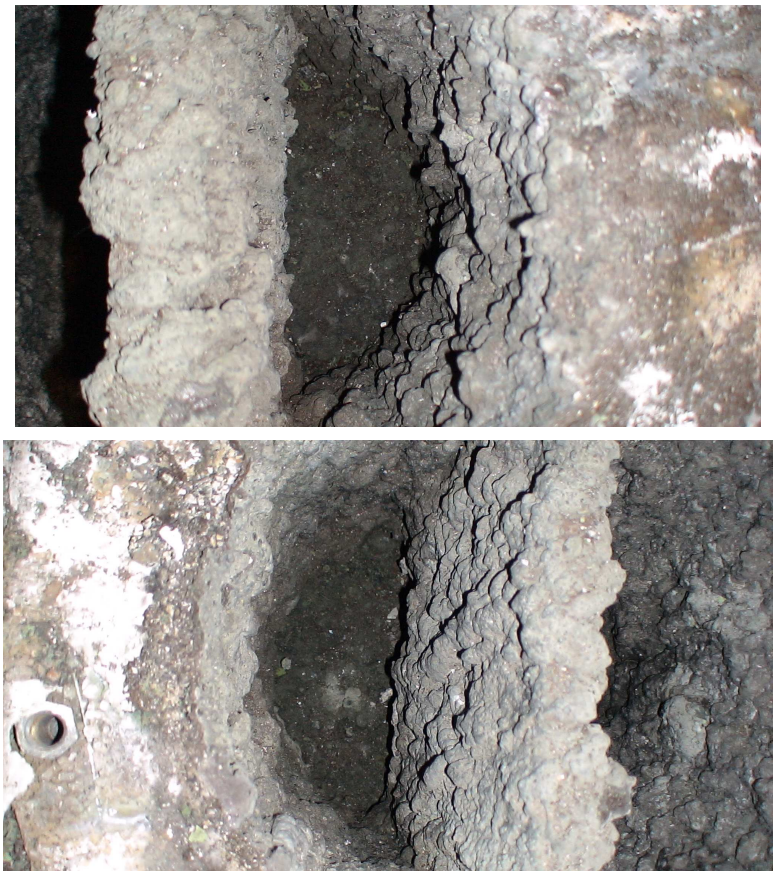

Figure 3-37. SSWICS-13 Closeups of Debris in North (top) and South (bottom) Basemat Sectors.

Figure 3-38 shows the distribution of corium collected from the vessel. As the apparatus was disassembled, corium was collected and weighed. The top zone consists of the steel liner and the second zone corresponds to the top MgO liner. The third encompasses the entire lower plenum. The amount of corium attached to the liner was based on the observed thickness range and a density of 6000 kg/m^3, estimated to be between 1.7 and 3.4 kg. Corium was firmly attached to the MgO liners and so the mass in the second zone could be determined directly by chipping corium away from the liner and weighing it separately. Corium from this second zone weighed 9.5 kg. Corium that fell from the steel liner was combined with loose debris taken out of the lower plenum. This was weighed and found to be 11.5 kg. The remaining corium was firmly affixed to the liners of the lower plenum and the tungsten plates. This material was estimated to be 113 kg based on the initial charge of 136 kg.

Finally, level measurements were made in each of the four quadrants in order to determine the final debris depths remaining over the basemat. These data are shown in Figure 3-39. The level was measured from the corium surface to the top of MgO liner, which was 62 cm above the basemat. Thus, corium depth in the north sector where water only was injected was 21 cm, while the depth in sector where a water/gas mixture was injected was 16 cm. These depths can be compared with the initial target collapsed pool depth of 30 cm. The fact that the final heights are significantly less than the target depth is consistent with the debris dispersal that occurred within the test section.

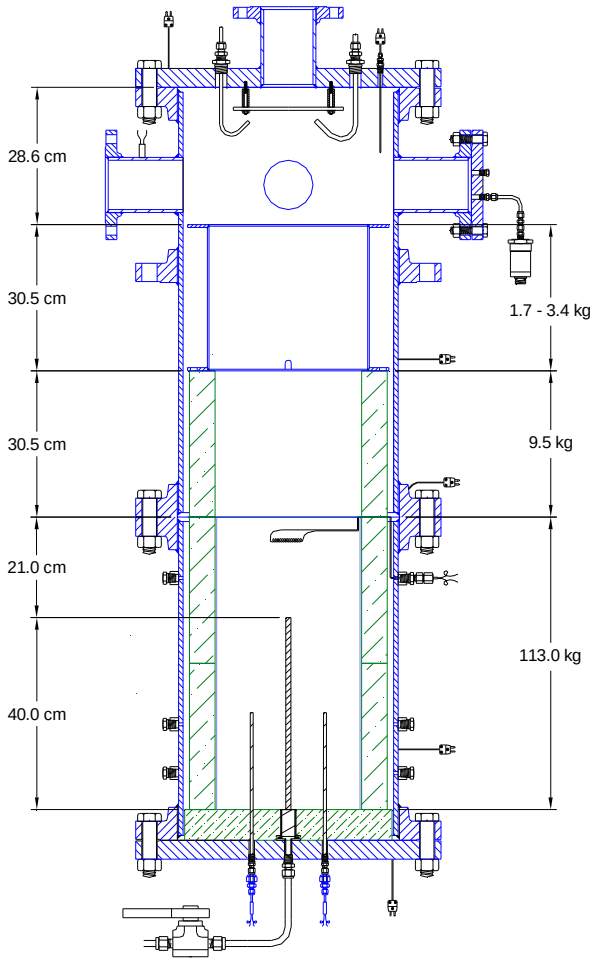

Figure 3-38. SSWICS-13 Posttest Corium Distribution.

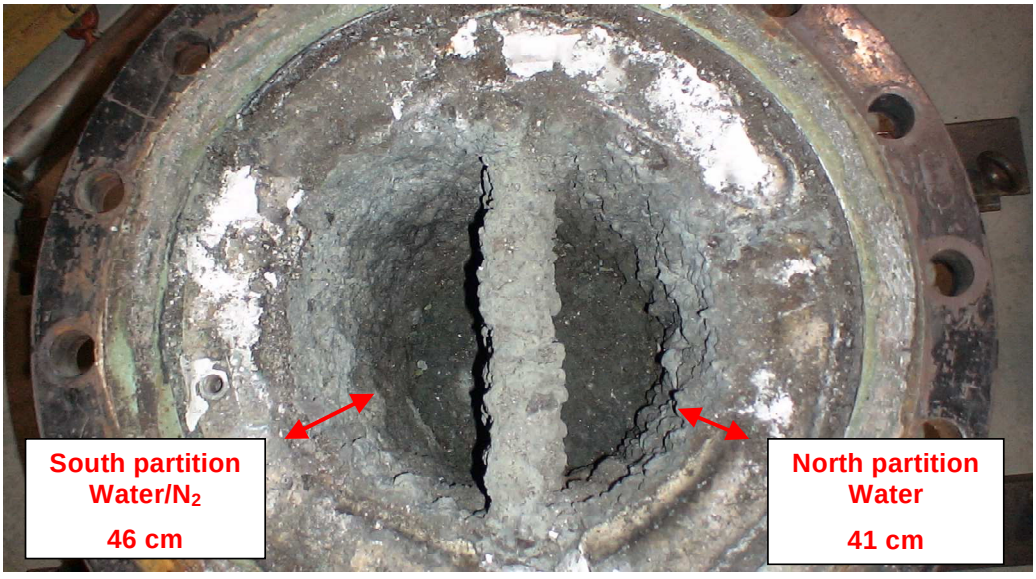

Figure 3-39. SSWICS-13 Corium Levels in Each Partition.

3.5 Discussion

Operationally, both SSWICS-12 and SSWICS-13 functioned as designed. SSWICS-12 featured an inert MgO basemat with four porous concrete injection nozzles mounted flush with the MgO surface. Water driving pressure was the key parameter investigated in this test, with heads of 0.05, 0.1, 0.15 and 0.2 bar applied to the four nozzles. Each nozzle was separated from the other by a tungsten cruciform that effectively divided the test section into four quadrants. In SSWICS-13, a specialty tube design was employed. The design was further refined by injecting water through two tubes in one sector of the melt, while a nitrogen gas-water mixture (20 % void fraction) was injected through two tubes in the other. In SSWICS-13, the additional step was taken to cover the upper surface of the injection tubes with a 10 mm thick layer of concrete to prevent direct contact with the melt following the thermite burn.

In SSWICS-12, the nozzles were throttled to provide a peak debris cooling rate of 1.2 MW/m^2 referenced to saturated coolant conditions. All four nozzles successfully opened upon contact with the melt, and debris quenching was achieved over a timescale of nominally 65 minutes. The average debris cooling rate over this time interval was 640 kW/m^2, which is ~ 50 % of the peak limit set by the nozzle orificing. There was no discernable effect of water head on the rate of cooling in the pressure range investigated as part of this study. At the throttled flowrate for this test, melt dispersal was quite large, leading to coating of the interior of the test section. As a result, water was added from the top in an effort to cool the upper internals of the RV. This somewhat complicated the data analysis, but it did not change the fact that the melt was quenched rapidly and effectively at a rate that exceeded by considerable margin the cooling rates achieved in the other SSWICS tests in which the melts were only cooled by top flooding alone [3].

For SSWICS-13, the nozzles were further throttled to provide a peak debris cooling rate of ~ 600 kW/m^2 referenced to saturation conditions. Following the thermite burn, the melt was able to ablate through the 10 mm thick concrete layer overlying the nozzles and flow was initially established in all four nozzles. However, shortly afterwards one of the nozzles that was fed by the gas/water mixture plugged so that additional water injection through this nozzle did not occur. For the three nozzles that did open, the co-injection of gas through the third nozzle was found to have no discernable influence on the average water injection flowrate when compared to the water-only nozzles over the duration of the quenching transient. Once water flow was established, the injection flowrate appeared to be relatively constant at a flowrate that was ~ 90 % of the throttled value. Based on the time to quench, it is estimated that the debris cooling rate in the sector where both water nozzles opened was on average 450 kW/m^2, which is ~ 75 % of that estimated based on the assumption of saturated coolant conditions in the melt pool. In this test, melt dispersal still occurred due to steam sparging through the melt, but not nearly to the extent as that seen in SSWICS-12. Melt quenching in SSWICS-13 also occurred at a rate that significantly exceeded that observed in the previous SSWICS top flooding experiments [3].

4.0 SUMMARY AND CONCLUSIONS

One of the key experiment objectives of the MCCI-2 program was to conduct tests to investigate new design features to enhance coolability, applicable particularly to new reactor designs. In order to meet this objective, one large scale water-cooled basemat integral effect test was conducted to provide data on the cold-crucible method for melt stabilization, and two separate effect tests were carried out to provide data on the melt fragmentation method for melt stabilization. This final report has summarized the test facilities, operating procedures, and key test results obtained from these three experiments.

The specific objective of the Water-Cooled Basemat test (WCB-1) was to provide prototypic data on the transient evolution and stabilization of a core melt in a generic water-cooled core catcher design for advanced plant applications. The experiment approach was to incorporate a water-cooled basemat into the core-concrete interaction test apparatus used for the CCI tests. The basemat was composed of five parallel water channels that were instrumented to provide both local and global data on the plate heat transfer performance. The basemat was covered with a layer of sacrificial concrete that was ablated by the overlying melt at the start of the experiment. Eventually, the melt approached, and then was thermally stabilized at, the interface of the water-cooled plate. The results from the test indicate that the up-down power split was heavily biased upwards to the overlying water pool that was added on top the melt as the ablation front approached the plate. In general, the plate was successful in cooling and stabilizing the core melt, although several hot spots developed on the plate as the experiment progressed, and the input power was reduced on that basis. However, the hot spots were noted to form on the ribbing between coolant channels, and additional analysis is needed to determine if the hot spots are problematic, or indicative of the heat removal that would be expected from a ribbed plate design. Due to the longer timeframe associated with this type of test, Direct Electrical Heating (DEH) was used to simulate decay heat within the melt to provide sufficient time for the melt to come to thermal equilibrium over the plate.

Two separate effect tests were carried out in the SSWICS test facility to provide data on the melt fragmentation cooling mechanism. The objective of the first test (denoted SSWICS-12, which was the 12^{th} test in the SSWICS series) was to evaluate the effect of pressure head on the debris cooling rate using a porous concrete nozzle design. The experiment approach was to install four nozzles into the inert MgO basemat of the SSWICS apparatus; each nozzle was fed by a different header tank, and the four tanks were positioned at different elevations in the test cell in order to vary the water head to each nozzle. The test section was divided into four quadrants using a tungsten cruciform, with one nozzle in each quadrant. This design basically allowed four tests to be conducted simultaneously. The objective of the second test (i.e., SSWICS-13) was to examine the influence of concurrent noncondensable (i.e., N_2) gas injection on the local debris cooling rate, since the presence of non-condensable gas during melt-water interaction is postulated to suppress the possibility of an energetic interaction. For this test, four stainless steel tube nozzles were incorporated into the basemat; two were fed with water only, while the other two were fed with a gas-water mixture. A tungsten cruciform was used for this test to separate the test section into two sectors; the first side contained the water-fed nozzles, while the second contained the water-gas mixture nozzles. All four nozzles were fed with the same driving pressure. This approach thus allowed two tests to be conducted simultaneously. The results of

both of these experiments confirmed that melt cooling by bottom water injection is an effective method for quenching the core melt. The results of SSWICS-12 showed that water head on the nozzles had no discernable effect on the debris quenching rate in the pressure range investigated as part of this study. All four porous concrete nozzles that were used in this test opened upon melt contact and provided a pathway for water to enter the melt. For SSWICS-13, the concurrent gas injection was found to have a negligible impact on the overall average debris quenching rate relative to that measured for pure water. In this test, three of the four nozzles opened upon melt contact, while the fourth opened briefly and then plugged for the balance of the test. The nozzle that plugged was intended to inject the water-gas mixture.

5.0 REFERENCES

1. M. T. Farmer, S. Lomperski, D. J. Kilsdonk, and R. W. Aeschlimann, "OECD MCCI Project Final Report," OECD/MCCI-2005-TR06 (2006).

2. M. T. Farmer, S. Lomperski, D. J. Kilsdonk, and R. W. Aeschlimann, "OECD MCCI Project 2-D Core Concrete Interaction (CCI) Tests: Final Report," OECD/MCCI-2005-TR05 (2006).

3. S. Lomperski, M. T. Farmer, D.J. Kilsdonk, and R. W. Aeschlimann, "Small-Scale Water Ingression and Crust Strength Tests (SSWICS) SSWICS Final Report: Thermal Hydraulic Results," OECD/MCCI-2005-TR03 (2005).

4. S. Lomperski, M. T. Farmer, D. J. Kilsdonk, and R. W. Aeschlimann, "Project Small-Scale Water Ingression and Crust Strength Tests (SSWICS) SSWICS Final Report: Crust Strength Measurements," OECD/MCCI-2005-TR02 (2005).

5. K. R. Robb and M. L. Corradini, "Ex-Vessel Corium Coolability Sensitivity Study with the CORQUENCH Code," *NURETH-13*, Kanazawa, Japan, September 27-October 2, 2009.

6. M. T. Farmer, D. J. Kilsdonk, and R. W. Aeschlimann, "Corium Coolability under Ex-Vessel Accident Conditions for LWRs," *Nucl. Eng. Technology*, **41,** 575 (2009).

7. S. Lomperski, M. T. Farmer, D. Kilsdonk, R. Aeschlimann, "Small-Scale Water Ingression and Crust Strength Tests (SSWICS) SSWICS-12 Design Report," OECD/MCCI-2008-TR06 (2009).

8. S. Lomperski, M. T. Farmer, D. Kilsdonk, R. Aeschlimann, "Small-Scale Water Ingression and Crust Strength Tests (SSWICS) SSWICS-13 Design Report," OECD/MCCI-2009-TR03 (2009).

9. M. T. Farmer, D. J. Kilsdonk, S. Lomperski, and R. W. Aeschlimann, "Category 2 Coolability Engineering Enhancement Tests: Water-Cooled Basemat Test 1 (WCB-1) Test Plan," OECD/MCCI-2008-TR04 (2008).

10. S. Lomperski, A. Ramirez, M. T. Farmer, D. Kilsdonk, R. Aeschlimann, "Small-Scale Water Ingression and Crust Strength Tests (SSWICS) SSWICS-12 Test Data Report: Thermal Hydraulic Results, OECD/MCCI-2009-TR04 (2009).

11. S. Lomperski, M. T. Farmer, D. Kilsdonk, and R. Aeschlimann, "SSWICS-13 Test Data Report: Thermal Hydraulic Results," OECD/MCCI-2009-TR07 (2009).

12. M. T. Farmer, R. W. Aeschlimann, D. J. Kilsdonk, and S. Lomperski, "Water-Cooled Basemat Test 1 (WCB-1) Data Report," OECD/MCCI-2009-TR05 (2009).

13. D. Cho et al., "Melt Quenching by Water Injection from Below: Co-Injection of Water and Noncondensable Gas," *ICONE-12*, Arlington, Virginia, April 25-29, 2004.

14. B. R. Sehgal, "Light Water Reactor (LWR) Safety," *Nucl. Eng. Technology*, **38**, 1 (2006).

15. T.G. Theofanous, C. Liu, S. Addition, S. Angelini, O. Kymäläinen, and T. Salmassi "In-Vessel Coolability and Retention of a Core Melt," *Nucl. Eng. Design*, **169,** 1 (1997).

16. T.N. Dinh, J.P. Tu, and T.G. Theofanous, "Two-Phase Natural Circulation Flow in AP-1000 In-Vessel Retention – Related ULPU-V Facility Experiments," *Proceedings ICAPP '04*, Pittsburgh, PA USA, June 13-17, 2004.

17. M. Fischer and H. Henning, "EPR™ Engineered Features for the Mitigation of Severe Accidents," *Proceedings ICAPP '09*, Tokyo, Japan, May 10-14, 2009.

18. M. Fischer, O. Herbst, and H. Schmidt, "Demonstration of Heat Removing Capabilities of the EPR Core Catcher," *Nucl. Eng. Design*, **235**, 1189 (2005).

19. V.B. Khabensky, V.S. Granovsky, S.V. Bechta, and V.V. Gusarov, "Severe Accident Management Concept of the VVER-1000 and the Justification of Corium Retention in a Crucible-Type Core Catcher," *Nucl. Eng. Technology*, **41,** 622 (2009).

20. H. Alsmeyer, M. Farmer, F. Ferderer, B. Spencer, and. W. Tromm, "The COMET-Concept for Cooling of Ex-Vessel Corium Melts," *Proceedings ICONE-6*, San Diego, CA USA, May 10-14, 1998.

21. H. Alsmeyer et al., "Ex-Vessel Core Melt Stabilization Research (ECOSTAR)," *Nucl. Eng. Design*, **235,** 271 (2005).

22. C. Journeau and H. Alsmeyer, "Validation of the COMET Bottom-Flooding Core-Catcher with Prototypic Corium," *Proceedings ICAPP '06*, Reno, Nevada USA, June 6-8, 2006.

23. M. J. Konovalikhin and B. R. Sehgal, "Investigation of Volumetrically Heated Debris Bed Quenching," *Proceedings ICONE-9*, Nice, France, April 8-12, 2001.

24. K. Nayak, B. R. Sehgal, and A. V. Stepanyan, "An Experimental Study on Quenching of a Radially-Stratified Heated Porous Bed," *Nucl. Eng. Design*, **236**, 2189 (2006).

25. M. T. Farmer, S. Lomperski, D. J. Kilsdonk, R. W. Aeschlimann, and S. Basu, "2-D Core Concrete Interaction (CCI) Tests: CCI-1 Test Data Report-Thermalhydraulic Results," OECD/MCCI-2004-TR01 (2004).

26. M. T. Farmer, S. Lomperski, D. J. Kilsdonk, R. W. Aeschlimann, and S. Basu, "2-D Core Concrete Interaction (CCI) Tests: CCI-3 Test Data Report-Thermalhydraulic Results," OECD/MCCI-2005-TR04 (2005).

27. D. H. Thompson, M. T. Farmer, J. K. Fink, D. R. Armstrong, and B. W. Spencer, “ACE Phase C Final Report: Volume I-MCCI Thermalhydraulic Results,” EPRI/ACE-TR-C42 (1997).

28. S. Lomperski, M. T. Farmer, B. Aeschlimann, D. Kilsdonk, “Final Report: Category 1 Test Results,” OECD/MCCI-2010-TR01 (2010).

29. S. Lomperski, M. T. Farmer, D. J. Kilsdonk, and R. W. Aeschlimann, “Small-Scale Water Ingression and Crust Strength Tests (SSWICS); SSWICS-6 Test Data Report: Thermalhydraulic Results,” Rev. 0, OECD/MCCI-2004-TR03, March 19, 2004.